DEPARTMENT OF PHYSICS
RWTH AACHEN UNIVERSITY

Master thesis

Two-Dimensional Quantum Simulations of a False Vacuum Decay on a Quantum Annealer

Daniil Teplitskiy

DEPARTMENT OF PHYSICS
RWTH AACHEN UNIVERSITY

Master thesis

Two-Dimensional Quantum Simulations of a False Vacuum Decay on a Quantum Annealer

Daniil Teplitskiy

Examiner:	Prof. Dr. Kristel Michielsen Prof. Dr. Markus Müller
Advisor:	Dr. Madita Willsch Dr. Dennis Willsch
Submission:	September 19, 2025

I hereby declare that I have completed this master thesis independently and without unauthorized assistance from third parties. Large language models, such as ChatGPT, have only been used occasionally as a linguistic formulation aid in this work in accordance with C) Nr. 1 of *Physics department: Recommendation on using AI tools when studying physics (14-Apr-2025)*[1]. I have not used any sources or aids other than those indicated.

Aachen, September 19, 2025

[1] `https://moodle.rwth-aachen.de/mod/resource/view.php?id=1953483`

Abstract

This work explores the qualitative dynamics of false vacuum decay in two dimensions, focusing on its realization through quantum annealing. Theoretical foundations are outlined and mapped onto quantum hardware, with several encoding strategies evaluated. Among these, the coupled domain wall encoding emerges as the most efficient, minimizing qubit usage while maintaining distance and rotational symmetries crucial for faithful modeling on a QPU. The study also addresses fidelity concerns: instead of the expected uniform distribution in the absence of an encoded potential, the coupled domain wall representation exhibited a bias toward anti-ferromagnetic states, which can be attributed to coupler imperfections. To mitigate this, techniques such as shimming and spin-reversal transformations were tested. Spin-reversal transformations proved to be most effective, both reducing variance as well as eliminating bias without requiring additional corrective iterations, thus offering a lightweight error-mitigation scheme. Building on this foundation, the decay process was simulated using modified Pöschl–Teller potentials combined with a local and global minimum. The results qualitatively reproduced the exponential decay, depending on the distance between the minima, in agreement with semiclassical quantum field theory.

Acknowledgments

I would like to thank everyone in the group who participated in valuable discussions, especially those that arose over lunch, and who provided input on this work. I am especially grateful to my supervisors, Dres. Madita and Dennis Willsch, for their constant support and guidance throughout this time, and for their readiness to help with any questions, no matter how small. Finally, I would like to thank Sophie Margarethe Küthe for carefully proofreading the thesis and for helpful comments on clarity and readability.

Contents

1. Introduction

In the beginning, there was nothing but an infinitely deep void. In a matter of moments, light emerged, and with it the universe came into existence. Over billions of years, up to the present day, it has persisted in the state we currently observe. But what if the seemingly stable state is not as stable as it intuitively appears? It is conceivable that the universe as a whole merely resides in a metastable configuration, which could, in principle, undergo a sudden transformation to a more stable true vacuum state within a fraction of a second [Col77], as proposed by Coleman in the late seventies. Although such an event is highly unlikely, it cannot be excluded within the framework of quantum field theory and is referred to as false vacuum decay.

However, this phenomenon is not restricted to the universe at large but can be observed in many areas of physics more generally. The concept appears whenever a system occupies a metastable state governed by a potential landscape. Consider, for instance, a quantum system initially trapped in such a false vacuum: over time, quantum fluctuations may induce a transition to the true vacuum, governed by the principles of quantum tunneling. Despite the underlying mechanism being well understood within the context of quantum mechanics, the actual computation of decay rates for arbitrary potentials remains a non-trivial task. In many cases — especially for multidimensional or non-analytic potentials — an exact analytical treatment is not feasible. This necessitates the use of numerical methods, which, although powerful, often reach their limits for more complex and larger system sizes due to the exponential growth of the Hilbert space — the curse of dimensionality.

This raises the question of whether one could simulate such decay processes directly on the level of quantum mechanics rather than classically, which sometimes requires approximations to manage the curse of dimensionality. With recent advances in quantum computing, this idea is becoming increasingly realistic. In contrast to classical numerical methods, a quantum simulation evolves the full quantum state of the system under the given Hamiltonian, utilizing the superposition principle over all possible states and thereby overcoming the curse of dimensionality arising from the exponential scaling of the Hilbert space with system size.

In the context of false vacuum decay, this idea has already been explored using both digital and analog quantum computing platforms. In [KL25], the decay from a metastable state was simulated on a digital quantum computer, where the system's time evolution was implemented using a trotterized approximation of the full Hamiltonian. This allowed for a stepwise, gate-based simulation of the dynamics leading to the decay, providing insights into how such tunneling phenomena can be captured within a discretized Hilbert space and controlled gate sequence. On the other hand, the use of analog quantum computers allows for the simulation of the system of interest without requiring approximations to compute decay probabilities or path integrals, as it enables modification of the actual Hamiltonian of the hardware platform — keeping in mind that this Hamiltonian is still only an approximate

description of the hardware, which becomes increasingly complex as one strives for accuracy, and may eventually fail to capture phenomena such as decoherence — and letting it evolve in time, capturing the dynamics using measurements of predefined observables. Using this approach, [VDH+25] investigated the nucleation process during false vacuum decay on an analog quantum simulator, where the continuous quantum dynamics of the system emerge naturally from the physical interactions engineered in the hardware itself. This approach, typically realized in platforms like cold atoms or trapped ions, does not rely on digital gate operations but instead allows the system to evolve according to an effective Hamiltonian that mimics the behavior of a metastable field configuration undergoing decay.

The present work builds upon the results of [AS21], where false vacuum decay was simulated within a scalar quantum field theory using a quantum annealing approach. In that study, the field was discretized and mapped onto an Ising spin system, which was then implemented on a quantum annealer to observe the tunneling dynamics from a metastable state to a lower-energy true vacuum. The tunneling probabilities extracted from the annealing process showed good qualitative agreement with theoretical predictions, providing experimental indications of instanton-like decay in a quantum field-theoretic setting. However, this demonstration was limited to one spatial dimension.

In this work, an extension of false vacuum decay simulations to two spatial dimensions is investigated, where the potential landscape and tunneling dynamics become more complex. To this end, chapter 2 introduces the theoretical foundation needed to compute the expected false vacuum decay behavior, such as the path integral formalism and the corresponding bounce solutions in two dimensions, a potential that facilitates the construction of a false vacuum scenario, as well as the theoretical background of quantum annealing with a realistic noise model, which will be used for the simulations of false vacuum decay. Chapter 3 introduces and compares several possibilities for encoding the decay onto the QPU, evaluating applicability and efficiency, with the coupled domain wall encoding emerging as the best solution. For actual simulations on the QPU, the hardware must be calibrated, as even small noise sources can significantly influence simulations of quantum systems. For this purpose, chapter 4 uses the previously introduced noise model to explore calibration methods, where spin-reversal transformation emerges as the most promising solution to mitigate errors. Before the actual simulations are run on the QPU, the numerical results for a two-dimensional potential describing a false vacuum need to be computed which is detailed in chapter 5. Chapter 6 outlines and discusses the subsequent simulation of the potential on the QPU, and the results are compared to the previously obtained numerical data. Although the two approaches exhibit consistent qualitative behavior, they differ quantitatively; the possible sources of this discrepancy are examined, and the question is raised whether these effects are of thermal or quantum nature. The thesis concludes with chapter 7, where possible applications of these simulations are presented and possible future research directions are discussed.

2. Theory

In this chapter, the theoretical foundation is introduced, which forms the basis for understanding false vacuum scenarios investigated in this thesis and enables their simulation on the D-Wave Quantum Processing Unit (QPU).

2.1. False Vacuum Decay

A false vacuum is defined as a metastable configuration of a system, a local minimum in its potential. Due to its metastability, such a configuration will eventually decay into a more stable configuration, the true vacuum, a global minimum in the potential, if given enough time. In this section, the theoretical background of the false vacuum decay is elaborated, more precisely, the qualitative behavior in dependence on a given potential. For this, the path integral formalism of QFT is introduced as a starting point and, using a semi-classical approximation, solved to retrieve a decay probability of the false vacuum. The derivations in the following sections are largely based on [DDDLR22] to which the reader is referred for further details.

2.1.1. Path integral formalism

The QFT path integral is another form of computing the amplitude for a quantum state being in some final state $|\phi_b\rangle$ while starting in some initial state $|\phi_a\rangle$, which is equivalent to the regular expression from quantum mechanics, using the time evolution operator and the inner product on the final and evolved state. For a real scalar field, the path integral is given by [PS95]

$$K(a,b) = \langle\phi_b| e^{-iHt/\hbar} |\phi_a\rangle = \int_{\phi_a}^{\phi_b} \mathcal{D}\phi e^{-i\frac{S[\phi]}{\hbar}}, \tag{2.1}$$

where H is the Hamiltonian of the present system and S the action defined by

$$S = \int_{-T/2}^{T/2} \mathcal{L} d^4x = \int_{-T/2}^{T/2} \frac{1}{2}(\partial_\mu\phi)^2 - V(\phi) dt d^3x \tag{2.2}$$

with $\mathcal{L}$ being the *Lagrangian density*, ϕ the real scalar field, $V(\phi)$ the potential depending on the field and $\partial_\mu = (\frac{\partial}{\partial_t}, \nabla)$ in the four-vector notation. The $\mathcal{D}\phi$ represents the integration of all possible paths $\phi(t)$, starting at $\phi(-T/2) = \phi_a$ and ending at $\phi(T/2) = \phi_b$. Additionally, one obtains

$$\frac{1}{2}(\partial_\mu\phi)^2 + V(\phi) = E_c \tag{2.3}$$

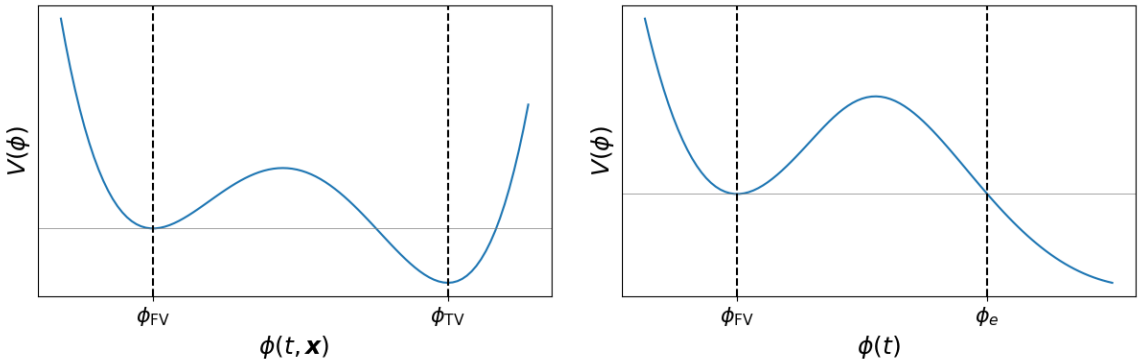

(a) QFT potential with a false vacuum ϕ_{FV} and a true vacuum ϕ_{TV}.

(b) Quantum mechanical analogue to Fig. 2.1a. ϕ_e marks the escape point governed by the classical equations of motion.

Figure 2.1.: Analogous potentials to simulate a false vacuum decay once in QFT and once in a purely quantum mechanical framework. When starting in QFT and reducing the field to one dimension such that the theory becomes isomorphic to quantum mechanics, the potential for the equivalent false vacuum decay transforms from Fig. 2.1a to Fig. 2.1b. The resulting potential becomes open for $\phi \to \infty$ with $\lim_{\phi \to \mathrm{inf}} V(\phi) < V(\phi_{\mathrm{FV}})$.

from energy conservation. In the context of a false vacuum decay and a four-dimensional quantum field theory, a potential of the form such as in Fig. 2.1a is given, where the system's field configuration over all space is at first in the false vacuum configuration ϕ_{FV} but eventually it decays into the more energy favorable true vacuum ϕ_{TV}. It is important to note that while the potential is given at a specific spatial point in time, the state of the system is defined as a collective field configuration over all space at a given time. Mathematically, the collective configuration over space is given in Eq. (2.2) by the indefinite integral over all space $\int d^3x$, while the specific time is given by the integral over time. With this, the false vacuum configuration is defined as the collective configuration that each field value over the entire space is in ϕ_{FV}, while during the decay, it evolves over time toward the collective configuration of all field values over the whole space, decaying into ϕ_{TV}.

In the semiclassical approach, in which $\hbar \to 0$, one can use the the saddle-point approximation (see A.1.2 for a more in-depth explanation). Here, because $\hbar$ goes to zero, the exponent becomes large and induces large oscillations, which will cancel out when integrating the entire configuration space. The only dominant contributions are those close to the saddle points, in complex space, of the function in the exponent. This is because a small shift in the input variables does not lead to a large change in the function's output (as the derivative of the function is close to zero at these points), which consequently suppresses large oscillations. These similar terms are then the only ones that are summed up in the integral. To make it clearer which terms these are, one needs to deform the contour in the complex plane so that the wanted saddle points become apparent in the integrand. This can be done due to

Cauchy's integral theorem, which, among other things, states that for a holomorphic function on an open region in the complex plane, the line integral is independent of the path. In the given case, these deformations need to be of global nature over the whole domain of paths to not alter the underlying physical model. Surely, one could try to search for the paths which dominate without any deformations of the domain [AGT19], but this would be an impractical task as it is not directly clear from the formulation of the integral which paths these might be. Therefore, a *Wick-Rotation* $t \to i\tau$ is performed, which represents a 90° rotation of the path domain in the complex plane and mathematically coincides with a change from the *Minkowski* into the *Euclidean* space (see. A.1.1).

This leads to the following equations where the $g_{\mu\nu}^{\text{Euclidean}}$ metric is employed

$$K(a,b) = \int_{\phi_a}^{\phi_b} \mathcal{D}\phi e^{-\frac{S[\phi]}{\hbar}} \qquad S = \int_{-T/2}^{T/2} \frac{1}{2}(\partial_\mu \phi)^2 + V(\phi) d\tau d^3x, \tag{2.4}$$

with the equation for energy conservation transforming to

$$-\frac{1}{2}(\partial_\mu \phi)^2 + V(\phi) = E_c, \tag{2.5}$$

effectively inverting the initial potential. As one can see, the oscillatory behavior arising from the i in the exponent vanishes, and as the action is invariant under a deformation of the path contour in the complex plane, the whole expression takes the form of a decay. One can solve it by finding the minima of the action, which coincide with the saddle points in complex space already mentioned above, as these are the ones that dominate the integral, and apply a second-order *functional Taylor-Expansion* (FTE) around these (see sec. A.1.3.1) to incorporate small deviations around the minima. For the sake of simplicity and foresight (as this procedure will later on only be done in the dimension for at most two concurrent active fields) only the **time dimension** is considered from here on, rendering effectively a one-dimensional quantum mechanical system, but can be adjusted to work for multiple dimensions (see sec. A.1.3.2), by accounting for all dimensions in the path. It is worth noting that while this dimension reduction seems simple on paper, it might have a great influence on the potential's form if one wants to preserve the qualitative behavior of the system, as it transforms the QFT into a purely quantum mechanical framework. Considering the potential in Fig. 2.1a, in order to preserve the qualitative decaying behavior of the system trying to flip infinitely many field values to ϕ_{TV} [Col77], one has to effectively transform it into Fig. 2.1b, as the infinity from the spatial dimensions, into which the false vacuum configuration would have decayed over an infinite time, vanished. This decay into infinity effectively becomes the open potential of Fig. 2.1b, where for $\phi \to \infty$ the potential energy is below the false vacuum energy $V(\phi) < V(\phi_{\text{FV}})$. This ensures that once the metastable state decays from ϕ_{FV}, it wanders off to infinity, never returning, similar to the QFT case. The second-order FTE of the action is then given by

$$S[\phi] \approx S[\phi_{cl}] + \frac{1}{2}\int_{-T/2}^{T/2} \delta\phi(\tau) S''[\phi_{cl}] \delta\phi(\tau) d\tau; \qquad S''[\phi_{cl}] = -\frac{\partial^2}{\partial t^2} + V''(\phi_{cl}) \tag{2.6}$$

where $\delta\phi(\tau) = \phi(\tau) - \phi_{cl}(\tau)$ and ϕ_{cl} is the classical path, also called *instanton*, representing a particle traveling in the potential, deduced from the Euler-Lagrange equations, which minimizes the action. It is convenient to define a basis set of orthonormal eigenvectors of $S''[\phi_{cl}]$ in the following manner

$$S''[\phi_{cl}]\psi_n(\tau) = \lambda_n\psi_n(\tau) \quad \text{with} \quad \int_{-T/2}^{T/2} d\tau\psi_n(\tau)\psi_m(\tau) = \delta_{nm}; \quad \psi_n(-T/2) = \psi_n(T/2) = 0. \tag{2.7}$$

This is analogous to the one-dimensional Schrödinger equation, in which one has a Hermitian differential equation with vanishing boundary conditions. The hermicity ensures orthogonal eigenvectors, which in turn yield the basis set. With this, one can write an arbitrary path in the $S''[\phi_{cl}]$ basis

$$\phi(\tau) = \phi_{cl}(\tau) + \sum_n c_n\psi_n(\tau), \tag{2.8}$$

where the start and endpoints are fixed, which, after plugging in Eq. (2.8) into (2.7), yields the following relation for the action

$$S[\phi] = S[\phi_{cl}] + \frac{1}{2}\sum_n \lambda_n c_n^2. \tag{2.9}$$

Equation (2.8) implies that an integration over all possible paths can also be equivalently written as

$$\mathcal{D}\phi = \prod_n \frac{dc_n}{\sqrt{2\pi\hbar}}, \tag{2.10}$$

where the integration is performed over all the possible c_n with an extra factor added for later convenience. Inserting this and (2.9) into Eq. (2.4) yields

$$K(a,b) = e^{-\frac{S[\phi_{cl}]}{\hbar}} \prod_n \frac{1}{\sqrt{2\pi\hbar}} \int_{-\infty}^{\infty} dc_n e^{-\frac{\lambda_n c_n^2}{2\hbar}} \tag{2.11}$$

$$= e^{-\frac{S[\phi_{cl}]}{\hbar}} \prod_n \frac{1}{\sqrt{\lambda_n}} \tag{2.12}$$

$$= \frac{e^{-\frac{S[\phi_{cl}]}{\hbar}}}{\sqrt{\det S''[\phi_{cl}]}} = Ae^{-\frac{S[\phi_{cl}]}{\hbar}}, \tag{2.13}$$

where from the first to the second line a Gaussian integral is performed, and in the last line a *functional determinant* is defined as

$$\det S''[\phi_{cl}] = \prod_n \lambda_n. \tag{2.14}$$

A similar derivation can be found in the section "Feynman Rules" of [PS95]. If there are several paths that minimize the action, one needs to sum over all of them according to

$$K(a,b) = \sum_n A_n e^{-\frac{S[\phi_{\mathrm{cl,n}}]}{\hbar}}. \tag{2.15}$$

The tunneling probability from $\phi_a \to \phi_b$ is then in turn given by $p_{\text{tunnel}} = |K(a,b)|^2$.

As in this work only the decay behavior in connection to the distance between ϕ_a and ϕ_b is investigated, which comes from the exponential factor, the specific value of the functional determinant is not needed and therefore will only appear as a proportionality factor. Nevertheless, for quantitative studies it is of interest and therefore needs to be taken into account. From this, problems may arise which need to be tackled e.g. negative eigenvalues, zero modes (zero eigenvalues) and the divergence of the determinant. They can be overcome by isolating the zero mode, the eigenstate with a zero eigenvalue, in Eq. (2.11). The zero mode is given by $\psi_0 = C\frac{\partial \phi_{\text{cl},1}}{\partial t}$, where C is a norm constant, which can be verified by computing $S''[\phi_{\text{cl},1}]\psi_0$ resulting in zero. With some calculations, which can be found in [DDDLR22], one can show that the zero mode is equivalent to an integration over all possible instanton centers (at $\phi(0)$) $\phi(\tau - \tau_1)$. This results in

$$K[\phi_{\text{cl},1}] = K[\phi_{\text{cl},0}] I T e^{-\frac{S[\phi_{\text{cl},1}] - S[\phi_{\text{cl},0}]}{\hbar}}, \tag{2.16}$$

with

$$I = \sqrt{\frac{S[\phi_{\text{cl},1}] - S[\phi_{\text{cl},0}]}{2\pi\hbar}} \sqrt{\frac{\det S''[\phi_{\text{cl},0}]}{\det' S''[\phi_{\text{cl},1}]}}, \tag{2.17}$$

where $\det' S''[\phi_{\text{cl},1}]$ is the determinant without the zero eigenvalue, $\phi_{\text{cl},1}$ is the one-way path from $a \to b$ and $\phi_{\text{cl},0}$ is the constant path that represents the particle residing at a. $K[\phi_{\text{cl},0}]$ is given by Eq. (2.13). Notably, as long as $V(\phi_a) = 0$ is chosen for the false vacuum, the action $S[\phi_{\text{cl},0}] = V(\phi_a)T$ is zero.

2.1.2. Bounce solution

In the previous section, a tunneling amplitude was computed for a path from $\phi_a \to \phi_b$. While this is sufficient to determine a transmission coefficient $\mathcal{T}$ for the tunneling probability, it does not give the decay probability per unit time that a false vacuum state might decay. In this case, considering a potential of the form of Fig. 2.1b, one resorts to the *Bounce solution* (introduced in [Col77]) according to the equations of motion, where one, instead of taking classical paths, which end behind the barrier, takes classical paths, which start and end in the false vacuum, while intermittently reaching the other side of the barrier, so-called bounces. This does not have to be limited to a single bounce but can happen arbitrarily often. All these paths which minimize the action have to be accounted for. This enables the computation of the decay probability per unit time that the state decays, meaning that the particle does not return to the false vacuum but leaks into the more favorable, lower-energy region. This can be described by

$$K(\text{FV},\text{FV}) = \langle \phi_{\text{FV}} | e^{-HT/\hbar} | \phi_{\text{FV}} \rangle = \sum_n e^{-E_n T/\hbar} \left| \langle \phi_{\text{FV}} | n \rangle \right|^2, \tag{2.18}$$

where $|n\rangle$ is the complete set of eigenstates of a Hamiltonian H, considering a potential of the form of Eq. (2.1b) with neglected tunneling, while still using the imaginary time convention. Effectively, no tunneling in this context means, that at first one approximates the potential

solely as the local minimum, i.e. the false vacuum, and ignores the lower-lying potential part behind the barrier, rendering the local minimum the absolute minimum. The last step in Eq. (2.18) is obtained by inserting the complete set of eigenstates $|n\rangle$ of the Hamiltonian H, with neglected tunneling, for the time evolution operator $e^{-HT/\hbar} = \sum_n e^{-E_n T/\hbar} |n\rangle \langle n|$. In this scenario, the eigenstate with the lowest eigenenergy which dominates Eq. (2.18) for large T, is the ground state of the local minimum, the metastable false vacuum state. Then, through an analytical transformation, the potential is transformed from only describing the false vacuum well to describing the potential with the lower energy part behind the barrier included, making the false vacuum again a local minimum, "turning" on tunneling [CC77]. In this context, Eq. (2.18) raises the question "What is the probability that the particle stays in the local minimum at position $|\phi_{\text{FV}}\rangle$ after some evolution for a given time T?". For turned-on tunneling, one can attach an imaginary part to the energy of the metastable state to account for the decay of the probability into the lower-energy region

$$\Im[E_0] = -\Gamma/2 = -\hbar\gamma/2, \tag{2.19}$$

where Γ denotes the decay width and γ the decay probability per time unit. The latter decay rate is a central quantity of interest in studies on false vacuum decay. This might seem like a non-unitary evolution as probability is leaking away, and in essence it is, as one treats the false vacuum here as an open system coupled to an environment, the lower-lying potential energy part. This results from the description of the system by a set of eigenstates for turned-off tunneling, while performing an analytical transformation of the potential exhibiting a false vacuum, while at the same time analytically continuing the spectrum of the Hamiltonian, leaving the initial set of eigenstates unmodified. As the metastable state is not in the spectrum of the Hamiltonian with full potential of Fig. 2.1b, this is therefore the only way of computing its energy [CC77]. Notably, one finds the same result for the decay probability per unit time in the imaginary part of the energy as one would have obtained in the real-time calculation. The total decay probability can, in turn, be derived from

$$\frac{dP(t)}{dt} = -\gamma P(t), \tag{2.20}$$

with $P(t) = P(0)e^{-\Gamma t/\hbar}$ being the probability for encountering the metastable ground state, consistent with Eq. (2.18).

The decay width can be isolated by taking the $T \to \infty$ limit, as the lowest eigenenergy has the largest contribution,

$$\gamma = 2\Im\left[\lim_{T\to\infty} \frac{\log K(\text{FV},\text{FV})}{T}\right]. \tag{2.21}$$

One can insert Eq. (2.15) for $K(\text{FV},\text{FV})$ while accounting for all possible multi-bounce solutions given by the exponentiation of Eq. (2.16) and neglecting tunneling in the potential

$$K(\text{FV},\text{FV}) = K[\phi_{\text{cl},0}] \sum_{n=0}^{\infty} \frac{\left(ITe^{-\frac{S[\phi_{\text{cl},b}]-S[\phi_{\text{cl},0}]}{\hbar}}\right)^n}{n!} \tag{2.22}$$

$$= K[\phi_{\text{cl},0}] \exp\left(ITe^{-\frac{S[\phi_{\text{cl},b}]-S[\phi_{\text{cl},0}]}{\hbar}}\right), \tag{2.23}$$

where $\phi_{\mathrm{cl},b}$ is the bounce solution with $\phi_{\mathrm{cl},b}(-T/2) = \phi_{\mathrm{cl},b}(T/2) = \phi_{\mathrm{FV}}$ and $\phi_{\mathrm{cl},b}(0) = \phi_e$, which is, in this case, the *escape point*, the point where the particle reaches the other side of the barrier with zero velocity and bounces back, governed by the Euler-Lagrange equations. Up to this point in the computations, $K(\mathrm{FV}, \mathrm{FV})$ is purely real as tunneling was not yet considered in the potential [DDDLR22]. Performing the analytical transformation of the potential, the prefactor I acquires an imaginary part as the lowest eigenvalue of $S''[\phi_{\mathrm{cl},b}]$ is not the zero mode anymore but a negative one, which can be seen in the zero mode acquiring a node (a zero crossing), as the velocity goes from positive to negative due to the nature of a bounce. According to the *Sturm–Liouville eigenvalue problem* [AG08] an eigenstate ψ_n has exactly n of such nodes, making the zero mode the first excited state, whereas the ground state subsequently has a negative eigenvalue. This negative value can be explained by the bounce becoming a saddle point in configuration space. The direction in configuration space in which the escape point is variable contains the maximum. After isolating this eigenvalue in Eq. (2.11) and solving the integral by analytically continuing the Gaussian integral from positive to negative λ_0, it gives rise to the imaginary part [CC77, DDDLR22]

$$\Im[I] = \frac{1}{2}\sqrt{\frac{S[\phi_{\mathrm{cl},b}] - S[\phi_{\mathrm{cl},0}]}{2\pi\hbar}}\sqrt{\frac{\det S''[\phi_{\mathrm{cl},0}]}{|\det' S''[\phi_{\mathrm{cl},b}]|}}. \tag{2.24}$$

Inserting all this into Eq. (2.21) yields

$$\gamma = \sqrt{\frac{S[\phi_{\mathrm{cl},b}] - S[\phi_{\mathrm{cl},0}]}{2\pi\hbar}}\sqrt{\frac{\det S''[\phi_{\mathrm{cl},0}]}{\det' S''[\phi_{\mathrm{cl},b}]}}e^{-\frac{S[\phi_{\mathrm{cl},b}]-S[\phi_{\mathrm{cl},0}]}{\hbar}} = Ae^{-B}. \tag{2.25}$$

When taking into account that the bounce solution is symmetric around $\tau = 0$, furthermore considering energy conservation and that the paths are derived classically from the Euler-Lagrange equations, one can rewrite the exponent B as the expression from the previous section as

$$B = \frac{2}{\hbar}(S[\phi_{cl},1] - S[\phi_{cl},0]) = \frac{2}{\hbar}\int_{\phi_{\mathrm{FV}}}^{\phi_e} d\phi\sqrt{2[V(\phi) - V(\phi_a)]}, \tag{2.26}$$

where the path transforms into $\mathrm{FV} \to e$, the escape point behind the barrier. The tunneling probability (2.16) is proportional to the decay probability per unit time of the metastable ground state

$$|K(\mathrm{FV}, e, T)|^2 = A_K e^{-2\frac{S[\phi_{\mathrm{cl},1}]-S[\phi_{\mathrm{cl},0}]}{\hbar}} \propto A_\gamma e^{-2\frac{S[\phi_{\mathrm{cl},1}]-S[\phi_{\mathrm{cl},0}]}{\hbar}} = \gamma. \tag{2.27}$$

For the purpose of this thesis, only the exponential function will be of interest, as this will be the behavior investigated in the simulations and which should be the same for the tunneling probability as well as for the decay probability per time unit. The prefactors might differ but do not have a qualitative influence on the exponentially decaying behavior.

Remark 1 *It is important to note that even though one obtains a decay rate by Eq. (2.25), the survival probability of the metastable state derived from Eq. (2.20) only approaches zero for $t \to \infty$ if the potential $V(\phi)$ is open to the right side, meaning $V(\phi > \phi_e) < V(\phi_{FV})$.*

This ensures that once the metastable state decays, the particle never returns but moves toward infinity due to its momentum [Col77]. However, when there is a double well potential where the potential is bound and approaches positive infinity for $\phi \to \pm\infty$, one would expect that once the instanton reaches the boundary, it is reflected, and when it reaches the barrier again, it regains a probability to tunnel through, which in the end leads to oscillations in the survival probability of the metastable state. One also needs to keep in mind that when doing simulations one needs to discretize the potential in space, which in turn implicitly introduces infinite boundary conditions on the edges leading to inevitable oscillations.

2.1.3. Many degrees of freedom

The goal of this section is to extend this formalism to two concurrent one-dimensional scalar fields, which still represents a one-dimensional quantum field theory but is isomorphic to a two-dimensional quantum mechanical system, given some transformation $V(\phi(t), \psi(t)) \to V(x(t), y(t))$, where x and y represent spatial components. In general, one can write

$$K(a,b) = \langle \boldsymbol{\phi}_b | \, e^{-iHt/\hbar} \, | \boldsymbol{\phi}_a \rangle = \int_{\phi_a}^{\phi_b} d\boldsymbol{\phi} e^{-i\frac{S[\boldsymbol{\phi}]}{\hbar}} \tag{2.28}$$

$$S = \int_{-T/2}^{T/2} \frac{1}{2}(\partial_\mu \boldsymbol{\phi})^2 - V(\boldsymbol{\phi}) dt d^3x, \tag{2.29}$$

for multiple scalar fields in a four-dimensional quantum field theory [PS95] where $\boldsymbol{\phi}$ stands for the vector of all given fields $\{\phi^i\}$. For a bounce solution in a potential of the form of Fig. 2.1a, the following boundary conditions emerge

$$\lim_{\tau \to \pm\infty} \phi^i(\tau, \boldsymbol{x}) = \phi^i_{\mathrm{FV}} \qquad \lim_{|\boldsymbol{x}| \to \infty} \phi^i(\tau, \boldsymbol{x}) = \phi^i_{\mathrm{FV}} \qquad \left.\frac{\partial \phi^i}{\partial \tau}\right|_{\tau=0} = 0, \tag{2.30}$$

with ϕ^i_{FV} being the i-th field component of the false vacuum position and $\boldsymbol{x}$ the spatial coordinates. The procedure to retrieve the decay of a metastable state is the same as in the section above, where it is performed only for one dimension. This is equivalent to how it would be done in regular quantum mechanics. In four dimensions and with multiple fields, the starting point is effectively identical, as can be seen in the equation above, except for the additional integrals over the spatial coordinates due to the incorporation of field theory [Col77], but with slight differences in the result due to the generalization. Nevertheless, the procedure is the same. In the beginning, one also performs a Wick rotation, followed by the steepest-descent method where a functional Taylor expansion is applied. The phases which dominate the path integral are again the classical paths which are solutions to the Euclidean equation of motion, deduced from the Euler-Lagrange equations

$$\left(\frac{\partial^2}{\partial \tau^2} + \nabla^2\right) \phi^i = \frac{\partial V}{\partial \phi^i} \tag{2.31}$$

but for several fields and four dimensions, which are coupled ordinary differential equations. This yields an analogous decay probability per unit time as Eq. (2.25) but with a different prefactor and different bounce solutions due to the higher dimensionality.

To retrieve the bounce solutions, one can use the fact that the action is in fact O(4)-invariant, where O(4) is the four-dimensional rotation group, and therefore presume that the bounce solution, which minimizes the action, also has this property. In mathematical formulation, this means that the solution ϕ^i is only a function of the variable

$$\rho = \sqrt{\tau^2 + |\boldsymbol{x}|^2}, \tag{2.32}$$

which in turn transforms Eq. (2.31) after performing a variable transformation regarding ρ to

$$\frac{\partial^2 \phi^i}{\partial \rho^2} + \frac{D-1}{\rho}\frac{\partial \phi^i}{\partial \rho} = \frac{\partial V}{\partial \phi^i}, \tag{2.33}$$

where D is the number of dimensions. And, in fact, it was shown in [BHS$^+$16] that for a multi-field system an O(N)-symmetric bounce solution minimizes the action so that the O(N)-non-symmetric solutions can be ignored and additionally it was shown in [Col77] that such an O(N)-symmetric bounce solution always exists. The boundary conditions in Eq. (2.30) thus become

$$\lim_{\rho\to\infty} \phi^i(\rho) = \phi^i_{\mathrm{FV}} \qquad \left.\frac{\partial \phi^i}{\partial \tau}\right|_{\tau=0} = 0, \tag{2.34}$$

with the additional condition that

$$\left.\frac{\partial \phi^i}{\partial \rho}\right|_{\rho=0} = 0 \tag{2.35}$$

to avoid a singularity at this point. Lastly, the Euclidean action in spherical coordinates has the form

$$S[\boldsymbol{\phi}] = \frac{\Omega_{D-1}}{\hbar}\int_0^\infty \rho^{D-1} d\rho \left[\frac{1}{2}\left(\frac{\partial \boldsymbol{\phi}}{\partial \rho}\right)^2 + V(\boldsymbol{\phi})\right]. \tag{2.36}$$

Due to the fact that $\boldsymbol{\phi}$ is only dependent on ρ alone, there are no dependencies on the integration angles giving the surface area $\Omega_{D-1} = \frac{2\pi^{D/2}}{\Gamma(D/2)}$, with Γ being the Gamma function. In the case of several fields in one dimension, the equations above, starting from (2.32), become the equations for the problem stated in section 2.1.2, with the only difference that one has multiple fields and for analogy in the decaying behavior, the potential transforms from the form of Fig. 2.1a to Fig. 2.1b. In particular Eq. (2.36) reduces to the known action from the previous sections, as one applies the appropriate spherical integration measure based on the dimensionality, which, for one dimension, would be the regular one-dimensional Euclidean integral. Basically, it reduces to a regular quantum system with many degrees of freedom. The decay rate becomes effectively the same as in Eq. (2.25), with the exponent being a line integral in several dimensions after applying energy conservation

$$B = \frac{2}{\hbar}(S[\boldsymbol{\phi}_{cl,1} - S[\boldsymbol{\phi}_{cl,0}]) = \frac{2}{\hbar}\int_{-T/2}^{T/2} dt \left[\frac{1}{2}\left(\frac{\partial \boldsymbol{\phi}}{\partial t}\right)^2 + V(\boldsymbol{\phi}) - V(\boldsymbol{\phi}_a)\right] \tag{2.37}$$

$$= \frac{2}{\hbar}\int_{-T/2}^{T/2} dt 2\left[V(\boldsymbol{\phi}) - V(\boldsymbol{\phi}_a)\right] = \frac{2}{\hbar}\int_{-T/2}^{T/2} dt \left|\frac{\partial \boldsymbol{\phi}(t)}{\partial t}\right| \sqrt{2[V(\boldsymbol{\phi}(t)) - V(\boldsymbol{\phi}_a)]}, \tag{2.38}$$

where the path is deduced from the Euclidean action of motions due to multiple fields, with $\boldsymbol{\phi}(-T/2) = \boldsymbol{\phi}_{\mathrm{FV}}$ and $\boldsymbol{\phi}(T/2) = \boldsymbol{\phi}_e$ being analogous to the false vacuum and the escape point behind the many-dimensional potential barrier. One can define $ds = dt|\partial\boldsymbol{\phi}(t)/\partial t|$ as the arc length, which naturally gives $|\partial\boldsymbol{\phi}(s)/\partial s|^2 = 1$, thus cancelling the prefactor. For a similar derivation and more information about the arc length representation, see section A.2.1.

2.2. Modified Pöschl-Teller Potential

In the above section, the results were derived for an arbitrary scalar field, but as in the course of this study, such a decay is going to be simulated on the D-Wave QPU, a specific potential needs to be chosen. For this study, the modified Pöschl-Teller potential was chosen, as the spectrum of eigenstates and eigenenergies is well known and understood for one dimension [BP18, CGKN16], but can be expanded in a similar manner into two dimensions, as will be shown later. Additionally, with this potential, one can effortlessly construct double well scenarios which exhibit a local as well as a global minimum, which enables the measurement of a false vacuum decay. A similar study was performed in [AS21], in which a one-dimensional quantum field theory with a one-dimensional modified Pöschl-Teller potential measuring the decay from one well into the other was simulated. This paper is also the baseline for this work, motivating an extension of the previous research from a one-dimensional to a two-dimensional potential, and effectively simulating a two-dimensional quantum system.

The derivation of the bound eigenstates and their eigenenergies for the one-dimensional case is given in [BP18]. Therefore, in the following sections, the results for the two-dimensional case, obtained by the same procedure, are discussed in more detail. A more detailed derivation can be found in section A.2.2.

2.2.1. Two Dimensions

In general, the appraoch underlying the derivation is that, instead of solving the time-independent Schrödinger equation for some potential to retrieve the eigenstates, one finds the potential corresponding to some given eigenstates. In the end, one finds the modified Pöschl-Teller potential for the given eigenstates. Since in this work, only the ground states are of interest, only these will be derived, while the computation of higher excited states will not be pursued here. Taking the time-independent Schrödinger equation in two dimensions

$$\left(-\frac{\hbar^2}{2m}\Delta + V(\vec{x})\right)\varphi(\vec{x}) = E\varphi(\vec{x}), \tag{2.39}$$

where $\nabla = (\partial/\partial x, \partial/\partial y)$ and $\Delta = \nabla^2$, one can rewrite it as

$$\frac{2m}{\hbar^2}\left[V(\vec{x}) - E\right] = \frac{\Delta\varphi(\vec{x})}{\varphi(\vec{x})}. \tag{2.40}$$

Choosing the ground states depending on $l \in \mathbb{R}^+\backslash\{0\}$ and some constant $c \in \mathbb{R}$

$$\varphi_l(|\vec{x}|) = \sqrt{\mathcal{N}_0}\mathrm{sech}^l(c\cdot|\vec{x}|) \qquad \mathcal{N}_0 = \frac{|c|}{\sqrt{\pi}}\frac{\Gamma(l+1/2)}{\Gamma(l)}, \tag{2.41}$$

with $\mathcal{N}_0$ being the norm constant and Γ the Gamma function, one finds

$$\frac{2m}{\hbar^2}\left[V(\vec{x}) - E\right] = c^2\left[-l + l(l+1)\tanh^2(c\cdot|\vec{x}|) - l\frac{\tanh(c\cdot|\vec{x}|)}{|\vec{x}|}\right], \tag{2.42}$$

from which one can directly deduce the potential and the eigenenergy of the according state

$$\frac{2m}{\hbar^2c^2}V(\vec{x}) = l(l+1)\tanh^2(c\cdot|\vec{x}|) - l\frac{\tanh(c\cdot|\vec{x}|)}{|\vec{x}|} \qquad \frac{2m}{\hbar^2c^2}E = l. \tag{2.43}$$

One can verify with the Sturm–Liouville theorem that Eq. (2.41) really accounts for the family of ground states, as these exhibit zero nodes. Moreover, in [BP18] it was shown for the one-dimensional case and an integer l, that l governs the number of bound states which the Hamiltonian exhibits, having l distinct bound states. Although the authors only considered $l \in \mathbb{N}$ it also holds for $l \in \mathbb{R}$, as there is no real restriction on l. The number of bound states for real l is given by the number of solutions n for the inequality $n < l$, with $n \in \mathbb{N}_0$[CGKN16] being related to the eigenenergies. Heuristically, one could assume that the same holds for the two-dimensional case, which, within the scope of this work only bears importance as the excited bound states, as well as scattering states, are possible thermal excited states during the quantum simulations on the DWave QPU. For a derivation of Eq. (2.42) see section A.2.2.

2.3. Quantum Annealing

The emerging technology of quantum computation, especially quantum annealing, is especially well suited to study the above theoretical predictions. Quantum annealing yields a compelling use case to implement a protocol to simulate the system discussed above while at the same time these protocols enable testing of current devices in development with respect to their reliability. The focus of this work is going to be on the former but, to a lesser degree, the latter also bears importance in verifying the reliability of the results.

Quantum annealing is an optimization process based on the physical core of quantum mechanics where quantum fluctuations and superposition are used to explore the search space by tunneling mechanisms between states. Unlike gate-based quantum computing, which manipulates qubits using sequences of logic operations, quantum annealing is an adiabatic approach in which the system evolves toward a low-energy solution state of a given problem in accordance with the adiabatic theorem, given that the annealing is done slowly enough. Such a process is implemented by the D-Wave QPU, in which the hardware implements the following Hamiltonian

$$H = -\frac{A(s)}{2}\underbrace{\sum_i \sigma_i^x}_{H_D} + \frac{B(s)}{2}\underbrace{\left(g(t)\sum_i h_i\sigma_i^z + \sum_{i,j} J_{i,j}\sigma_i^z\sigma_j^z\right)}_{H_P}, \tag{2.44}$$

with σ_i^x and σ_i^z being the Pauli-X and Z matrices acting on the qubit at position i. The problem is encoded in the parameters h_i, which is an external magnetic field applied to qubit

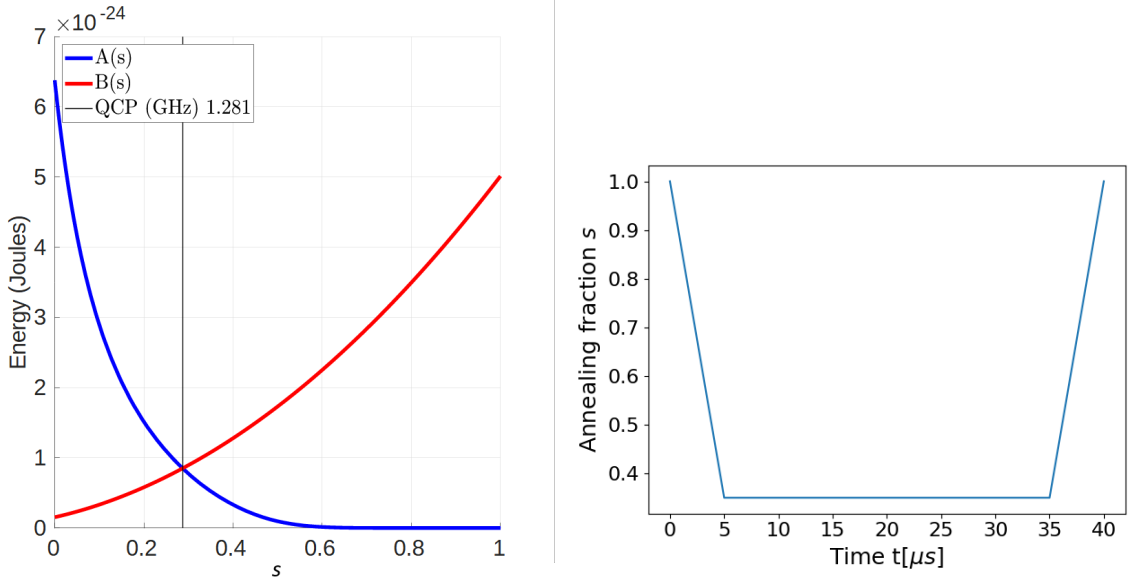

(a) Anneal schedule functions of the D-Wave Advantage System 6.4 [DWa25]

(b) Reverse anneal schedule

Figure 2.2.: Process parameters of a quantum anneal on the D-Wave QPU

i, and $J_{i,j}$, which is the coupling constant between two qubits i and j, into which the Pöschl-Teller potential from the previous section is going to be incorporated later on in chapter 3. Additionally, the Hamiltonian offers the possibility to embed a user-predefined *h-gain* function $g(t)$, which controls the h_i biases independently from the rest during the anneal. It is important to note that the annealing Hamiltonian acts on a discrete set of qubits; thus the encoded problem also has to be discretized. This does not pose a significant problem as in this work the discretization of a potential is a straightforward process, still it brings about certain implications such as the introduction of implicit infinite boundary conditions and a dependence of the final quality of the simulations on the correct choice of discretization parameters. $A(s)$ and $B(s)$ are the anneal schedule parameters depending on $s(t)$, which is specified manually by the user for the whole duration of the anneal. The anneal schedule for the *D-Wave Advantage System 6.4* can be found in Fig. 2.2a. At the end of an anneal, each qubit is measured to determine whether it is in the $|0\rangle$ or $|1\rangle$ state, which, over many qubits, returns a configuration of the whole system. This is repeated many times until one retrieves a statistically sampled probability distribution over all possible configurations. The configurations are of interest, as these contain the solution to the user-encoded problem on the QPU, which needs to be decoded afterwards with respect to the problem.

When using quantum annealing, one is usually interested in finding an optimal solution to a problem which is given by the ground state of the problem Hamiltonian, denoted by H_P, by finding a configuration which coincides with the lowest eigenenergy of this Hamiltonian. To do so, one starts at $t = 0$ and $s = 0$ in the ground state of the driving Hamiltonian

H_D, which is a superposition of all possible configurations, and lets s increase slowly to 1. Thereafter, the system should, in accordance with the adiabatic theorem, be in the ground state of the problem Hamiltonian, i.e. the configuration which optimizes the solution to the problem. Such an anneal schedule is called *forward anneal*.

The next step is to consider its application in the scope of this work, because the effect which is sought for the simulation of the false vacuum decay is not an optimization problem. Instead the focus shall be on measuring the final state of the real-time dynamics of the decay. A forward anneal is not suitable for that purpose, as it does not allow setting the initial state in the false vacuum but rather starts in a superposition of all states. If starting in the superposition of all states, one would obtain the ground state in the global minimum as the final state, but it would be impossible to deduce the decay fraction of the metastable false vacuum state from that. Instead, the D-Wave QPU allows for a *reverse anneal*, in which the initial value of $s = 1$ decreases to some arbitrary s, and, after the system has evolved for some time, increases back to $s = 1$. Such a schedule can be seen in Fig. 2.2b, which governs the parameter $s(t)$, which will also be used later for the simulation, as it allows setting the initial state in the local minimum at $s(t = 0) = 1$. As the evolution progresses, the system attains a probability to tunnel into the global minimum and at the final t_{final}, in this example $t_{\text{final}} = 40\mu s$, the system is then measured to deduce the tunneling fraction from the local to the global minimum of the run. During the whole run, the evolution of the system of the false vacuum decay only occurs while $s = 0.4$ as at that point, as $A(s)$ increases and $B(s)$ decreases, the proportionality shifts toward the drive Hamiltonian which represents the momentum of the states, introducing off-diagonal matrix terms, which can be interpreted as the momentum of a particle in an encoded Pöschl-Teller potential. With a particle momentum $p \neq 0$, the system exhibits dynamics, more specifically, in this case, the particle attains the probability to tunnel through the barrier of the double well into the global minimum. Ideally, one would start with a potential which describes only the false vacuum well at $s(0) = 1$, decrease it slowly to $s = 0.4$ and keep it constant until the end. Once $s = 0.4$ is reached, one would "turn on" the second well using the h-gain, transforming the potential to incorporate the lower-lying global minimum, analogous to the theory in subsection 2.1.2 and similar to the implementation in [AS21], in order to make the false vacuum a metastable state, introducing tunneling effects and thus causing the decaying behavior. The measurements are then taken after some time t while the s value is still 0.4. Unfortunately, the D-Wave QPU currently does not allow measurements at values $s \neq 1$, so one needs to resort to a reverse anneal scheme as described above, preferably quenching the system at the end as fast as possible within the given limits. Additionally, as will be shown later in section 3.2, it is not possible to encode a two-dimensional potential into the h-parameters.

Remark 2 *It is important to note that for long enough annealing times, thermalization likely occurs on the D-Wave QPU during the annealing process [MVHR19]. This means an exchange of thermal energy until an equilibrium is reached, as the chip on which the annealing takes place interacts with its surrounding environment through heat exchange [Ami15]. More precisely, if the system is in an excited state with an energy scale larger than the thermal energy of the environment, it can release energy to the colder environment through heat exchange, which can drive the system toward lower-energy states and potentially toward its ground state.*

This means that in the end, the state distribution does not only follow a quantum mechanical description but rather a semi-classical description in accordance with a Boltzmann distribution.

Computing the order of the effective temperature of the quantum annealing Hamiltonian by $10^{-24}/k_B \approx 72mK$ *(energy order of the Hamiltonian taken from Fig. 2.2a and* k_B *being the Boltzmann constant) and comparing it with the qubit environment temperature of* $16.0 \pm 0.1mK$*, given by D-Wave for the Advantage system 6.4, one sees that the effective temperature is larger than that of the environment within the extent of the approximation. This suggests that during thermalization, the system is likely steered toward its ground state, as higher excited states are exponentially suppressed.*

This is important to keep in mind later on, as, as mentioned in remark 1, one would expect oscillations in the survival probability of finding the particle in the local minimum due to energy conservation. With the thermalization toward the ground state taking place, one would expect that the oscillations die out after some time and the particle stays in the global minimum as this is the overall ground state. While this process of dying out takes some time due to the probabilistic nature of thermalization, it will skew the theoretical predicted decay probability per unit time. Nevertheless, it will still yield valid transmission rates to some extent compared to the case where one would have constant oscillations, for which one would need to know the oscillation frequency to measure exactly at a half-period to isolate a one-way decay from the local to the global minimum without any tunneling back occurring. For now, this is not feasible, as the theory in the sections above does not predict any oscillations and additionally such clean oscillations are not expected on the D-Wave QPU due to thermalization.

2.3.1. Noise Model

As the D-Wave QPU is an application based in reality, and not operating in an ideal setting, there will, inevitably, be some sort of interaction with the environment and therefore noise sources, which in the setting of quantum annealing might influence the couplings between the spins and their couplings to the external magnetic field. This might appear as deviations of the J and h parameters from the set value. To counter this, one needs to pre-calibrate the D-Wave QPU before running the simulation by choosing a fitting noise model to first determine the noise offset in the parameters and then correct it. Here it is presumed that the noise is systematic and that it is stable over some time.

To estimate the noise on each parameter, one can model the system for each parameter, either as a one qubit system for the h parameters or a two qubit system for the J parameters. In the two qubit system, the qubits are connected by a coupling constant $J_{i,j}$ and each qubit is subject to an external magnetic field h_i or h_j, as given by Eq. (2.44), and it is assumed that all other qubits of the machine are only acting as environment noise on the pair, as depicted in Fig. 2.3, characterized by some effective temperature T, describing a thermal equilibrium. For the one-qubit system, this model simplifies to just one qubit which is subject to an external magnetic field h_i without any couplings. If the real system exhibits direct non-zero couplings between the qubits in the modeled system and the environment, this will be noticed as a deviation of the coupling constant in the two-qubit system from the set value toward

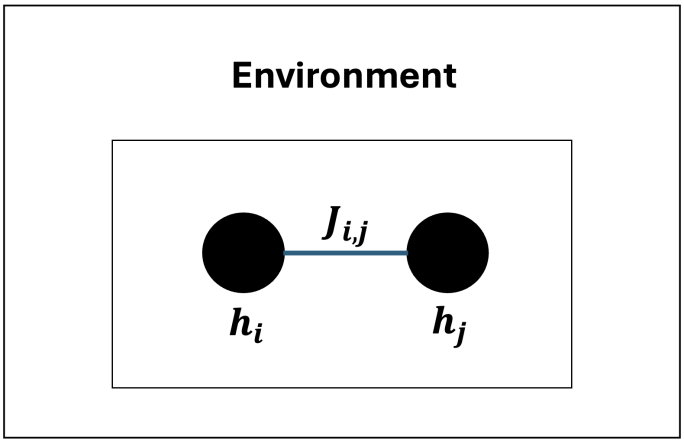

Figure 2.3.: Many-qubit system approximated as a two-spin system with an effective environment interacting with it through heat exchange. The two black dots are the spins coupled through the coupling constant J with external magnetic fields h applied to them independently.

the coupling strength to the environment. Additionally, in the one-qubit system, this will only have an effect on the magnetization if the overall magnetization of the environment is non-zero. If that is the case, the magnetization of the qubit in the modeled system will align, depending on the sign of the coupling strength, toward or away from the overall magnetization of the environment.

It is of interest to determine the couplings as well as the external magnetic field constants acting in the system, in order to be able to compare them later on to the set values, to quantize the noise, and, ideally, to eliminate systematic noise by calibration. For this, the model in Fig. 2.3 can be described by a semi-classical *Boltzmann distribution* measuring some observable $\mathcal{M}$ with the according classical *Ising-Hamiltonian* $H(s)$, which, as an input, uses a spin-configuration s of the system ($|\uparrow\downarrow\rangle$ etc., where spin-up is +1 and spin-down -1), as follows

$$\langle \mathcal{M} \rangle = \frac{1}{\mathcal{Z}} \sum_{\{s\}} \mathcal{M} e^{-\beta H(s)} \qquad \mathcal{Z} = \sum_{\{s\}} e^{-\beta H(s)} \qquad \beta = \frac{1}{k_b T}, \tag{2.45}$$

where $\mathcal{Z}$ is the norm of the probability distribution and k_b the Boltzmann constant. To determine the external magnetic field constants on each qubit one can compute the magnetization of a spin in the one-qubit system as follows

$$\langle s_i \rangle = \frac{1}{\mathcal{Z}} \sum_{\{s\}} s_i e^{-\beta h_i s_i} = \frac{e^{-\beta h_i} - e^{\beta h_i}}{e^{-\beta h_i} + e^{\beta h_i}} = -\tanh(\beta h_i), \tag{2.46}$$

with the according Hamiltonian. This can then be rearranged to retrieve the magnetic field constant. For the retrieval of the coupling constant it is assumed that the systematic noise on the h parameter can be neglected so that the true value of the h parameters can be assumed

to be on average the set value, which is supported later in section 4 by the measurement of the magnetization dependent on the set value. The same calculation is repeated for the coupling constant starting from the correlator of the spin pair

$$\langle s_i s_j \rangle = \frac{1}{\mathcal{Z}} \sum_{\{\sigma\}} s_i s_j e^{-\beta J_{i,j} s_i s_j} = -\tanh(\beta J_{i,j}), \tag{2.47}$$

where the external magnetic fields is set to zero in the Hamiltonian. And again, by transformation one can retrieve the coupling constant.

With this, it is possible to compute the J and h parameters from the magnetization and correlators and to compare them to the set values. In turn, this yields a list of offsets, which are then used to calibrate the machine by subtracting them from the set values.

Remark 3 *This is just a simplified model and does not incorporate non-linear noise, which changes depending on the range of the parameters one has set. The procedure described above attempts to group all possible noise sources on the D-Wave QPU into one, which is then characterized by some effective temperature. Thus, the choice of this temperature is crucial to determine the noise on the set values, by doing a sweep over several values of the parameters and then fit the temperature in either Eq. (2.46) or (2.47). One could potentially get an even more accurate estimation of the noise for each parameter if one weren't assuming a single overall effective temperature for the system as a whole but rather different effective temperatures, which are specific to the individual two-qubit systems, since the temperature does not have to be the same everywhere.*

3. Encodings

For the simulation of the false vacuum decay on the D-Wave quantum annealer, one needs to encode a potential, which incorporates the false vacuum, into the $J_{i,j}$ and h_i parameters of the problem Hamiltonian in Eq. (2.44). This can be done in various ways but some are more suited than others. In this chapter, the different possibilities are shown, explained and analyzed with respect to their suitability for the given problem. The encoding itself consists of encoding the modified Pöschl-Teller potential of Eq. (2.43) and therefore effectively simulating the dynamics of the Schrödinger equation with the driving Hamiltonian being the kinetic energy and the problem Hamiltonian becoming the potential landscape of the emerging particle. Effectively, the problem Hamiltonian on the quantum annealer becomes

$$H_P = H_{\text{Enc}} + H_{\text{QFT}}, \tag{3.1}$$

where H_{Enc} are the constraints that enforce an encoding, such as the domain wall encoding, which shall be introduced shortly, while H_{QFT} encodes the quantum field theoretic potential within the chosen encoding scheme. In the following sections, various methods are presented and explored, for how to do those encodings which are then probed by performing runs on the *D-Wave Quantum Annealer Advantage 6.4*. Additionally, before each run, the machine is calibrated, as will be described shortly in chapter 4, to minimize noise as much as possible.

3.1. Domain Wall Encoding

In this section, the domain wall encoding is introduced and probed for its suitability to encode a two-dimensional potential, building on its earlier successful application in [AS21] in simulating a false vacuum decay in one dimension. As it is a simple encoding, which also scales very well with system size, as will be demonstrated later, it is efficient, yet straightforward to implement. First, it was proposed in [Cha19] as a way of encoding discrete variables into Ising spin chains for quantum annealing and later on, it was used in [ACS21] as a way to encode the classical action into the quantum annealing Hamiltonian by discretizing and minimizing it, and effectively computing its bubble profile of the bounce solution.

The approach is to encode a discrete variable into an Ising spin chain that incorporates two domains of spin-up and spin-down. The change between the two domains is called the domain wall and its position governs the value of the variable. As an example, consider a discrete variable ϕ_i, with ϕ_0 and ϕ_N being some arbitrary boundary values and N the number of Ising spins. This variable can then be represented by

$$|\overbrace{\underbrace{11\cdots1}_{\times r}00\cdots0}^{N}\rangle \Leftrightarrow \phi(\tau) \equiv \phi_0 + r\xi \tag{3.2}$$

where $\phi(\tau)$ is the field as a function of time, r represents the position of the domain wall, and $\xi = (\phi_N - \phi_0)/N$ is the discretization spacing between the values. The Hamiltonian for this is given by

$$H_{\mathrm{DW}} = -\Lambda \sum_{i=1}^{N-1} \sigma_i^z \sigma_{i+1}^z - \Lambda'(\sigma_1^z - \sigma_N^z), \tag{3.3}$$

which imposes a ferromagnetic bias on neighboring spins, aligning them into the same direction, while also creating two domains by aligning the outermost spins in opposite directions as long as the condition $\Lambda < \Lambda'$ holds, i.e. as long as the energy of the configuration with one domain wall is smaller than with no domain wall. This creates a degenerate groundspace with energy $E_0 = -([N-3]\Lambda + 2\Lambda')$ that incorporates all possible domain wall positions. With N spins, only $N-1$ values can be encoded due to the boundary conditions imposed by Λ'. Given the Hamiltonian in Eq. (3.3), the J-couplings and h biases are given by

$$J_{i,j}^{\mathrm{DW}} = -\frac{\Lambda}{2}(\delta_{i+1,j} + \delta_{i,j+1}), \qquad h_i^{\mathrm{DW}} = \Lambda'(\delta_{i,1} - \delta_{i,N}), \tag{3.4}$$

assuming a symmetric Hamiltonian, as given in Eq. (2.44), due to which the factor $1/2$ appears in the J values. Reversely, the field value of a given configuration can be determined by the following equation

$$\phi(\tau) = \frac{1}{2} \sum_{i=1}^{N-1} (\phi_0 + i\xi)(\sigma_{i+1}^z - \sigma_i^z). \tag{3.5}$$

Assuming that the expectation value is taken only over domain wall states, only the term corresponding to the position of the domain wall, the transition from one domain to the other marked by a spin flip, contributes to the sum. While this term yields one, all other terms evaluate to zero. This can be used to encode an arbitrary function, in this case a potential, by inserting the discrete variable into the potential in the following manner

$$V(\phi(\tau)) = \frac{1}{2} \sum_{i=1}^{N-1} V(\phi_0 + i\xi)(\sigma_{i+1}^z - \sigma_i^z). \tag{3.6}$$

There are two possibilities to continue from here on, giving the following couplings or h biases

$$J_{i,j}^{\mathrm{QFT}} = \frac{1}{2} V(\phi_0 + i\xi)(\delta_{i,j} - \delta_{i,j-1}) \qquad h_i^{\mathrm{QFT}} = \begin{cases} -\frac{1}{2} V(\phi_0 + \xi) & \text{for } i = 1 \\ \frac{1}{2}[V(\phi_0 + (i-1)\xi) - V(\phi_0 + i\xi)] & \text{for } i < N \\ \frac{1}{2} V(\phi_0 + (N-1)\xi) & \text{for } i = N \end{cases}, \tag{3.7}$$

as one can encode the potential either directly in the h biases, by simply grouping the same spin operator in the sum above and then extracting the prefactor, or, as shown in section A.2.3, into the J-couplings. It is important to mention that due to the energy spacing between the eigenstates, given by $\Delta E = |2\Lambda|$, the maximum range between the minimum and the maximum that the potential can reach is $< \Delta E$ or else, with respect to the domain wall Hamiltonian, the excited states become more favorable in specific configurations.

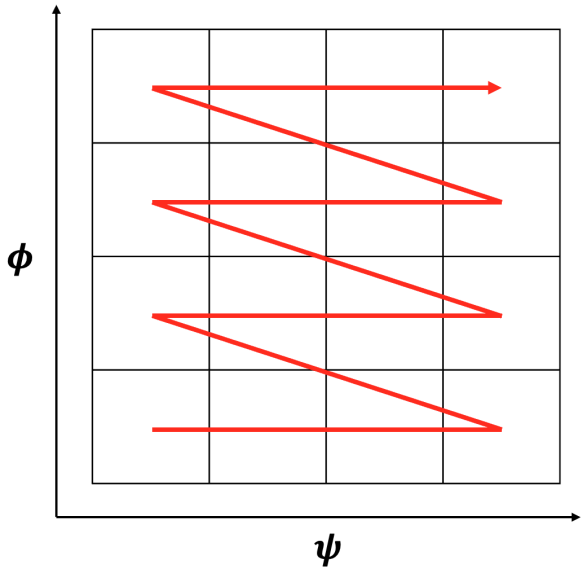

Figure 3.1.: Traverse path in a two-dimensional lattice to mimic a one-dimensional chain.

As was shown above, it is straightforward to encode a one-dimensional potential simply by plugging it into Eq. (3.7) for a spin chain. However, to encode a two-dimensional potential, one would either need to map a two-dimensional grid onto a one-dimensional chain or use two domain wall spin chains to encode the two dimensions. There are advantages and disadvantages for either of the two approaches. If everything was encoded in a single spin chain, an advantage would be that it would be possible to "turn on" the second well after some time t with the help of the *h-gain* function from the quantum annealing Hamiltonian, as was done in [AS21], giving the system time to settle in the first well and then turn on the tunneling. On the other hand, this would require the qubit numbers to grow quadratically, proportional to the system size, and would also pose problems regarding symmetry, such as breaking rotational symmetry, as will be seen, starting from the next subsection. Conversely, if one were to encode the potential in two spin-chains, one would only be able to do it using the J-parameters, as will become clear in section 3.2, so that the second well would be turned on from the beginning. However, this approach scales only linearly with the system size. In the following, some methods for obtaining these are presented and compared with respect to their applicability to the given problem by executing simulations with each of them. For the simulations, $\Lambda = 0.7$ and $\Lambda' = 0.9$ were used.

3.1.1. Zig-Zag

In this subsection, an approach is presented in which a two-dimensional potential is encoded by first discretizing it onto a grid and then traverse it in a zig-zag like manner as shown in Fig. (3.1). The two-dimensional potential can be encoded as follows: Given an $N = N_\psi \cdot N_\phi$, where N_ψ and N_ϕ are the respective numbers of qubits per axis, the path can be described

by the following curve

$$\mathcal{C}_Z : i \in \mathbb{N} \mapsto (\psi_0 + (i \ \mathbf{mod} \ N_\psi) \cdot \eta, \phi_0 + (i \ \mathbf{div} \ N_\psi) \cdot \xi) \in \mathbb{R} \times \mathbb{R}, \tag{3.8}$$

where **mod** is the modulo and **div** the integer division operation. This returns a two-dimensional vector with the respective field value for each axis, given the position i in the spin chain. The *div* and **mod** operators are used to compute the two-dimensional integer grid coordinates of the cells, which are then multiplied by the discretization spacing of the corresponding axis in order to map them onto the discretized field values. In turn, these can be inserted into the two-dimensional potential in the same manner as in Eq. (3.6) yielding a similar sum for the potential

$$V(\phi(\tau)) = \frac{1}{2} \sum_{i=1}^{N-1} V(\mathcal{C}_\mathcal{Z}(i))(\sigma_{i+1}^z - \sigma_i^z), \tag{3.9}$$

which returns two ways of encoding the potential, either in the J or h parameters

$$J_{i,j}^{\mathrm{QFT},Z} = \frac{1}{2} V(\mathcal{C}_\mathcal{Z}(i))(\delta_{i,j} - \delta_{i,j-1}) \tag{3.10}$$

$$h_i^{\mathrm{QFT},Z} = \begin{cases} -\frac{1}{2} V(\psi_0 + \eta, \phi_0) & \text{for } i = 1 \\ \frac{1}{2}[V(\mathcal{C}_\mathcal{Z}(i-1)) - V(\mathcal{C}_\mathcal{Z}(i))] & \text{for } i < N \\ \frac{1}{2} V(\psi_0 + (N_\psi - 1) \cdot \eta, \phi_0 + (N_\phi - 1) \cdot \xi) & \text{for } i = N \end{cases}, \tag{3.11}$$

where $N - 1 = N_\psi \cdot N_\phi - 1 = N_\psi \cdot (N_\phi - 1) + (N_\psi - 1)$ is used. To probe this encoding in terms of its behavior and suitability for the problem of simulating a false vacuum decay, the potential from Eq. (2.43) with $l = 1/2$ is encoded as shown in Fig. (3.2a) and a reverse anneal schedule is used as depicted in Fig. (3.2b). The system size is taken to be 32 qubits per axis, resulting in 1024 qubits used in total. The form of the potential was specifically chosen to verify whether the rotational symmetry is preserved in the ground state for a rotation-symmetric potential, as there should not be a preferred direction. No decay is expected in this case as there is no second well and the quantity of interest is solely the form of the final distribution.

The system remains in the ground state for most of the evolution until the final ramp up. According to the adiabatic theorem, a sufficiently slow ramp should enforce ground state prevalence. Both the ramp down and the ramp up were chosen to be $20\mu s$. However, this timescale is not slow enough to avoid occupation of excited states during the ramp down, while still allowing measurements to be performed on the system in a partially excited state, describing the fictive particle with some kinetic energy different from zero in the encoded potential, before thermal relaxation restores ground state dominance at $s = 1$ with zero kinetic energy. In practice, thermalization effects (as discussed in remark 2) that act while s is kept low, help to reduce these excitations and thereby increase the likelihood of finding the system in the ground state. At the minimum $s_{\min}$, the system is kept for $80\mu s$ to let it thermalize and evolve long enough to be able to observe a probability spread over the space.

Two runs are performed, for which the only difference is the minimum value $s_{\min}$ in the annealing schedule, which is done, on the one hand, to visualize the effect of different $s_{\min}$

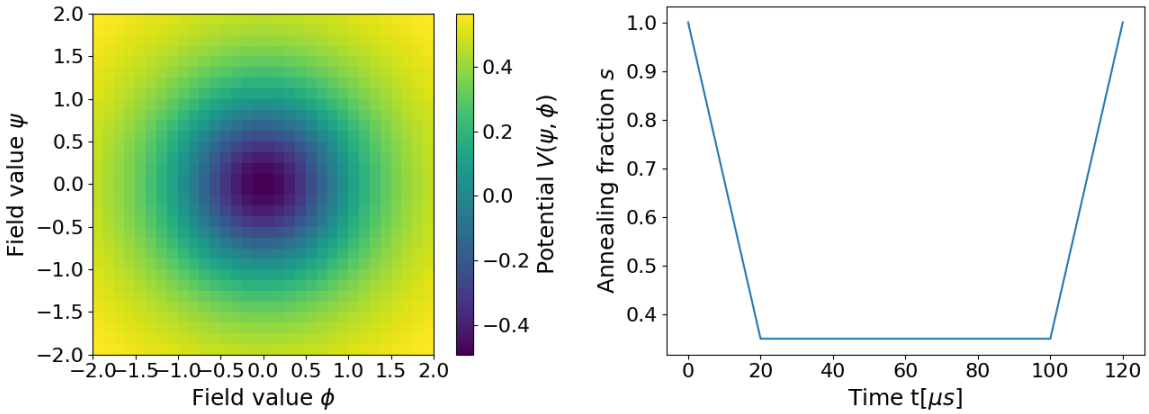

(a) Discretized potential as seen on the QPU given by (2.43) with $l = 1/2$.

(b) Schedule for the annealing fraction s, given in Eq. (2.44), in dependence of time.

Figure 3.2.: The discretized potential which was used for the simulation on the QPU, to probe the zig-zag encoding, together with the respective annealing schedule for the runs.

and, on the other hand, to accelerate the time evolution of the ground state state for lower $s_{\min}$, as the driving Hamiltonian in Eq. (2.44) becomes more prevalent and with that the "kinetic energy" of the fictive particle increases, allowing it to traverse longer distances in the same amount of time, resulting in a larger spread of the probability density. The values are $s_{\min} = 0.6$ and $s_{\min} = 0.5$. For the final probability densities, 20000 samples are taken, as can be seen in Fig. (3.3), and only domain wall states are considered, by filtering out every state that does not comply with the domain wall representation. The initial state is prepared at $(\phi, \psi) = (0, 0)$ in the domain wall representation. Since a reverse anneal schedule is being implemented, this corresponds to the ground state of the problem Hamiltonian encoding the above potential at $s = 1$, and the objective is to remain in this state until the final ramp up. One can clearly see in both figures of 3.3, that the probability spreads from its initial position but with a clear horizontal bias, violating the expected rotational symmetry. The larger spread of the probability in Fig. 3.3a than in 3.3b and the horizontal bias can be explained by closely examining the curve depicted in Fig. 3.1 that one uses to traverse the grid. It is noticeable that the probability spreads along the given curve and this can be seen in the figures 3.3. Due to the fact that the grid is encoded onto a one-dimensional spin chain, the fictive particle can only move left or right inside this chain, which is given by spin flips at the domain wall either to the left or right of it. While in the original two-dimensional system the distance between a cell and its adjacent cells (excluding diagonally neighboring ones) is the same, in the system with the zig-zag encoding the distances vary. The distance from a cell to its left or right cell, counted in spin-flips needed in the domain wall encoding, also known as *Hamming distance*, is one; but to the lower or upper cell it is N_ϕ, which explains the asymmetry with respect to the horizontal bias. Additionally, if the curve from Fig. 3.1 is superimposed onto the potential shown in Fig. 3.2a and the resulting zig-zag is then pulled

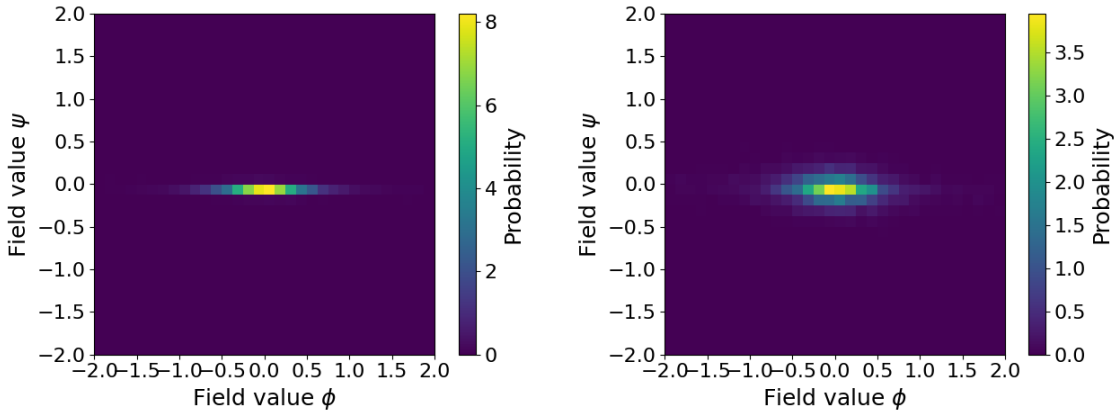

(a) $s_{\min} = 0.6$ (b) $s_{\min} = 0.5$

Figure 3.3.: Normalized result probability densities of decoded domain wall states in discretized space, obtained at the end of a simulation with the zig-zag encoding and different $s_{\min}$ values.

into the chain, along which the particle can move, the potential effectively reduces to a one-dimensional landscape with multiple wells. With lower $s_{\min}$ values one is able to explore a broader space, which in this context means to traverse a larger Hamming distance. Because lower $s_{\min}$ means lower B in Eq. (2.44), and at the same time the potential becomes flatter, the upper and lower cells also come into reach, as seen in Fig. 3.3b, but with lower probability due to the distances that need to be passed being longer. All in all, this encoding does not pose a suitable encoding in the current form due to the lack of preservation of rotational symmetry.

3.1.2. Hilbert curve

To address the rotational asymmetry from the previous section, one can turn to *space-filling curves* and try to keep the locality of the two-dimensional grid preserved in the encoding as much as possible. The *Hilbert-Curve* [Bad13] is an example of such a curve. It is computed in an iterative way and depicted in Fig. 3.4. This procedure is well described in [Bad13] and can be summarized as shown in Algorithm 1. A visualization of the algorithm is depicted in Fig. 3.4, where the initial iteration I_0, shown in the left grid, was obtained by combining four empty squares to a large one and connect their midpoints in the manner depicted. The start and endpoint are located in the lower left and right corner, respectively. With the initial iteration given, the iteration process continues in the manner described in Algorithm 1. In Fig. 3.4 three iterations are shown, where in each new iteration the previous iteration is located in the four sub-squares, indicated by the dashed lines. The previous iteration in each of the four sub-squares is then rotated and reflected in such a manner, that the starting and end points of consecutive copies connect with each other. In this example, the global starting point was chosen to be in the lower left corner and the global endpoint in the lower

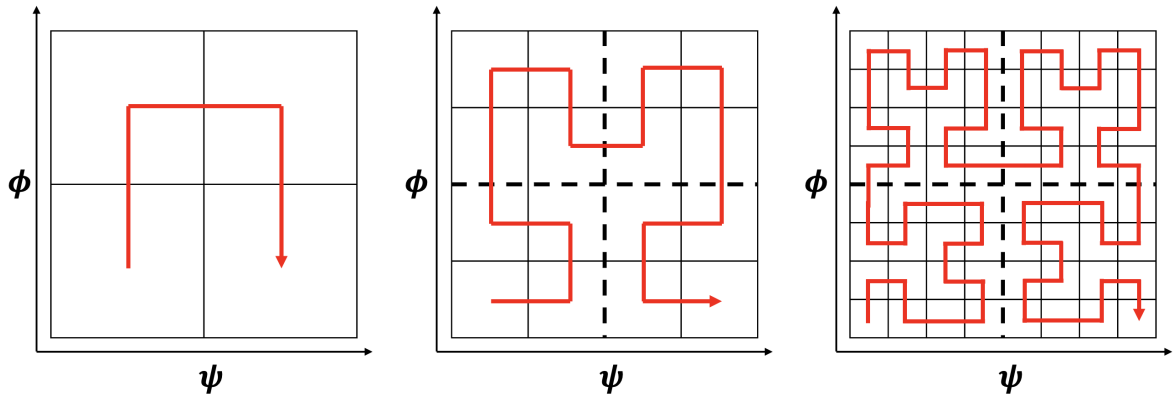

Figure 3.4.: Traverse path in a two-dimensional lattice in form of a Hilbert-curve to map to a one-dimensional chain

right corner. This ensures a distinct curve that meets the boundary conditions. This process is ended, when the desired grid size is reached. Possible grid sizes are limited to 2^{2n}, with n being the number of iterations.

For the purpose of encoding, the Hilbert curve is defined as

$$\mathcal{C}_H : i \in \mathbb{N} \mapsto (\psi_0 + x_H(i) \cdot \eta, \phi_0 + y_H(i) \cdot \xi) \in \mathbb{R} \times \mathbb{R}, \tag{3.12}$$

where i is the position in the spin chain, and the two-dimensional vector with the respective field value for each axis is returned. Using the functions $x_H(i)$ and $y_H(i)$ one can compute the two-dimensional integer grid coordinates, in accordance with the Algorithm 1. With this, similar to the previous subsection, the potential becomes

$$V(\phi(\tau)) = \frac{1}{2} \sum_{i=1}^{N-1} V(\mathcal{C}_H(i))(\sigma_{i+1}^z - \sigma_i^z), \tag{3.13}$$

after inserting the function for computing the Hilbert curve. From this, it is again possible to extract the J-couplings or h biases, depending on which should be used for encoding the

Algorithm 1 Iterative construction process of the Hilbert-curve

```
Initialize iteration I_0 as a base pattern
for each iteration n = 1, 2, ... do
    Create 4 copies of I_{n-1}
    for each copy do
        Rotate and/or reflect the copy
        Ensure orientation matches connection rules
    end for
    Connect the 4 copies end-to-end to form I_n
    Ensure that start and end points are properly aligned
end for
```

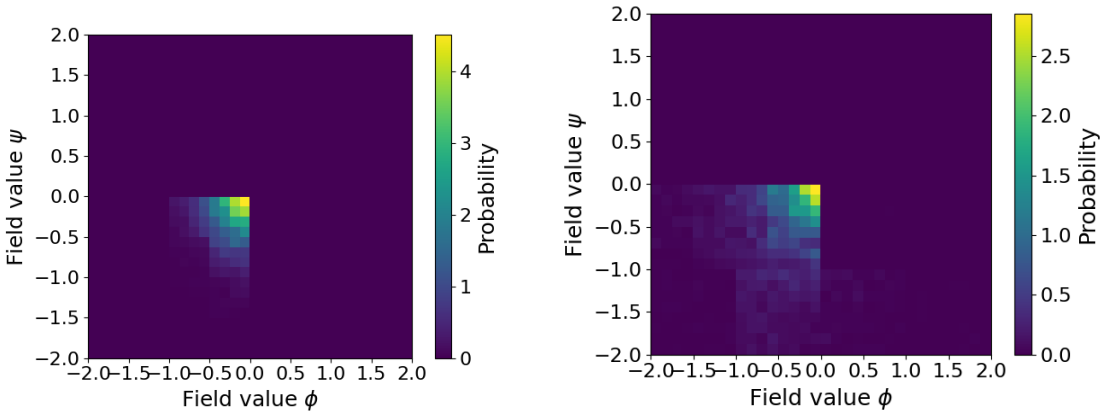

(a) $s_{\min} = 0.6$ (b) $s_{\min} = 0.5$

Figure 3.5.: Normalized result probability densities of decoded domain wall states in discretized space, obtained at the end of a simulation with the Hilbert-curve encoding and different minimal $s_{\min}$.

problem, given by

$$J_{i,j}^{\mathrm{QFT},H} = \frac{1}{2} V(\mathcal{C}_H(i))(\delta_{i,j} - \delta_{i,j-1}), \quad h_i^{\mathrm{QFT},H} = \begin{cases} -\frac{1}{2} V(\mathcal{C}_H(1)) & \text{for } i = 1 \\ \frac{1}{2}[V(\mathcal{C}_H(i-1)) - V(\mathcal{C}_H(i))] & \text{for } i < N \\ \frac{1}{2} V(\mathcal{C}_H(N-1))) & \text{for } i = N \end{cases}. \tag{3.14}$$

To probe this encoding the same simulations are executed as before in Fig. 3.2, again with 32 qubits per axis resulting in $1024 = 2^{2 \cdot 5}$ qubits in total and 5 iterations of the Hilbert curve algorithm performed. The initial state is chosen to be at $(\phi, \psi) = (0, 0)$ with the same argument as before. The resulting probability densities, taken from 20000 samples, can be seen in Fig. 3.5. It is clear that the same problems as in the zig-zag encoding persist: firstly that it is not rotation-symmetric and secondly that it has a clear bias, in this case, toward the left lower corner. This can be explained in the same manner as before for the zig-zag encoding, as only the curve one takes to traverse the grid, but not the way of encoding, differs. The problem here is also that one again uses a one-dimensional spin chain where the distances between equidistant points on a two-dimensional grid are not kept when mapped to a one-dimensional chain. The Hilbert curve keeps some locality as one can see in the figures 3.5, so that the probability density spreads in the local region (the local space is used for exploration), but it also constrains it, as is clearly visible in the figures. What one can see is that the probability stays in the subsquare where the state was initialized. In this case, it is at $(\phi, \psi) = (0, 0)$, which belongs to the lower left subsquare depicted in Fig. 3.4. When looking at the center of Fig. 3.4, at the intersection of all subsquares as indicated by the dashed lines, one can see that the cells there are right next to each other in the grid but due to the Hilbert curve they are far apart in the one-dimensional mapping, resulting yet again in large Hamming distances between the encodings of these positions. One could argue that it

might just be a question of choosing the right curve to traverse the grid, but this example is a good indication, that no matter which curve is mapped onto the grid, there will always be regions where the actual distances will not translate well enough to mapped distances during the transformation, thus resulting in non-negligible asymmetries.

3.1.3. Non-Metric Multi-Dimensional Scaling

The last method to map the two-dimensional grid onto a one-dimensional spin chain that shall be discussed in this work is to use *Non-metric Multi-Dimensional Scaling* (NMDS) [Kru64], as this does not lay a continuous curve through the multi-dimensional space, but tries to order the points in a lower dimension depending on their similarities, more precisely, their distances from each other in the higher dimension. Mathematically, if one defines the Euclidean distance $d_{i,j}(X) = |y_i - y_j|^2$ between points in some space X, then for $d_{i,j}(X) > d_{l,n}(X)$ the relation $d_{i,j}(\hat{X}) > d_{l,n}(\hat{X})$ should hold in the lower-dimensional embedding space $\hat{X}$. In this case, this results in a mapping from two dimensions to one, keeping the distance order between them as much as possible. Note that the emphasis is on order and not distance, as the former is the value of interest for the encoding. Only the distance order, not the distance itself, determines the order of the spins on the spin chain. (If one is interested in embedding the absolute distances instead of only keeping the order, one should use metric MDS.) This method is an optimization algorithm which tries to minimize the following *Stress* function

$$\mathcal{S}(x_1, x_2, \cdots, x_n; f) = \sqrt{\frac{\sum_{i \neq j} \left(f(d_{i,j}(X)) - d_{i,j}(\hat{X}) \right)^2}{\sum_{i \neq j} d_{i,j}(\hat{X})^2}}, \tag{3.15}$$

with f being a monotonically increasing function to ensure the aforementioned constraint for the rank order in the form of distance. Additionally, the stress function should be invariant to simple translations and scalings, which is ensured by the denominator in the square root. X and $\hat{X}$ are the original $\mathbb{R}^N$ and embedded $\mathbb{R}^M$ space, which, in this case, will be $N = 2$ and $M = 1$, as the mapping is performed from two dimensions to one. The optimization algorithm to find the optimal embedding is given by Algorithm 2. Executing this algorithm for 16 grid points yields a mapping to a one-dimensional chain as can be seen in Fig. 3.6. It is noticeable that while this method tries to preserve the distance order as much as possible, it still does not yield a perfect translation to one dimension simply because of the dimensionality reduction and the associated loss of information. This is also the reason why imperfect but necessary mappings happen for the sake of stress minimization, so that e.g. the points 0 and 15 are close by in the grid but far away in the one-dimensional mapping, which justifies the assumption that the same problems that already existed for the previous encodings in subsections 3.1.1 and 3.1.2 will also be prevalent here. Nevertheless, when traversing along the curve through the grid, given by the one-dimensional chain, it can then, in turn, be characterized as

$$\mathcal{C}_{\text{NMDS}} : i \in \mathbb{N} \mapsto (\psi_0 + x_{\text{NMDS}}(i) \cdot \eta, \phi_0 + y_{\text{NMDS}}(i) \cdot \xi) \in \mathbb{R} \times \mathbb{R}, \tag{3.16}$$

where the position in the chain is inserted and the corresponding coordinates in the grid are returned. The resulting h and J-parameters are then given by Eq. (3.14) only that the curve

Algorithm 2 NMDS optimization procedure with Euclidean distance $d_{i,j}(X) = |y_i - y_j|^2$, some initial space X, embedding space $\hat{X}$ and some stress function $\mathcal{S}$.

1: Initialize random points in $\hat{X}$
2: **repeat**
3: Perform isotonic regression of $d_{i,j}(\hat{X})$ on $d_{i,j}(X)$:

$$f \leftarrow \underset{f}{\operatorname{argmin}} f\ \mathcal{S}(x_1, x_2, \ldots, x_n; f)$$

4: Perform gradient descent on $\mathcal{S}$:

$$(x_1, x_2, \ldots, x_n) \leftarrow \underset{x_1, x_2, \cdots, x_n}{\operatorname{argmin}}\ \mathcal{S}(x_1, x_2, \ldots, x_n; f)$$

5: **until** stop criterion is met (e.g. $\mathcal{S}$ below threshold)
6: **return** $x_1, x_2, \ldots, x_n$

function is exchanged for $\mathcal{C}_{\text{NMDS}}$. With these parameters the simulation is carried out as in the previous sections, i.e. with 32 qubits per axis, the potential and schedule depicted in Fig. 3.2, with 20000 samples taken and the initial state positioned at $(\phi, \psi) = (0, 0)$. The resulting probability densities can be seen in Fig. 3.7. There is no clear bias to some direction, but the result appears to be more rotation-symmetric. Nevertheless, due to the dimensionality reduction of the mapping, close points in two dimensions are not necessarily close in one dimension, as mentioned above. Meanwhile, the distance order between the points seems to be preserved as much as possible, which can be deduced from the rotational symmetry of the distribution. The probability density is very concentrated. This can be explained very well by looking at the neighboring points in the one-dimensional mapping and noticing that these are likely farther apart in the two-dimensional lattice so that the difference in potential is larger than for close points, which is why the fictive particle would need more energy to enter the region of the higher potential, making it less likely. As the energy of the particle is conserved, the result is that it is less likely to encounter the particle in these areas, thus minimizing the spread of probability. One could argue that by lowering $s_{\min}$ even further the results would be better as more points would be reached, but the figures 3.7 show clearly that the fictive particle is not exploring space in a physical manner, as it already tunnels during the exploration due to the nature of NMDS. This might be a good solution for optimization problems but not for quantum simulations, where it is crucial to reproduce the dynamics of the real world to the greatest possible extent.

3.2. Coupled Domain Walls

As seen in the previous section, the encoding of a two-dimensional problem is not trivial and poses many difficulties to overcome. The mapping from a two-dimensional grid onto a one-dimensional spin chain is not satisfactory due to all the biases toward some direction because

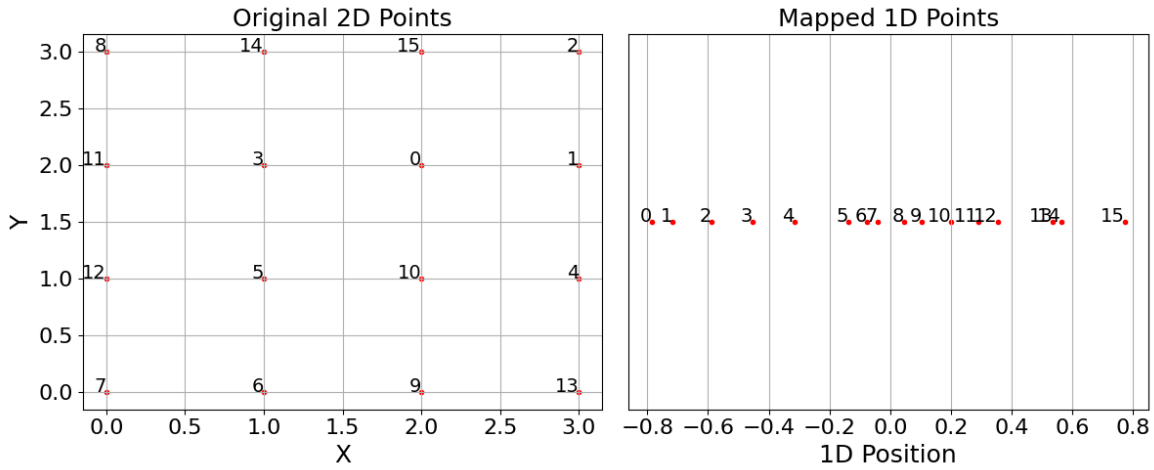

Figure 3.6.: Non-Metric Multidimensional scaling of a two-dimensional grid onto a one-dimensional chain, which, within the chain, tries to group together the spins that are neighboring in the lattice, in order to preserve as much information about the locality as possible.

of the dimensionality reduction, thus one needs to turn to other possibilities of encoding this problem. One such possibility is to use two domain walls accounting for two spin chains, where each spin chain encodes one dimension, and the field value of each domain wall is retrieved separately, using Eq. (3.5). The Hamiltonian in this case is given by [ABS22]

$$H_{\mathrm{2DW}} = -\Lambda \sum_{i=1}^{N-1} (\sigma_i^z \sigma_{i+1}^z + \sigma_{i+N}^z \sigma_{i+N+1}^z) - \Lambda'(\sigma_1^z - \sigma_N^z + \sigma_{N+1}^z - \sigma_{2N}^z), \tag{3.17}$$

with N being the number of qubits per axis of a two-dimensional grid, resulting in the same h and J-parameters for the encoding as before in Eq. (3.4) but without having a coupling between the N and $N+1$ spin. The encoding of each variable in the potential is then performed with its own respective domain wall, similar to before, which produces

$$V(\phi(\tau), \psi(\tau)) = \frac{1}{4} \sum_{i,j=1}^{N-1} V(\phi_0 + i\xi, \psi_0 + j\eta)(\sigma_{i+1}^z - \sigma_i^z)(\sigma_{N+j+1}^z - \sigma_{N+j}^z). \tag{3.18}$$

This is basically just a concatenation of two single domain walls from the previous section 3.1. As stated above, in this case, the sigmas ensure that only the terms of both domain wall positions contribute to the sum. From this, one cannot directly deduce the J or h parameters for the encoding in the Hamiltonian, so one first needs to transform the expression. This is

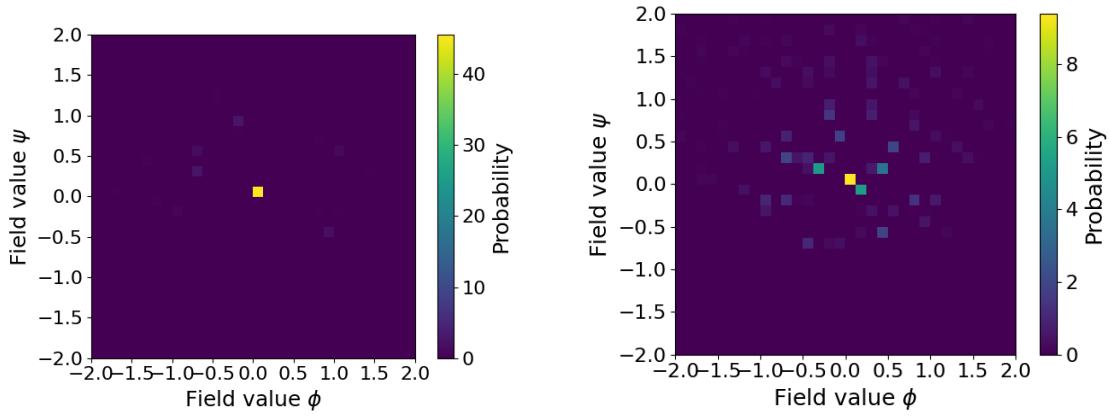

(a) $s_{\min} = 0.6$ (b) $s_{\min} = 0.5$

Figure 3.7.: Normalized result probability densities of decoded domain wall states in discretized space, obtained at the end of a simulation with the NMDS encoding and different minimal $s_{\min}$.

done in the following manner:

$$V(\phi(\tau),\psi(\tau)) = \frac{1}{4}\sum_{i=1}^{N-1}\left[(\sigma_{i+1}^z - \sigma_i^z)\sum_{j=1}^{N-1} V(\phi_0 + i\xi, \psi_0 + j\eta)(\sigma_{N+j+1}^z - \sigma_{N+j}^z)\right] \tag{3.19}$$

$$= \frac{1}{2}\sum_{i=1}^{N-1}\left[(\sigma_{i+1}^z - \sigma_i^z)\sum_{j=1}^{N} h^{\mathrm{QFT}}(i,j)\sigma_{N+j}^z\right], \tag{3.20}$$

where one first factors out one part of the sum, characterizing one of the domain walls given by the sigmas, and rearranges the sum so that Eq. (3.7) can be substituted. The resulting $h(i,j)$ function is given by

$$h^{\mathrm{QFT}}(i,j) = \begin{cases} -\frac{1}{2}V(\phi_0 + i\xi, \psi_0 + \eta) & \text{for } j = 1 \\ \frac{1}{2}[V(\phi_0 + i\xi, \psi_0 + (j-1)\eta) - V(\phi_0 + i\xi, \psi_0 + j\eta)] & \text{for } j < N \\ \frac{1}{2}V(\phi_0 + i\xi, \psi_0 + (N-1)\eta) & \text{for } j = N \end{cases}. \tag{3.21}$$

Now, one only needs to apply the same procedure to the other sum, which is done by exchanging the order of the sums, factoring the h function into the inner sum and encoding this into the h parameter, according to Eq. (3.7). This is done as follows:

$$V(\phi(\tau),\psi(\tau)) = \frac{1}{2}\sum_{j=1}^{N}\sigma_{N+j}^z\sum_{i=1}^{N-1} h(i,j)(\sigma_{i+1}^z - \sigma_i^z) = \sum_{i,j}^{N} J_{i,j}^{\mathrm{QFT,2DW}}\sigma_i^z\sigma_{N+j}^z, \tag{3.22}$$

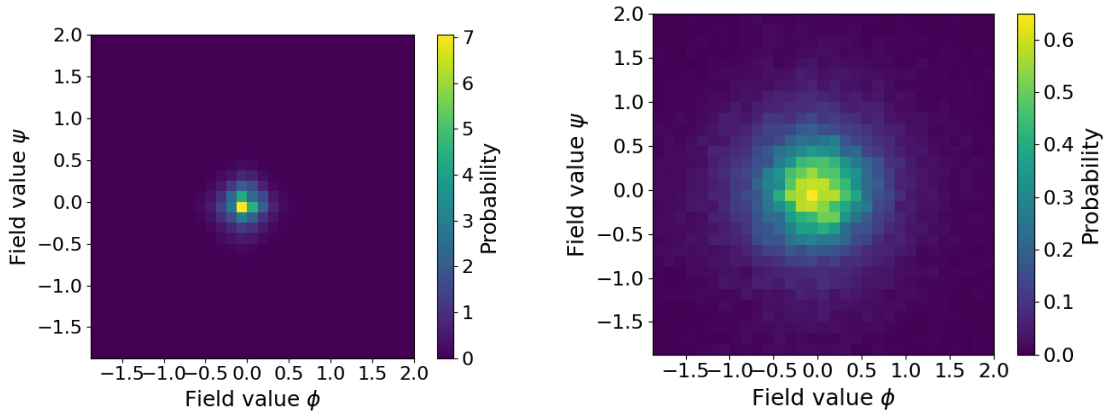

(a) $s_{\min} = 0.4$ (b) $s_{\min} = 0.35$

Figure 3.8.: Normalized result probability densities of decoded domain wall states in discretized space, obtained at the end of a simulation with the coupled domain wall encoding and different minimal $s_{\min}$.

where $J_{i,j}^{\mathrm{QFT,2DW}}$ is the encoded coupling between qubit i and j, and given by

$$J_{i,j}^{\mathrm{QFT,2DW}} = \begin{cases} -\frac{1}{2}\hat{h}(1,j) & \text{for } i = 1 \\ \frac{1}{2}[\hat{h}(i-1,j) - \hat{h}(i,j)] & \text{for } i < N \\ \frac{1}{2}\hat{h}(N-1,j) & \text{for } i = N \end{cases}. \tag{3.23}$$

As one can see, there are no h biases involved in the encoding of the potential, nor can they be somehow artificially added through transformations or the use of ancilla qubits. This presents the drawback that one has to encode the whole potential directly, without the possibility of turning on an additional potential later during the simulation, which could overlay the existing potential and effectively turn on the tunneling. The encoding is probed for 32 spins per axis and 50000 samples, by using the same procedure as in the previous section, depicted in Fig. 3.2, with the only difference that this time, the $s_{\min}$ values were chosen to be smaller. The probability densities can be seen in Fig. 3.8. The need for smaller $s_{\min}$ values can be attributed to the more complex way of encoding, which contributes to the fact that the logical graph of the problem, given by the h and J parameters, which needs to be mapped onto the physical hardware graph, is more complex, due to the all-to-all couplings between the two domain wall spin chains, and needs to use more embedding chains during the mapping. These embedding chains are also called *logical qubits* in [D-W21] and their size correlates with the *freeze-out* point, the s value after which evolution ceases and the system can be assumed to be *quasistatic* [Ami15, JAG+11]. In the logical graph, there still is approximately the same number of parameters in the leading order as there is for the one domain wall encoding from sec. 3.1, i.e. $N \times N$ couplers between the two spin chains, and $2 \times (N-1)$ couplers per spin chain for the domain wall encoding, with an extra four biases for the spins at the ends. For the one spin chain, one needs $N_{\mathrm{1D}}^2 - 1$ couplers plus

two biases, where $N_{1\mathrm{D}}$ is the number of qubits per axis in the two-dimensional grid. This can be embedded as a direct chain on the hardware without using additional qubit clusters as it is a simple geometry, but due to the all-to-all couplings in the coupled domain walls, the embedding which maps the logical graph for the coupled domain wall encoding needs to use more physical hardware qubits in combination with embedding chains. As the freeze-out point $s_{freeze-out}$ is decreasing for larger logical-qubit cluster sizes [D-W21], one needs to lower the $s_{\min}$ value to be able to see the same dynamics as before. Apart from that, Fig. 3.8 shows a well defined distribution with the desired rotational symmetry.

3.3. One-Hot Encoding

Another encoding worth investigating is the *One-hot encoding* (also mentioned in [Cha19]), which encodes a discrete variable into one-hot qubit, e.g. all qubits are pointing up while one is pointing down. The position of the hot qubit then indicates the value of the discrete variable, similar to the domain wall, where the position of the domain wall does the same. The disadvantage of the one-hot encoding is that it lacks a meaningful notion of distance, as all encoded vectors are located at the same Hamming distance from one another, with only two spin-flips needed to transform one vector into another. This property also enforces rotational symmetry in higher dimensions, which makes the encoding interesting to investigate, despite its flawed distance representation. The Hamiltonian for the One-hot encoding is given for a $\Lambda > 0$ by

$$H^{\mathrm{OH}} = \Lambda \left(\left[\sum_i^N \frac{1-\sigma_i^z}{2} \right] - 1 \right)^2 \propto \underbrace{\Lambda \left[1 - \frac{N}{2} \right]}_{\Lambda'} \left(\sum_i^N \sigma_i^z + \frac{1}{4\left[1-\frac{N}{2}\right]} \sum_{i,j}^N \sigma_i^z \sigma_j^z \right), \tag{3.24}$$

where N is the total number of qubits. Here, the equation is already rearranged in such a manner that the J-couplings and h biases can be obtained from it directly (for more details, see sec. A.2.4). This Hamiltonian ensures that at all times only one spin is in the $|\downarrow\rangle$ state, with eigenvalue -1, as this is the ground state that has the ground state energy $E_0 = 0$. It also suppresses wrong configurations with more than one spin pointing down quadratically, as the energy scales as $E_i = \Lambda i^2$, where i is the number of excess spins pointing downward. The J-couplings and h biases, obtained from the Hamiltonian, are given by

$$J_{i,j}^{\mathrm{OH}} = \frac{\Lambda}{4} \quad h_i^{\mathrm{OH}} = \Lambda \left[1 - \frac{N}{2} \right]. \tag{3.25}$$

It is immediately apparent that the h parameters scale with the system size which causes the problem that the h values will need to be *autoscaled* on the QPU. This means that if a value leaves the range defined by the annealer - in the case of the Advantage 6.4 the range is $[-4, 4]$ for the h parameters - all parameters will be scaled down accordingly so that all values lie within the range again. This indicates that as the system size increases, Λ takes smaller values and therefore the encoding becomes weaker due to weaker couplings, which results in more invalid configurations during the simulation. One can also turn this feature

off, but then either the maximum Λ value or the system size is limited, depending on which of the two one chooses to keep constant. Due to the all-to-all connectivity of the encoding, not only do the h parameters scale with system size, which, in a two-dimensional grid, is given by the squared number of qubits per axis for a two-dimensional lattice, but so does the required number of couplings. This will also result in an increased run time for larger system sizes. The encoded value is, conversely, retrieved by doing many measurements in the σ^z basis of all qubits and computing the following expectation value:

$$\langle \phi(\tau) \rangle = \frac{1}{2} \sum_{i=1}^{N} (\phi_0 + i\xi) \langle 1 - \sigma_i^z \rangle , \tag{3.26}$$

by simply determining the direction of all spins and applying the above formula, as only one spin is pointing down and this is the only one contributing to the sum with an eigenvalue of -1. Similar to the domain wall encoding, the potential can be encoded as

$$V(\phi(\tau)) = \frac{1}{2} \sum_{i=1}^{N} V(\phi_0 + i\xi)(1 - \sigma_i^z), \tag{3.27}$$

by simply inserting the discretized value into the potential and using it as a prefactor to the corresponding sigmas. The couplings and biases are then extracted with the help of an ancilla qubit, which is needed if the goal is to encode the potential solely in the biases or the couplings without mixing them. Instead, one could write $1 = \sigma_i \sigma_i$, but this would force the encoding to use both couplings and biases for the encoding of a specific potential. The goal is to be able to separately encode two potentials, with one being turned on for the whole duration of the process, while the other is turned off in the beginning, and turned on later using the h-gain. To that end, an ancilla qubit is necessary, which will be denoted as σ_0 in the state $|\uparrow\rangle$ with an eigenvalue of 1, which is achieved by applying a large negative bias to it. The resulting potential can be rearranged in two ways with respect to an encoding in either the biases or the couplings:

$$V(\phi(\tau)) = \begin{cases} \frac{1}{2} \sum_{i=1}^{N} V(\phi_0 + i\xi) \langle \sigma_0^z - \sigma_i^z \rangle & \text{for h parameters} \\ \frac{1}{2} \sum_{i=1}^{N} V(\phi_0 + i\xi) \langle \sigma_i^z \sigma_i^z - \sigma_i^z \sigma_0^z \rangle & \text{for J parameters} \end{cases} . \tag{3.28}$$

From the potential, the couplings and biases can be obtained as

$$J_{i,j}^{\mathrm{QFT}} = \frac{1}{2} V(\phi_0 + i\xi)(\delta_{i,j} - \delta_{i,0}) \qquad h_i^{\mathrm{QFT}} = \begin{cases} \frac{1}{2} \sum_{i=1}^{N} V(\phi_0 + i\xi) & \text{if } i = 0 \\ -\frac{1}{2} V(\phi_0 + i\xi) & \text{else} \end{cases} , \tag{3.29}$$

depending on which one of the two one wants to encode the potential in.

Unfortunately, as the encoding scales quadratically with the number of qubits per axis in a two-dimensional grid, it is not feasible to run it for a two-dimensional grid, as given in the previous sections. Firstly, because the number of all-to-all couplings, for a 32×32 grid with $N = 32^2$, already amounts to a total of 32^4 couplings which need to be embedded onto the DWave topology; as this problem of finding an embedding is *NP-hard*, it becomes increasingly

expensive for larger graphs with many couplings. Secondly, due to the scaling of Eq. (3.25), the encoding becomes weak and results in a growing number of faulty configurations. This can be seen if, for example, one sets $\Lambda' = -4$ in Eq. (3.24) for a 32×32 grid. In that case all the couplings will become $J_{i,j}^{\mathrm{OH}} = 511^{-1} \approx 0$, which is too small compared to the large h biases of -4 and will not have a considerable influence on the simulation.

3.4. Discussion

After extensive probing of different encodings, it is apparent that the most suitable encoding for this task is the one from subsection 3.2, in which two domain wall encoded spin chains are concatenated and each one represents one variable, i.e. one dimension. It incorporates all necessary symmetries such as being rotationally invariant under a rotationally invariant potential, expressed by having no biases toward a specific direction in space; this being in stark contrast to the exhibited biases of only one single spin chain encoded with the domain wall encoding and using different traversing techniques of the two-dimensional grid, as described in section 3.1. Additionally, for the coupled domain wall encoding, the number of qubits necessary scale linearly with the number of qubits per axis for a two-dimensional system, thus allowing for the simulation of larger system sizes, which is not the case for the single domain wall and one-hot encoding, as these scale quadratically with the number of qubits per axis. Especially the one-hot encoding has an all-to-all connectivity between all qubits, resulting in an enormous amount of necessary couplings for larger system sizes, which are needed for two-dimensional simulations, which makes the embedding onto the hardware graph rather impractical.

The coupled domain walls encode the distance in space using the Hamming distance of spin configurations, which is crucial for physical problems depending on spatial coordinates. This is not the case for the One-hot encoding, in which each pair of spin configurations has the same constant Hamming distance of two, and therefore being unsuitable to encode mechanisms such as tunneling in the way described above. For all of these reasons, the coupled domain wall encoding will be used in further simulations on the QPU.

For future research it is noteworthy that one does not need to stop with the concatenation of two domain wall chains but can perform it for arbitrarily many. This allows for the encoding of higher-dimensional problems as the number of dimensions is equal to the number of domain wall spins. Although it is currently not suitable for the simulation of dynamic systems because one needs the same amount of multi-qubit interactions as there are dimensions, e.g. a three-dimensional problem requires 3-spin interactions due to the encoding. Currently, there are no devices yet which implement multi-qubit interactions greater than two, but there might be some in the future.

4. Calibration

As the quantum simulations are run on a real device and which does not operate in an ideal environment, it is crucial to ensure that the machine is well calibrated. While for regular optimization problems this might not be a big concern, simulations of quantum systems are rather susceptible to noise and as a consequence, poor calibration can produce unsatisfactory results. Sources of noise can be diverse and range from stray magnetic fields of couplers on the D-Wave QPU [HJL$^+$10] that are too strong to defects in the material. The present noise and the resulting bias in its presence can be demonstrated well by performing a simple forward anneal for $120\mu s$, as depicted in Fig. 4.1, by using the coupled domain wall encoding from subsection 3.2 without any potential, and setting the all-to-all J-couplings of Eq. (3.23) between the two domain walls, which will hereafter be referred to as inter-domain wall couplings, to zero.

The essential idea is that, with the inter-domain wall couplings set to zero, one would expect a uniform distribution over all coupled domain wall states with some random noise at most, as depicted in Fig. 4.2b, as there should not be a bias toward some states because of the absence of the encoded potential, which would have introduced an energy splitting for the degenerate ground states. Instead one obtains Fig. 4.2a as a result, which is obtained by setting all inter-domain wall couplings to zero, while for Fig. 4.2b, these couplings have been completely removed from the couplings list sent to the QPU, so that these are not taken into account at all during the run. As is apparent from Fig. 4.2a, there is an anti-ferromagnetic bias between the coupled domain walls, as the points $(\phi, \psi) = (-1.87, 2)$ and $(\phi, \psi) = (2, -1.87)$ represent, respectively, the domain wall states $|\phi, \psi\rangle = |-1.87, 2\rangle = |10\cdots00\rangle \otimes |11\cdots10\rangle$ and $|2, -1.87\rangle = |11\cdots10\rangle \otimes |10\cdots00\rangle$, indicating a prevalence of systematic noise. The diagonal, on which the probabilities spread therefore contains the anti-ferromagnetic states between the two domain walls. Due to the large impact on the results, it is of great interest to understand the consequences from noise that one has to expect during the simulations, to quantize them, and to correct for the noise effectively. This will be investigated in the next sections, and methods will be presented on how to correct for these noises.

The following sections provide an overview of the approaches used to address the problem. At first, the application of the effective temperature model shall be discussed to establish a foundational understanding of the system by computing a canonical ensemble over all possible configurations. Based on these estimations, shimming is then applied to correct the previously determined imperfections and its limitations are discussed. Finally, spin reversal transformations are identified as the most effective solution to the challenges considered.

Remark 4 *To reduce noise and biases from specific embeddings of the problem on the physical QPU, the sample acquiring mechanism has been modified so that it is split into batches of 100 samples, where for each batch a new embedding is computed before a run.*

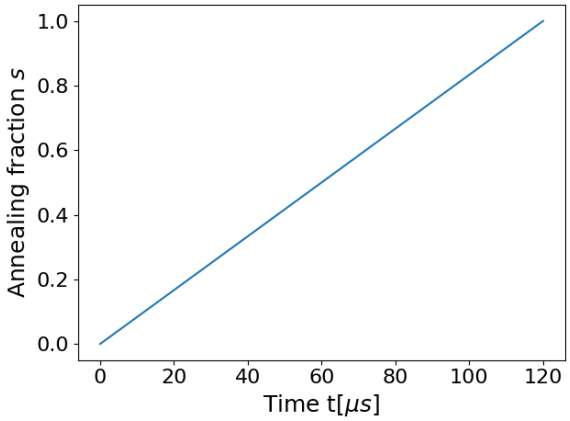

Figure 4.1.: Simulation forward-anneal schedule for the calibration test runs.

4.1. Canonical Ensemble

For a better understanding and quantization of the noise seen in Fig. 4.2a, it is convenient to define a model that reproduces the measured results. In this section, such a model is constructed and its results are compared to the measurements in Fig. 4.2. One such possibility for a model is to assume a thermal equilibrium and take a semi-classical Boltzmann distribution, as described and elaborated on in subsection 2.3.1. The distribution is then given by

$$p_{m,n} = \frac{1}{\mathcal{Z}} e^{-\beta E_{\text{config}}(m,n)} \qquad \mathcal{Z} = \sum_{m,n} e^{-\beta E_{\text{config}}(m,n)} \qquad \beta = \frac{1}{k_b T}, \tag{4.1}$$

with $p_{m,n}$ being the probability for a specific state, the indices of which will be explained below, E_{config} being the eigenenergy of the specific configuration, and T being an estimate of an effective temperature. Here, instead of just looking at a small subsystem, as was done in subsection 2.3.1, the whole system is taken into account in which a configuration is given over all qubits in the Hamiltonian. The Hamiltonian of interest is given by

$$H_{\text{P}} = H_{2DW} + J' \sum_{i,j}^{N} \sigma_i^z \sigma_{N+j}^z. \tag{4.2}$$

This is the problem Hamiltonian of the coupled domain wall encoding, combining Eq. (3.17) and (3.22). As mentioned above, no potential is encoded but instead a constant coupling J' was assumed for reasons of simplicity, which represents a general mean offset in the couplings between the qubits and accounts for the systematic noise seen in Fig. 4.2a. The resulting eigenenergies $E_{\text{config}}(m,n)$ can be deduced by analyzing the following eigenstates of the above Hamiltonian

$$|m,n\rangle = |\underbrace{11\cdots1}_{\times m}\ \underbrace{0\cdots0}_{\times(N-m)}\rangle \otimes |\underbrace{11\cdots1}_{\times(N-n)}\underbrace{0\cdots0}_{\times n}\rangle\,, \tag{4.3}$$

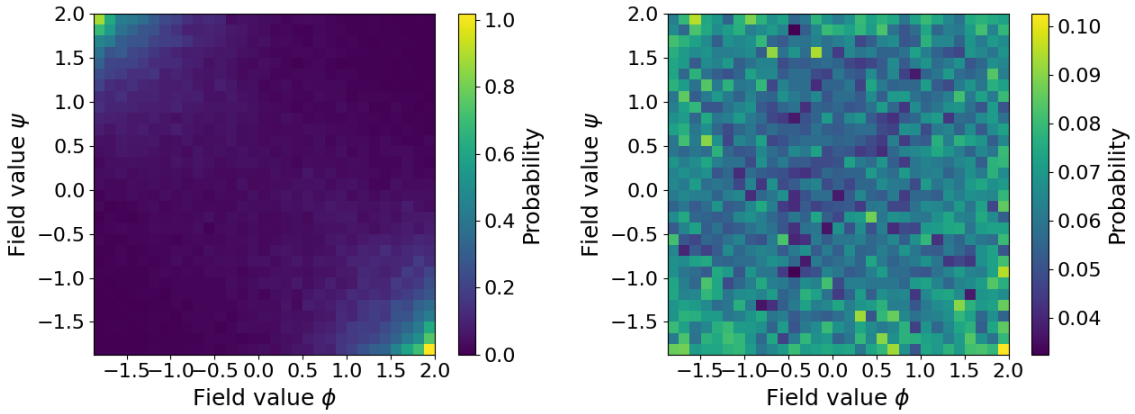

(a) Couplings between the two domain-walls set to zero.

(b) Couplings between the two domain-walls removed completely.

Figure 4.2.: Normalized probability densities, obtained from the QPU, with 50000 samples taken to check for some bias arising from uncalibrated couplings or h-biases. One can clearly notice an anti-ferromagnetic bias in Fig. 4.2a given by the probability being spread over the diagonal. For the run 32 qubits per axis and the schedule from Fig. 4.1 were used without any potential encoding.

where there are two domain walls with the first having m ones and the second having n zeros. These eigenstates are clearly degenerate ground states of H_{2DW}, as they represent two separate domain walls, thus having the same constant energy offset; but taking into account the last part of the problem Hamiltonian (which can also be regarded as a small perturbation), the energies undergo a splitting due to the error contribution. The splitting can be calculated as

$$E_\Delta(m,n) = \left[J'(N-n) - J'n\right] m + \left[-J'(N-n) + J'n\right](N-m) \tag{4.4}$$
$$= -J'\left[nm + (N-n)(N-m) - (N-n)m - (N-m)n\right] \tag{4.5}$$
$$= -J'(N-2m)(N-2n), \tag{4.6}$$

where all ferro- and anti-ferromagnetic contributions between the two domain walls are summed up with the correct sign in front of J' in the first line and then rearranged to a simpler form. Combining the general offset in the energy from the domain wall constraints and the energy splitting leads to the following equation for a specific configuration:

$$E_{\text{config}}(m,n) = 2E_{\text{DW}} + E_\Delta(m,n) \tag{4.7}$$
$$= -2\Lambda(N-3) - 4\Lambda' - J'(N-2m)(N-2n). \tag{4.8}$$

However, for the computation of the Boltzmann distribution, this constant energy offset can be neglected, as it is cancelled by the normalization. Consequently, only the energy splitting terms are relevant to the final distribution. With this in mind, using Eq. (4.1), one can numerically compute what would be expected if there were a slight mean offset in

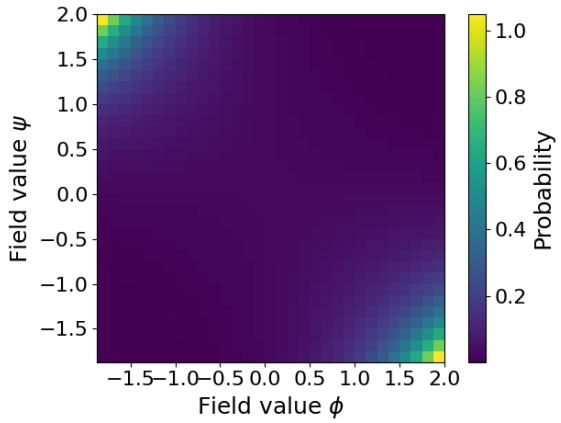

Figure 4.3.: Numerical computation of the Boltzmann density distribution for a mean error of $J' \approx 1.9 \cdot 10^{-3}$, $T \approx 187.4mK$, the energy is given in units of $[E] = 5.7 * 10^{-24} J$ and $N = 32$ qubits.

the J-couplings in the real device. Doing so for $J' \approx 1.9 \cdot 10^{-3}$, which introduces an anti-ferromagnetic bias, an estimated effective temperature of $187.4mK$, an energy unit obtained from Fig. 2.2a at $s = 1$, and 32 qubits per axis, one obtains the distribution depicted in Fig. 4.3. It is noticeable that this distribution is similar to the one from Fig. 4.2a, which indicates that the systematic noise observed there can, in fact, be modeled by an error arising from the coupling terms between the two domain walls.

Next, it will be investigated whether the assumption of an overall mean error on the couplings, denoted by J', is valid, or if one needs to model it by examining each coupling term and its error individually. To do this, one can determine the magnetization and correlator for each qubit and for each coupling between two qubits on the real device by performing a run with a forward-anneal schedule and setting all h and J parameters on the machine to zero, then averaging over all measurements. If only random noise is present, the magnetizations and correlators are expected to form a normal distribution around zero. Conversely, if there is a systematic offset, this would manifest itself as a shifted mean in the distribution.

Applying this procedure to the D-Wave QPU, with a forward-anneal length of $400\mu s$ and 20000 samples, yields the magnetization and correlator distributions over all individual qubit magnetizations and couplers, as displayed in Fig. 4.4. For both the magnetizations and the correlators one can see that the values measured on the QPU are normally distributed around a mean, which is -0.016 for the magnetizations and -0.02 for the correlators. While for the magnetizations the normal distribution is approximately symmetric around zero, due to the larger standard deviation of the magnetizations, making them more balanced in terms of possible negative and positive terms, the same cannot be said for the correlators. In contrast, the correlators are leaning more toward the negative region given by the negative mean and smaller standard deviation, supporting the theory, considered in combination with the normal distribution of the magnetizations being symmetric around zero, of an anti-ferromagnetic bias. Using Eq. (2.46) and (2.47) and rearranging them for J and h, one can infer that the

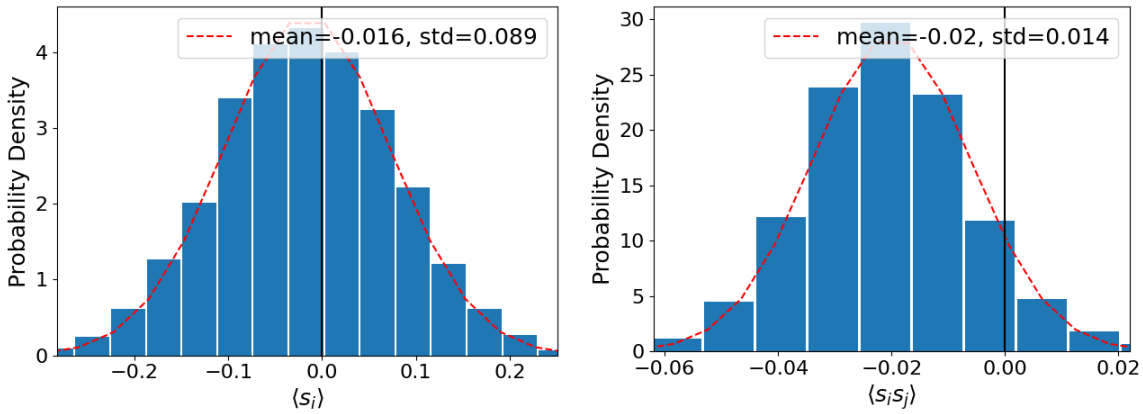

(a) Magnetization of all qubits on the QPU.

(b) Correlators between all coupled qubits on the QPU.

Figure 4.4.: Normalized probability densities of magnetizations and correlators measured on the DWave QPU by doing a forward anneal for $400\mu s$, taking 20000 samples and having all biases and couplers of the QPU set to zero.

reconstructed mean values for these runs were greater than, yet close to, zero. Firstly, this fulfills the condition required by Eq. (2.47), that the h parameters can be neglected when set to zero and, secondly, it supports the assumption that one can assume a mean J' offset as was done above, accounting for the systematic noise, resulting in the anti-ferromagnetic bias one could observe in Fig. 4.2a. With this, it is now possible to correct for the systematic noise in the couplers, which will be done in the following section.

Remark 5 *These noise statistics have been performed for a static set of parameters during the simulation runs which were set to zero. It is important to keep in mind that the observed offset can be dependent on the set and may vary for different values of h and J. These methods are not intended to quantify noise absolutely for specific devices, as it may change over time and depends on many factors; but rather it is there for temporal quantization and qualitative correction either during or before a run. Nevertheless, during the course of these experiments, the noise behaved in quite a stable manner, did not change much and always exerted the same anti-ferromagnetic bias.*

4.2. Shimming

In the previous section, the systematic noise has been examined and it could be concluded that it can be modeled as a systematic offset, primarily in the J couplings. One might try to correct for that by subtracting the offset from the affected couplings and biases. For this, one inverts (2.46) and (2.47) for the respective parameter and obtains the following equations

$$J_{i,j} = \operatorname{arctanh}(-\langle \sigma_i^z \sigma_j^z \rangle)/\beta \qquad h_i = \operatorname{arctanh}(-\langle \sigma_i^z \rangle)/\beta. \tag{4.9}$$

Algorithm 3 Iterative shimming procedure with forward annealing

1: Define fixed parameters $\{h_i^{\text{fixed}}\}$, $\{J_{i,j}^{\text{fixed}}\}$ and initial guess for effective temperature T
2: **repeat**
3: Perform a forward anneal with $\{h_i^{\text{fixed}}\}$, $\{J_{i,j}^{\text{fixed}}\}$
4: Compute magnetizations and correlators for all qubits and couplers
5: Compute updated h_i-biases and $J_{i,j}$-couplings according to Eq. (4.9)
6: Compute correction terms:

$$\Delta_i = h_i^{\text{comp}} - h_i^{\text{fixed}}, \quad \Delta_{i,j} = J_{i,j}^{\text{comp}} - J_{i,j}^{\text{fixed}}$$

7: Subtract correction terms from fixed parameters:

$$h_i^{\text{new}} = h_i^{\text{fixed}} - \Delta_i, \quad J_{i,j}^{\text{new}} = J_{i,j}^{\text{fixed}} - \Delta_{i,j}$$

8: Perform a forward anneal with updated parameters $\{h_i^{\text{new}}\}$, $\{J_{i,j}^{\text{new}}\}$
9: Update guess for effective temperature T based on results
10: **until** mean of resulting normal distributions for the magnetizations and correlators equals the expected means depending on the set $\{h_i^{\text{fixed}}\}$ and $\{J_{i,j}^{\text{fixed}}\}$

There is a caveat to this approach: one has to estimate the effective temperature which is crucial for getting an accurate correction for this method. The temperature will be estimated and adjusted by comparing the magnetization and correlator distribution curves, whose forms are similar to Fig. 4.4), to the expected curves, which are normal distributions with a mean of zero. This is done in an iterative process, by performing a manual form of gradient descent which, in turn, will also yield the correction terms for the calibration. This procedure is summarized in Algorithm 3, in which the temperature is the fitting parameter. This results in a set of correction terms, which then in turn will be used, as in line 7 of Algorithm 3, as a calibration for each run on the QPU. Performing the procedure described in Algorithm 3, by setting the fixed set of parameters for h_i^{fixed} and $J_{i,j}^{\text{fixed}}$ to zero, using a forward anneal length of $400\mu s$ and taking 20000 samples per run, produces the final magnetization and correlator distributions that can be seen in Fig. 4.5a and 4.5b. The energy unit was taken to be approximately $[E] = 5.7 * 10^{-24} J$, according to Fig. 2.2a, with a final effective temperature of $T \approx 63mK$, which was retrieved after several iterations of comparing the given distribution to the expected distribution. One can see that for both the magnetizations and correlators, the mean shifts closer to zero, the expected mean for biases and couplers set to zero. Another observation one can make is that the deviations in the normal distributions increased, which might be explained by the manner in which the corrections are currently performed. As they are performed individually for each bias and coupler, the value which is used for the individual correction is fixed, while the real error on the machine for a run is likely probabilistic and governed by the distributions given in Fig. 4.4. Thus it is possible for the correction value to be, for example, $\mu - 2\sigma$ for the qubit i (analogous for the couplers), where μ is the mean and σ is the standard deviation, but the actual error during this run on this bias might already be around $\mu + 2\sigma$ resulting in an overall error of 4σ instead of canceling, thus spreading the

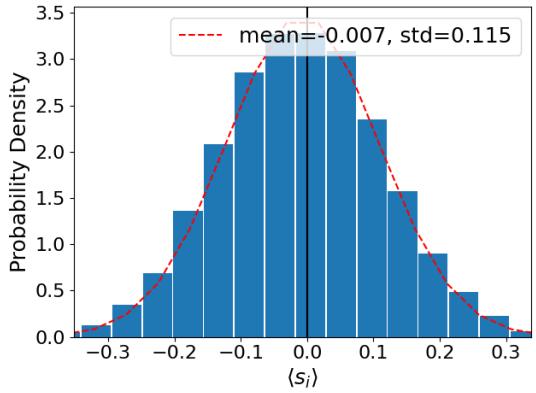

(a) Magnetization after individual per-qubit correction.

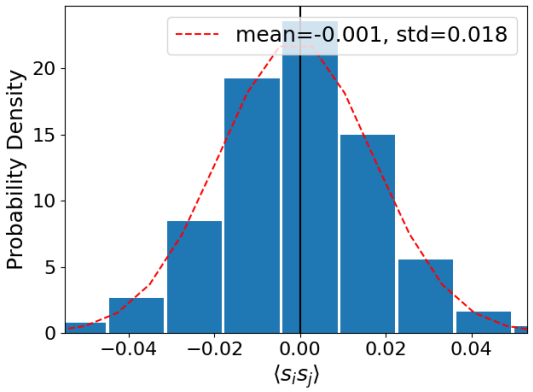

(b) Correlators after individual per-coupler correction.

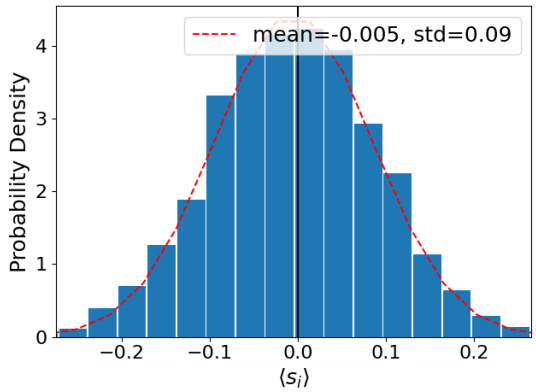

(c) Magnetization after mean offset correction.

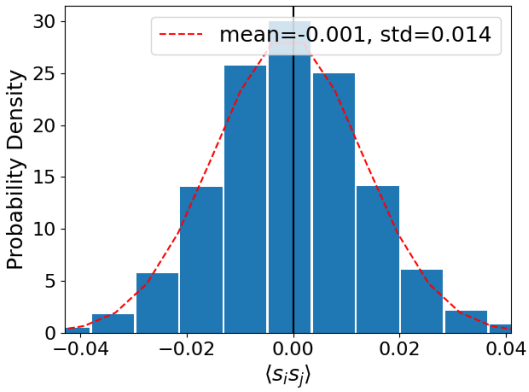

(d) Correlators after mean offset correction.

Figure 4.5.: Magnetization and correlator distributions after applying an individual per-qubit/coupler correction and an overall mean offset correction, which constituted computing the mean J offset of the couplers and subtracting it from all couplers. The mean offset terms were both of order $\approx 10^{-3}$, while the per-spin/coupler correction terms ranged between $\approx 10^{-3} \cdots 10^{-2}$, all computed with a guessed effective temperature $T \approx 63mK$ and an energy unit of $[E] = 5.7 * 10^{-24} J$ according to Eq. (4.9).

distribution on both sides and resulting in an overall larger deviation. This problem can be solved easily by correcting with the mean over all computed h_i and $J_{i,j}$ offsets, given in the figures 4.4 by the mean of the distributions, instead of correcting every bias and coupler individually. In turn, this should shift the distribution without having an effect on the standard deviation and avoiding overcorrection. The resulting distributions from these modifications can be seen in figures 4.5c and 4.5d, in which it is apparent that the standard deviations for the distributions stay the same, while the means shift toward zero.

Applying this calibration to the simulation of the coupled domain wall encoding, which

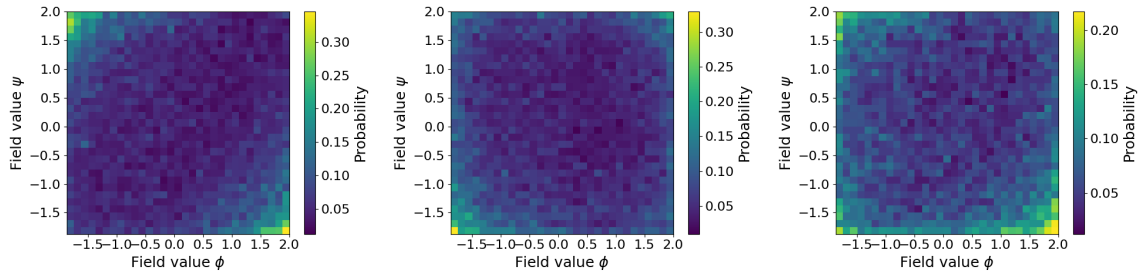

(a) Regular calibration

(b) Overshooting calibration by choosing $1.25 \cdot \overline{J}$ as the correction term.

(c) Adjusted calibration by choosing $1.125 \cdot \overline{J}$ as the correction term for reaching the sweet point.

Figure 4.6.: Normalized probability densities after re-executing simulation runs of Fig. 4.2a with regular and overshooting calibration. One can see a diminished antiferromagnetic bias in 4.6a while seeing a ferromagnetic bias in 4.6b. Runs have been done taking 50000 samples for 32 qubits per axis.

is depicted in Fig. 4.2a, together with the annealing schedule from Fig. 4.1, results in the probability density for the domain wall states depicted in Fig. 4.6a. Here, it is visible that there still is an anti-ferromagnetic bias, but it is much weaker when comparing the magnitudes of the probability densities to Fig. 4.2a, which shows that the calibration is showing the desired effect qualitatively. If the calibration for the J-parameters (as shown in Fig. 4.3; this is the main contribution to the anti-ferromagnetic bias one observes) is 'overshot' - meaning, for example, that one doubles the mean correction term for the J-parameters to achieve a larger correction toward the ferromagnetic bias - one can see in Fig. 4.6b that one indeed retrieves a probability density with a ferromagnetic bias. This implies that somewhere in the range $[\overline{J}, 1.25 \cdot \overline{J}]$, with $\overline{J}$ being the mean J correction term, lies the *sweet point*, where there is neither a ferro- nor an anti-ferromagnetic bias in the probability densities. Adjusting the correction term to $1.125 \cdot \overline{J}$ one retrieves the probability density in Fig. 4.6c, which closely resembles the desired uniform distribution. Yet it does not perfectly conform to a uniform distribution, seeing that the edges of the grid have a slightly higher probability than the center, which was also already prevalent in Fig. 4.2b. As [CCD+22] shows for the one-dimensional case, this parabolic distribution arises when taking into account noise arising from stray magnetic fields of free spins and defects in the material of the QPU. Because in the given case two one-dimensional chains are linked, it is highly probable that this effect also occurs in this setup in form of higher probabilities at the edges, especially at the corners where the superposition of the two parabolas is maximal - even after calibration, as in [CCD+22]. This persistency in the noise originates from its statistical nature with an average of zero, so that the main contributing part is the variance of it in contrast to systematic noise, where the offset of the mean from zero is the driving force and can thus be corrected with the above described procedure. Another observation one can make is the absence of probability in the top right corners of figures 4.6b and 4.6c, which indicates a bias in the ferromagnetic regime

toward the mostly all-up domain wall state. This can be explained by some sort of residual offset in the h-biases which has not been fully corrected, pushing the system toward the state in the lower left corner, while not having a significant effect on the anti-ferromagnetic states, as it does not introduce an energy splitting between them, due to their symmetry. This shows that one can indeed correct the shown bias in Fig. 4.2a to some extent with the proposed procedure. Nevertheless, it requires several iterations and a careful estimate of the temperature, and even with that, it is not certain if these correction terms are valid for the whole h and J ranges that are possible on the QPU, which also might explain why, after retrieving Fig. 4.5, one still has to adjust the temperature once more, as shown in Fig. 4.6.

Remark 6 *For future reference: The effective temperature for the qubits can be estimated as described in [JAG+11] (Supplemental Information, section II.D page 8.), in which, for every qubit, a sweep over an h range is performed, the magnetization is computed from the QPU data, the curves are shifted to have the same centers and then the averaged data is fitted to a hyperbolic tangent as depicted in Eq. (2.46), in which the temperature is the fitting parameter.*

This method would not replace the iterative process described in Algorithm 3, as the need for verification of the resulting correction terms, based on the deduced effective temperature, is still necessary. During this verification, the need for further refinement might still arise. That is why the method mentioned in the previous paragraph constitutes an additional step, which goes beyond the extent of this work.

4.3. Spin Reversal Transformation

The procedure of the previous section already yields satisfactory results with respect to mitigation of errors but it includes many caveats, such as costly retrieving the effective temperature in many iterations. It also does not provide certainty of the calibration by just looking at the correlator and bias distributions, as is apparent from the mean correction coupler term requiring readjustment during the simulations of the coupled domain walls to get the expected distribution. Lastly, it is not clear if this calibration also holds for h and J parameters other than the ones for which the calibration has been performed. For these reasons, it is of great interest to explore other correction methods. One such method is the *Spin-reversal transformation* [BRI+14], which includes running the problem in several batches while simultaneously applying gauge transformations to random qubits. It has the great advantage that, firstly, it does not rely on any fitting and, secondly, it is simple to implement. The only caveat of this method is that it does not allow for quantization of the noise and the estimation of the effective temperature on the QPU, which, here, is not a problem, as the objective is to perform error mitigation and reduce any noise which could bias the simulations.

Given a problem with N qubits, the transformation consists of flipping qubits by a randomly chosen bit string $g \in \{\pm 1\}^N$, where $+1$ leaves the qubit as it is, and -1 flips its h bias and couplings according to

$$h_i \to g_i h_i \qquad J_{i,j} \to g_i g_j J_{i,j}. \tag{4.10}$$

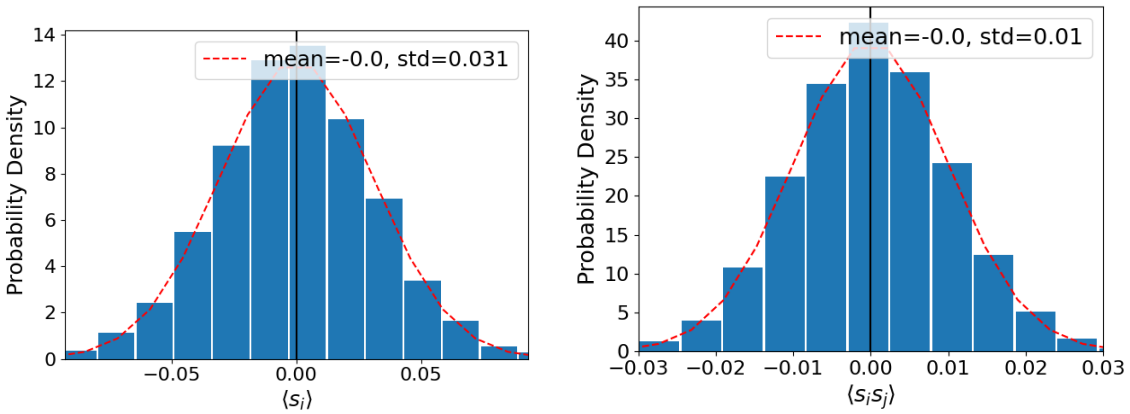

(a) Magnetization of all qubits on the QPU.

(b) Correlators between all coupled qubits on the QPU.

Figure 4.7.: Normalized probability densities after applying the Spin-Reversal transformation, measured on the DWave QPU by doing a forward anneal for $400\mu s$, taking 20000 samples and having all biases and couplers of the QPU set to zero.

This transformation has no effect on the problem and the dynamics of it, while the results of the transformed and original problem are still related through $s_i = g_i s'_i$ with preserved energy. As a consequence, when averaging the results over many batches, the systematic noise offsets can be averaged out. Having a look at the problem Hamiltonian of Eq. (2.44), one can see that it can be written as the sum of many local Hamiltonians over two qubits given by

$$H_{\mathrm{P}} = \sum_{i,j}^{N} \underbrace{J_{i,j}\sigma_i^z\sigma_j^z + \frac{h_i}{2N}\sigma_i^z + \frac{h_j}{2N}\sigma_j^z}_{H_{i,j}^L}. \tag{4.11}$$

Analyzing this local Hamiltonian in terms of how it behaves under the gauge transformations, one can first group the possible random bit strings into two groups of equal probability, i.e. the anti-ferromagnetic transformations $(g_i, g_j) \in \{(1,-1),(-1,1)\}$, where only one spin is flipped, and the ferromagnetic transformations $(g_i, g_j) \in \{(1,1),(-1,-1)\}$, where either both are flipped, or none are flipped. Then with this, one can compute the average over an AFM gauge transformation and an FM gauge transformation of the local Hamiltonian, denoted by a line over the local Hamiltonian

$$\overline{H_{i,j}^{\mathrm{L,\ J}}} = \underbrace{\frac{1}{2}\left[(-J_{i,j} + J_{i,j}^{\mathrm{off}})(-\sigma_i^z\sigma_j^z)\right]}_{\text{antiferromagnetic}} + \underbrace{\frac{1}{2}\left[(J_{i,j} + J_{i,j}^{\mathrm{off}})(\sigma_i^z\sigma_j^z)\right]}_{\text{ferromagnetic}} = J_{i,j}\sigma_i^z\sigma_j^z, \tag{4.12}$$

where Eq. (4.10) along with the back-transformation $\sigma_i^z = g_i\sigma_i'^z$ were applied. As expected, after averaging, the constant systematic offset $J_{i,j}^{\mathrm{off}}$ is successfully removed. Again, it is assumed that there is a constant systematic offset $J_{i,j}^{\mathrm{off}}$ on the individual couplings, similar

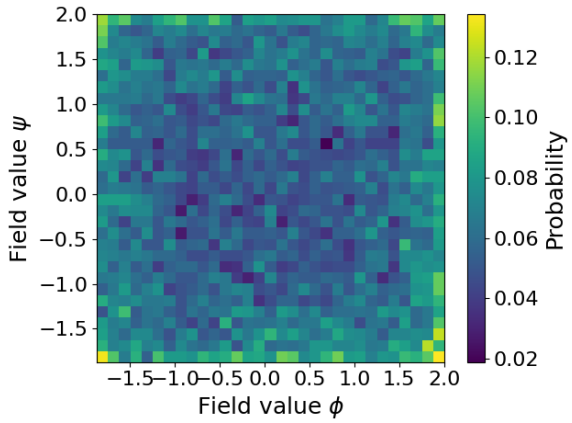

Figure 4.8.: Normalized probability density after re-executing simulation runs of Fig. 4.2a and applying the Spin-Reversal transformation. For the run 32 qubits per axis and the schedule from Fig. 4.1 were used without any potential encoded.

to Fig. 4.4b, which is responsible for the bias. This assumption is backed by the findings of the previous section, where one can clearly see, despite the fact that it was done for the whole ensemble over all magnetizations and correlators, that the noise is normally distributed around some mean offset, which is represented by the constant offset in the equation above. Analogously, the same can be done for the spin biases, for which there are only two possible transformations $g_i \in \{1, -1\}$, resulting in the following average over AFM and FM gauge transformation

$$\overline{H_i^{\mathrm{L,\,h}}} = \frac{1}{2}\left[\left(-\frac{h_i}{2N} + h_i^{\mathrm{off}}\right)(-\sigma_i^z)\right] + \frac{1}{2}\left[\left(\frac{h_i}{2N} + h_i^{\mathrm{off}}\right)\sigma_i^z\right] = \frac{h_i}{2N}\sigma_i^z. \tag{4.13}$$

As this holds for the local Hamiltonian, it is extendable to the global problem Hamiltonian, which shows that the systematic noise can be corrected completely in this way, as long as the assumption of a constant systematic offset holds.

Repeating the same simulations in combination with the spin reversal transform as in the previous section for the magnetization and correlator distributions, with a $400\mu s$ forward anneal, 20000 samples and all biases and couplings set to zero, yields the distributions depicted in Fig. 4.7. Here, one can clearly see that the mean for the magnetization as well as for the correlators is centered around zero, and even the deviations decrease compared to Fig. 4.5c, likely because this method averages out the error on an individual spin/coupling level and not for the whole ensemble of all spins and couplers in the form of a single constant correction term, resulting in less over- or under-correction. This effect could probably have been achieved by extending the method of the previous section onto the individual spin/correlator level by computing the distributions for every single bias and coupler, but this would have been more demanding in comparison to the gauge transformations. Applying the spin reversal transforms to the same simulation of the coupled domain wall as in Fig. 4.2a, in which one sets the coupling terms between the two domain walls to zero, results in Fig. 4.8. Here, one

can clearly see that the state distribution follows an almost uniform distribution, without a bias toward any particular direction, since the distribution appears to be rotation-symmetric, though with slightly higher probabilities at the edges than at the center, as also noted in the previous section. The latter effect should cease to be the dominant contribution once a potential is encoded, splitting the eigenenergies of the degenerate ground-state space, so that the main contribution to the final probability density comes from the encoded potential, instead of fluctuations in the couplers or h-biases. All in all, the spin reversal transform should be sufficient to eliminate the direction bias in the following quantum simulations. Therefore, this work shall restrict itself to only using this technique going forth, as for the purpose of this work it is superior to the technique presented in the previous section.

5. Numerical solutions

To get a sense of what to expect from the false vacuum decay runs on the QPU, which will be done later in chapter 6, it is of great interest to solve Eq. (2.38) numerically for the following potential in two dimensions

$$\frac{2}{\hbar^2}V(\vec{\phi}) = \underbrace{l(l+1)\tanh^2(|\vec{\phi}|) - l\frac{\tanh(|\vec{\phi}|)}{|\vec{\phi}|}}_{V_l} + \underbrace{\left(-g(g+1)\mathrm{sech}^2(|\vec{\phi}-\vec{b}|) - g\frac{\tanh(|\vec{\phi}-\vec{b}|)}{|\vec{\phi}-\vec{b}|}\right)}_{V_g}, \tag{5.1}$$

which also will be used later on for the QPU runs. The potential is a combination of two wells, V_l and V_g, governed by Eq. (2.42), where m and c are set to one for simplicity and tanh is expressed as a sech by the $1 = \tanh(x)^2 + \mathrm{sech}(x)^2$ relation, and $\vec{b}$ is the position of the second well in two-dimensional space. As the simulations of the one-dimensional quantum field theory are performed for two fields simultaneously, the equations of motion in Eq. (2.31) simplify to

$$\ddot{\vec{\phi}}(t) = \left.\frac{\partial^2\vec{\phi}}{\partial t^2}\right|_t = \left.\vec{\nabla}V\right|_{\phi^i=\phi^i(t)}. \tag{5.2}$$

The derivative of the potential can be obtained by computing the derivative for the two single wells and then combine them accordingly. The derivatives should only differ in some offset in the field value, as the description of the two wells are connected by a transformation using the aforementioned trigonometric identity. Thus, the derivatives for the wells are given by

$$\vec{\nabla}V_{n\in\{l,g\}}(\vec{\phi}) = 2n(n+1)\tanh(|\vec{\phi}|)\mathrm{sech}^2(|\vec{\phi}|)\frac{\vec{\phi}}{|\vec{\phi}|} - n\mathrm{sech}^2(|\vec{\phi}|)\frac{\vec{\phi}}{|\vec{\phi}|^2} + n\tanh(|\vec{\phi}|)\frac{\vec{\phi}}{|\vec{\phi}|^3}, \tag{5.3}$$

and combined, Eq. (5.2) becomes $\ddot{\vec{\phi}}(t) = \vec{\nabla}V_l(\vec{\phi}) + \vec{\nabla}V_g(\vec{\phi}-\vec{b})$. An example of the potential can be seen in Fig. 5.1, where the parameters are chosen to be $\vec{b} = (2.5, 2.5)$, $g = 3/4$ and $l = 1/2$. This form of the potential is picked, because the analytical solutions of the Schrödinger equation for the single wells are known, as discussed in subsection A.2.2, and also because, when combining them, it is simple to model a local and a global minimum. Distinct global and local minima are necessary to observe a false vacuum decay of the metastable state from the local into the global minimum, as otherwise one would expect non-negligible oscillations, as described in remark 1, without the possibility of trapping the probability through thermalization (see remark 2) in the global minimum after tunneling has occurred. This should effectively simulate the open potential as in Fig. 2.1b, mitigating oscillations, and allowing for a more precise computation of the decay probability per unit time. Still,

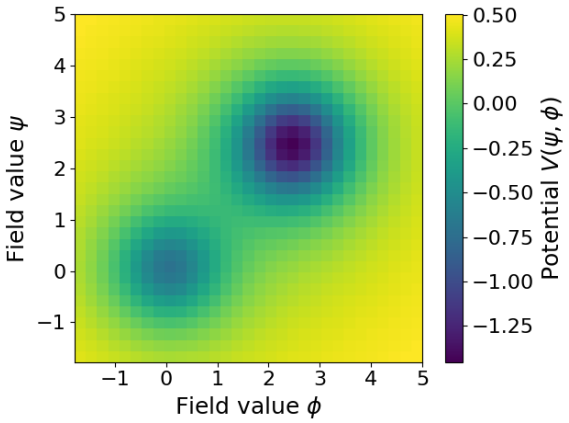

Figure 5.1.: Potential of Eq. (5.1) in two dimensions, with $\vec{b} = (2.5 \quad 2.5)^T$, $g = 3/4$ and $l = 1/2$.

one has to keep in mind that oscillations will occur nonetheless, as the thermalization process does not happen instantaneously.

The process of solving the integral of Eq. (2.38) numerically consists of two steps, repeated in a loop for different positions of the second well. For all $\vec{b}$ in some predefined array:

1. Compute the dominating classical path of the particle from ϕ_a to ϕ_b with the *Velocity-Verlet* algorithm.

2. Solve the integral of Eq. (2.38) with the previously computed path.

which will be addressed in the following sections.

Remark 7 *Rewriting the potential in Eq. (2.42) to incorporate a sech instead of a* tanh *also entails that the eigenenergies transform from* $\frac{2m}{\hbar}E = l \to -l^2$. *This is a direct consequence of inserting* $\tanh(x)^2 = 1 - sech(x)^2$ *and absorbing the resulting constant of* $l(l+1)$ *into the energy term.*

5.1. Velocity-Verlet Algorithm

The Velocity-Verlet algorithm [SABW82] is a widely used numerical method for integrating Newton's equations of motion, particularly in molecular dynamics simulations [KMV22]. It offers a balance between computational efficiency and accuracy by updating both positions and velocities of particles in a time-reversible and symplectic manner. In comparison to basic Euler methods, which are the naive way of solving differential equations, the Velocity-Verlet approach minimizes the accumulation of numerical errors over long simulations, preserving energy more effectively. By incorporating information about the system's accelerations at both the current and predicted positions, this algorithm constitutes a robust technique for simulating the dynamics of physical systems. This is crucial for solving Eq. (2.38), due to

the dependence of the integral on the classical path from $\phi_a \to \phi_b$, governed by the potential of Eq. (5.1) and the equations of motions in Eq. (5.2).

For some given initial values $(\vec{\phi}(0), \dot{\vec{\phi}}(0)) = (\vec{\phi}_0, \dot{\vec{\phi}}_0)$, the algorithm starts by computing the velocity at a given half-time step, which is given by

$$\dot{\vec{\phi}}\left(t + \frac{\Delta t}{2}\right) = \dot{\vec{\phi}}(t) + \frac{1}{2}\ddot{\vec{\phi}}(t)\Delta t, \tag{5.4}$$

where Δt denotes the length of a single time step. This is then in turn used to update the field to the new value, which is done using

$$\vec{\phi}(t + \Delta t) = \vec{\phi}(t) + \dot{\vec{\phi}}\left(t + \frac{\Delta t}{2}\right)\Delta t = \vec{\phi}(t) + \dot{\vec{\phi}}(t) + \frac{1}{2}\ddot{\vec{\phi}}(t)\Delta t. \tag{5.5}$$

Having the newly updated field value, this will be used for the derivation of the acceleration at $t + \Delta t$

$$\ddot{\vec{\phi}}(t + \Delta t) = \vec{\nabla} V\Big|_{\vec{\phi}=\vec{\phi}(t+\Delta t)}, \tag{5.6}$$

which is then used for the computation of the updated velocity at a full time step

$$\dot{\vec{\phi}}(t + \Delta t) = \dot{\vec{\phi}}\left(t + \frac{\Delta t}{2}\right) + \frac{1}{2}\ddot{\vec{\phi}}(t + \Delta t)\Delta t = \dot{\vec{\phi}}(t) + \frac{\ddot{\vec{\phi}}(t) + \ddot{\vec{\phi}}(t + \Delta t)}{2}\Delta t. \tag{5.7}$$

This method is mathematically equivalent to the Verlet algorithm; however, it possesses several advantages, such as computing the field and velocity at the same time, and explicitly keeping track of the velocity without the need of extra computations and estimations, resulting in a more stable description of the system. Additionally, it mitigates numerical round-off errors due to the absence of subtractions of large, nearly equal numbers, and instead computes the updated values in small incremental steps. Moreover, due to the independence of the formulas on the previous time-steps and its reliance only on the current time, the algorithm is self-starting and does not require another method to compute the first time-step. Finally, the local truncation error for this method amounts to $\mathcal{O}((\Delta t)^3)$ while the global error is of order $\mathcal{O}((\Delta t)^2)$.

5.2. False Vacuum Decay

The False Vacuum Decay becomes apparent when studying several iterations of a metastable decay for the potential given by Eq. (5.1), for which the initial state is positioned in the local minimum, at various positions of $\vec{b}$, and then plotting the results against the distance between the local and global minimum. For each iteration, as described above, the classical path is computed using the Velocity-Verlet algorithm and then Eq. (2.38) is being integrated numerically with the trapezoidal rule being applied. The initial values in each run are the field value at the local minimum and a velocity of zero. It is important to note that the local minimum for small $\vec{b}$ is not necessarily at $|\vec{\phi}| = 0$, as the wells are shifting toward each

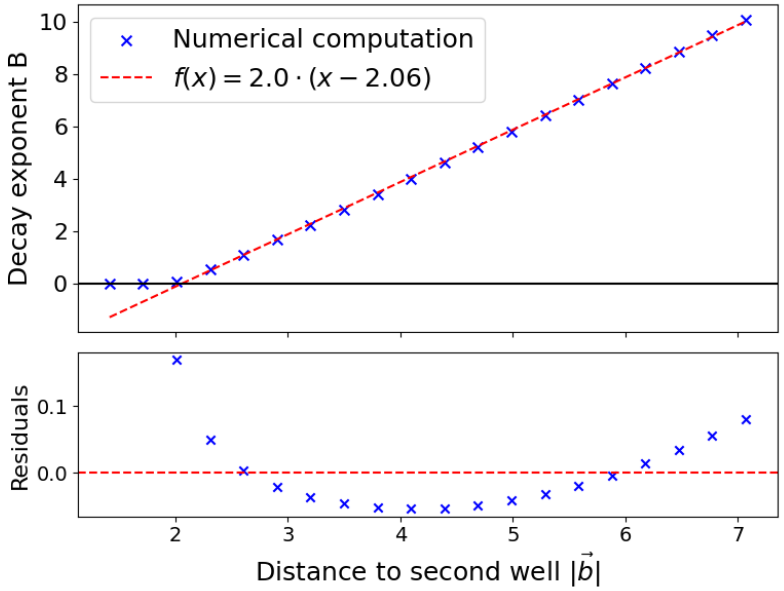

Figure 5.2.: Numerical results for the computation of the decay exponent from Eq. (2.38), in combination with Eq. (5.1), where $l = 1/2$ and $k = 3/4$ were chosen. The computed values are given by the crosses and the dashed line represents a linear fit for the last ten values.

other due to the superposition of the potential, as can also be discerned weakly in Fig. 5.1. That is why it is necessary to compute the position of the local minimum at least for small values of $\vec{b}$ at the beginning of each run, instead of setting it to the expected value for a single well at $\vec{0}$. After the computation of the position of the local minimum, it must be verified, as it is possible that, due to numerical inaccuracy, the computed value does not coincide precisely with the position of the actual minimum, and shows a slight deviation. This might induce, quite evident in the example of the inverted potential, a gradient toward the opposite direction of the second well. Yet it may be countered by adding a small offset toward the global minimum.

Having the initial state $(\vec{\phi}(0), \dot{\vec{\phi}}(0)) = (\vec{\phi}_a, 0)$, the classical path is computed until it reaches the escape point on the other side of the potential barrier with a velocity of zero, as given by the boundary conditions in Eq. (2.30). One caveat remains: when the two wells are close to each other, there is no barrier which forms for small $\vec{b}$, and the square root becomes imaginary in Eq. 2.38. Hence the imaginary part of the ground state energy vanishes and Eq. (2.21) becomes zero. For such cases, the distinction between local and global minimum and thus the distinction between wells is lost and the previous metastable state ceases to exist. During the numerical computation of such a case, one proceeds by setting the decay exponent to zero if encountered.

Executing this procedure with a time-step length of $\Delta t = 10^{-3}$ and sufficiently small values of $\vec{b}$ along the diagonal from $(0, 0)$ to $(5, 5)$ (the specific choice of $\vec{b}$ should not matter, as

the potential is rotation-symmetric around each well) helps to minimize error accumulation, as the classical paths remain sufficiently short. With $l = 1/2$ and $g = 3/4$ chosen as the potential in Eq. (5.1), one obtains Fig. 5.2, where the exponent is plotted against $|\vec{b}|$. It is clear that the behavior can be described by a linear function, as given by the dashed red line in the figure, while the residuals between the fit and the numerical values are close to zero in comparison to the actual values. The residuals exhibit an oscillating behavior, which might be explained by a systematic error originating from the numerical techniques used to solve the integral. Inserting this linear behavior into the decay probability per unit time γ from Eq. (2.25) results in a function showing exponential decay and depending on the distance between the local and global minimum.

6. Quantum simulations

With the theoretical background in place as well as its predictions for the decay experiments, this chapter shall now explore and probe theory and predictions by performing several experiments on the *D-Wave Advantage System 6.4*. For each run the spin reversal transformation of section 4.3 shall be used here, as it was found to be the most efficient and simple error mitigation technique, combined with the coupled domain wall encoding of subsection 3.2. The experiments will consist of simulating the double well potential from Eq. (5.1), with $l = 1/2$, $g = 3/4$, $m = 1$ and $c = 1$, but with varied positions of the global minimum, in the same diagonal manner as was used in section 5.2. Additionally, to test whether the rotational symmetry of the problem is conserved during the simulations, the global minimum will be moved along a spiral path. For each position in the run where a diagonal shift is performed, there is a corresponding position in the spiral shift which has the same distance to the local minimum.

In the following, the methodology will be explained on how the simulation runs on the QPU are performed and how the decay from the local into the global minimum is obtained, based on the probability density from experimental data. Then, in the following section, both decay rates, for the diagonal as well as the rotational shift will be analyzed and compared to each other. And lastly, the question will be raised on whether the process which takes place is due to the quantum nature of the annealer, or else might be explained by thermal effects.

6.1. Methodology

In this section, the methodology of how the experimental simulation runs have been performed on the D-Wave QPU is going to be explained, along with the post-processing of the data, as well as how the decay of the metastable state is extracted. Firstly, each run is performed using the spin-reversal transformation which needs to be run for a sufficient amount of batches, which is dependent on the system parameters. Secondly, the coupled domain wall encoding is employed and only configurations which represent valid coupled domain wall states are used after the run, whereas non-valid configurations, which, as shall be demonstrated, make up around 10% of all states in the following simulations, are filtered out and not used at all. Afterwards, the probability is renormalized over the remaining states. The annealing schedule for each run will consist of two linear ramps, down from $s = 1$ to $s_{\min} = 0.35$ and then reversely from $s_{\min} = 0.35$ to $s = 1$. Each ramp process takes $20\mu s$. In the meantime, the system is kept at $s_{\min} = 0.35$ for $60\mu s$, allowing the decay to take place. The initial state at $s = 1$ is the domain wall state, representing the position of the local minimum.

There are several ways to determine whether the probability mass should be classified as belonging to the local or the global minimum based on the corresponding potential. One

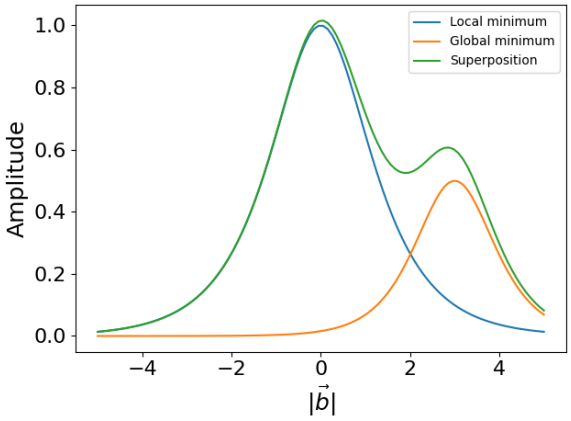

Figure 6.1.: Exemplary overall probability density with the individual contributing peak distributions trapped in the single wells on the cross-section where the two peaks lie.

option is to apply a rather simplistic approach using masks; a process in which, in this case with two wells in the potential, each cell is assigned to one of two clusters, i.e. the masks representing each of the wells. This can be done either using a clustering algorithm, assigning each cell to the closest cluster center, which are the known positions of the potential wells, or by splitting the surface using a straight line, which is computed based on some predefined procedure. One such procedure is that one takes the vector $\vec{b}$ connecting the two wells, so that at some place on the vector there is the maximum between the wells; the maximum is computed, and the plane in which the maximum lies and to which the connecting vector is orthogonal effectively splits the space in two halves, in each of which a well is located. These masks would then be applied, in turn, for computing the peak clusters in the probability density.

The procedure described in the previous paragraph, on the one hand, requires prior knowledge of the positions of the wells in the potential, which one has, but on the other hand would also neglect the experimental data, which might show a slight shift in positions for the peaks, relative to the well positions.

This approach appears to be simple, but it has two caveats, the first one being one of the points just made: if the two peaks are close to each other, they will start to overlap and the probability between them becomes indistinguishable, making it impossible to determine, to which of the peaks it belongs. An illustration of the overlap is provided in Fig. 6.1, in which for reasons of clarity a cross section is taken in the plane perpendicular to the ϕ–ψ-plane and containing the vector connecting the two peaks. If taking the straightforward approach with the masks, probabilities might be assigned to peaks they do not belong to, so that, for example, if splitting the area at approximately $|\vec{b}| = 2$, both peaks will be assigned probabilities of the other peak, thus skewing the tunneling fraction.

Secondly, it does not necessarily yield reliable results for the computation of the decay over $|\vec{b}|$, because when employing the antiparallel vector, $\vec{b}_{\text{global}} \rightarrow -\vec{b}_{\text{global}}$, in the mask

computation, one can still observe an exponential decay. This effect likely arises because, as the separating plane is shifted further outward from the relevant region of the peaks, cells from the distal tail of the local minimum are still clustered together. As a result, the computed fractions continue to exhibit an apparent exponential decay, even though both peaks lie on the same side of the boundary.

The situation can be better understood by examining Fig. 6.1. Here, if the antiparallel vector between the local and global minimum is used for computing the tunneling fraction, one can see that for increasing distances between the peaks, the area below the tail decreases exponentially. From this it is apparent, that the computed masks are not necessarily consistent with or indicative of the actual peaks, hence requiring a manual check in advance in order to ensure meaningful results.

As manual checks aren't feasible, a more sophisticated method is needed: instead of using masks for splitting the surface into two areas representing the peaks, one employs a different approach in which masks are used to determine the probabilities around the two peaks, which are then in turn fitted to the expected ground state probabilities. The expected ground state for one peak is given in Eq. (2.41) of which the squared absolute value needs to be calculated to retrieve the probability, which is then used to construct the fitting function for one peak

$$y(|\vec{\phi}|, A, l, c, \vec{\mu}) = A \cdot \operatorname{sech}^{2l}(c \cdot |\vec{\phi} - \vec{\mu}|), \tag{6.1}$$

where $\{A, l, c, \vec{\mu}\}$ are fitting parameters; the normalization constant is left arbitrary to ensure another degree of freedom. As two peaks are to be expected, the fitting function will consist of two of these ground state peaks combined in the following manner $\hat{y} = y(|\vec{\phi}|, A, l, c_1, \vec{\mu}_1) + y(|\vec{\phi}|, B, g, c_2, \vec{\mu}_2)$ and fitted around an area around the peak centers, large enough to capture the ground state. Yet it also needs to be sufficiently small: It is assumed that in the area around the peak, the major contribution to the probability is from the ground state, and that in areas farther away from the peak, the larger the share of excited states becomes. The excited states are induced by thermal excitation, but as their energy increases, their probability decreases.

The approach of the above paragraph builds upon an assumed similitarity of the one- and two-dimensional cases when considering the excited states during the QPU run. Two such one-dimensional excited states are depicted as an example in Fig. 6.2, and taken from [BP18] for $l = 3$; It is presumed that the states of the one-dimensional show a similar nodal structure to the two-dimensional system, resembling a cross-section through the space of the two-dimensional probability density. In Fig. 6.2, for the one-dimensional case, one can see that the major contribution in the vicinity of the local and global minimum stems from the ground state and that the excited states primarily add to the probabilities at the tails of the distribution. With the two peaks fitted, the tunneling fraction can be computed by taking the ratio between the summed probability of the probability distribution curve of the global minimum and the overall probability of the two curves, as the fits, despite having been performed on normalized data, might not be normalized themselves

$$\mathcal{T} = \frac{\int y_{\text{glob}}(\vec{\phi}) d\vec{\phi}}{\int [y_{\text{loc}}(\vec{\phi}) + y_{\text{glob}}(\vec{\phi})] d\vec{\phi}}. \tag{6.2}$$

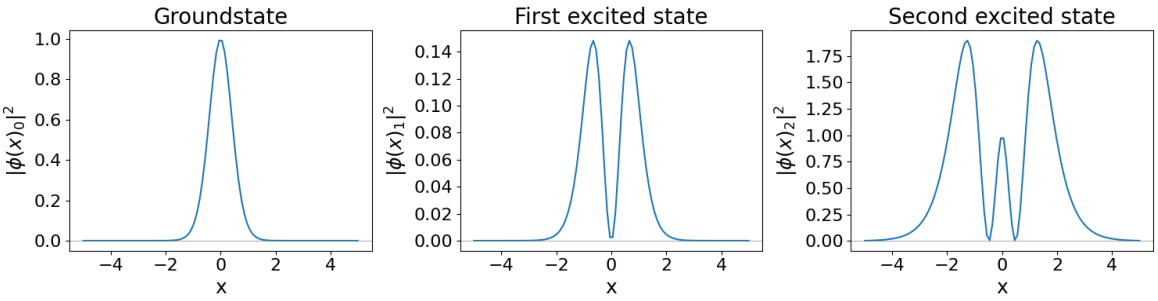

Figure 6.2.: Probability density distributions of the first three (bound) eigenstates for the potential $\frac{2m}{\hbar}V(x) = l(l+1)\tanh^2(x)$ with $l = 3$.

Remark 8 *The one-dimensional Hamiltonian of the potential* $\frac{2m}{\hbar}V(x) = l(l+1)\tanh^2(x)$ *can only have* $n = \lfloor l \rfloor$ *bound states [BP18, CGKN16] with* $n \in \mathbb{N}_0$. *As* $l = 1/2$ *and* $g = 3/4$ *are given here, theoretically, only the ground state is expected to manifest as a bound state (which is known from Eq. (2.41)) for each well, while the higher excited states manifest as scattering states. Nevertheless, they might influence the experimental data distribution in the same manner as the bound states through thermal effects, with the probabilities of the scattering states dissipating away from the peaks, flattening them and spreading them out.*

Additionally these states are examined for a singular potential well and it is not certain that the solution for a double well potential is always merely a linear combination of these states. For well-separated wells being far away from each other, this might hold, but the closer they are together, the greater the deviation from this simplifying assumption becomes.

6.2. False Vacuum Decay

To probe the false vacuum decay behavior on the QPU, the insights from the previous sections are combined here. For each run, the annealing schedule described in the previous section is implemented, together with the coupled domain wall encoding, encoding of the potential of Eq. (5.1) for $l = 1/2$ and $g = 3/4$, as well as the spin-reversal transformation of sec. 4.3, to mitigate the errors stemming from biases on the couplers as well as the h biases. For each annealing process, a total of $32 \times 32 = 1024$ qubits is used, while each annealing run is split into 6000 batches; 50 readouts are performed per batch.

The decay process is implemented for two scenarios. In the first scenario, the global minimum is shifted away from the local minimum in a diagonal manner; in the second scenario, the global minimum is shifted away in a spiral manner to probe the rotational symmetry on the QPU. In both cases, the local minimum is located at the origin at $(0, 0)$ and the distance between the two minima is increased in increments of $\Delta \approx 0.33$. The positions of the diagonally shifting global minimum $\vec{b}$ of the first scenario can be obtained from table 6.1.

Executing the annealing procedures for the diagonal shift of the positions of the global minimum yields, in total, seven final distributions from which the tunneling fractions are

$\vec{b}$	A	l	c_1	$\vec{\mu}_1$	B	g	c_2	$\vec{\mu}_2$
(1.41, 1.41)	0.25	0.64	1.78	(0.04, 0.05)	0.16	0.76	2.01	(1.25, 1.23)
(1.65, 1.65)	0.28	0.43	2.38	(0.02, 0.02)	0.10	0.79	1.92	(1.48, 1.48)
(1.89, 1.89)	0.30	0.34	2.90	(0.00, 0.01)	0.06	1.03	1.66	(1.71, 1.72)
(2.12, 2.12)	0.27	0.35	2.65	(0.00, 0.00)	0.04	2.90	0.90	(1.97, 1.97)
(2.36, 2.36)	0.33	0.46	2.33	(-0.01, -0.01)	0.02	92.61	0.16	(2.13, 2.17)
(2.59, 2.59)	0.33	0.27	3.40	(-0.02, -0.02)	0.01	3.26	0.83	(2.40, 2.37)
(2.83, 2.83)	0.33	0.33	2.92	(-0.01, -0.02)	0.01	948.43	0.04	(2.60, 2.58)

Table 6.1.: Table of double peak fitting parameters, according to Eq. (6.1), for the tunneling fraction simulation runs where the global minimum was shifted diagonally.

computed based on the fitting of a double peak, as described in the previous section. The first four out of the seven encoded potentials are depicted in Fig. 6.3. The final distributions are obtained by dividing the number of occurrences of a state by the product of total number of occurrences and discretization area. The distributions corresponding to the encoded potentials of Fig. 6.3 can be found in Fig. 6.4. The black outlines in the final distributions indicate the masks which have been used for the fitting procedure. It is noticeable that for small distances between local and global minimum, there is a greater decrease in the fraction $\mathcal{T}$ between the peaks, while for greater distances, the peak at the global minimum decreases in height while broadening. It is evident, that the peaks are not clearly separated and blend into each other as a superposition, as illustrated for the one-dimensional case in Fig. 6.1. Based on these distributions, the double peak function $\hat{y}$ is fitted and the fits for the distributions of Fig. 6.4 are displayed in Fig. 6.5. On the left, the observed final distribution is displayed in a two-dimensional plot, on the right, the double peak fit of the observed distribution is shown, and in the middle, the corresponding residuals $\Delta = \text{Data} - \text{Fit}$ are given. The associated fitting parameters of $\hat{y}$ can be found in table 6.1. From the figures, it is clearly visible that the fitted surfaces match the observed distributions from the QPU quite well, especially when comparing the magnitude of the residuals to the actual values at these positions.

However, it is also evident that, compared to the peaks in the fit, the observed peaks are broader and show a higher degree of overlap. This slight divergence can be explained by the nature of the fit, as it solely relies on the theoretical ground state of the modified Pöschl-Teller potential, while the excited states are not taken into account. But due to the fact that the QPU is also susceptible to thermal effects, higher excited states may become prevalent during the anneal, which leads to a deformation away from the expected ground state and to more spread out peaks, as described in the previous section.

This absence of higher excited states in the fit might also explain the fine structures in the residuals at the positions of the peaks, which seem to be of a systematic nature. Nevertheless, the residuals indicate that the peaks are captured quite well even though the aforementioned broadening can still be noticed as small systematic deviations from zero. The specific fitting parameters can be found in table 6.1.

Additionally, one can see in table 6.1 that the fitted l and g values do not correspond to the theoretical values of $1/2$ and $3/4$, which might again be explained by the absence of

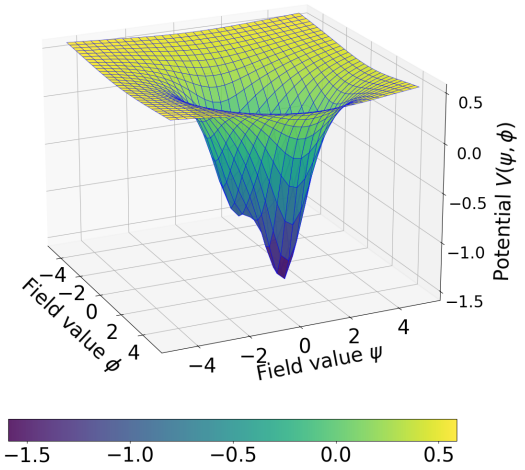

(a) $\vec{b} = (1.41, 1.41) \quad |\vec{b}| = 2$

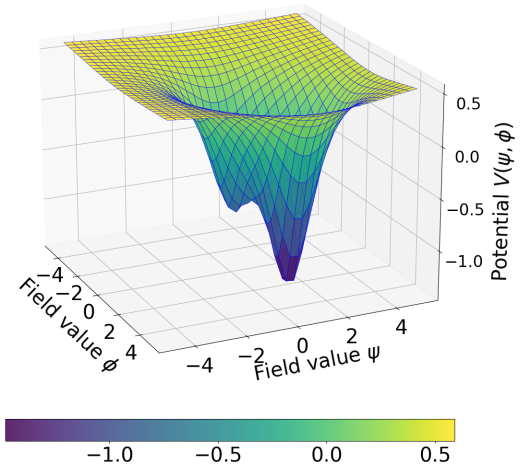

(b) $\vec{b} = (1.65, 1.65) \quad |\vec{b}| = 2.33$

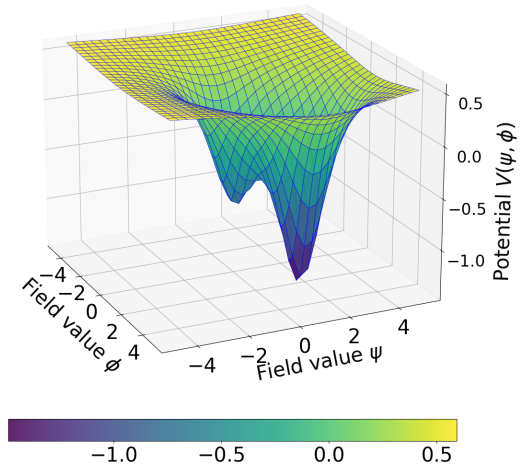

(c) $\vec{b} = (1.89, 1.89) \quad |\vec{b}| = 2.68$

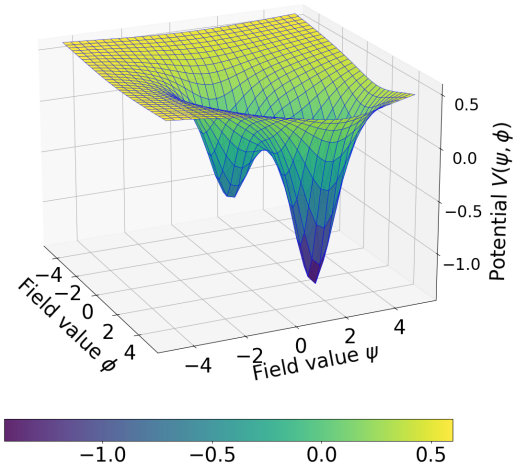

(d) $\vec{b} = (2.36, 2.36) \quad |\vec{b}| = 3.34$

Figure 6.3.: The encoded potentials Eq. (5.1) on the QPU using the coupled domain wall encoding, for $l = 1/2$, $g = 3/4$ and position $\vec{b}$ of the global minimum. $32 \times 32 = 1024$ qubits have been used for this.

thermal excited states in the fitting function but also, to a large extent, by the fact, that these parameters show, to some degree, a correlation with the c_i parameters, which also influence the peak width. This correlation is especially apparent in the fifth and seventh row, in which

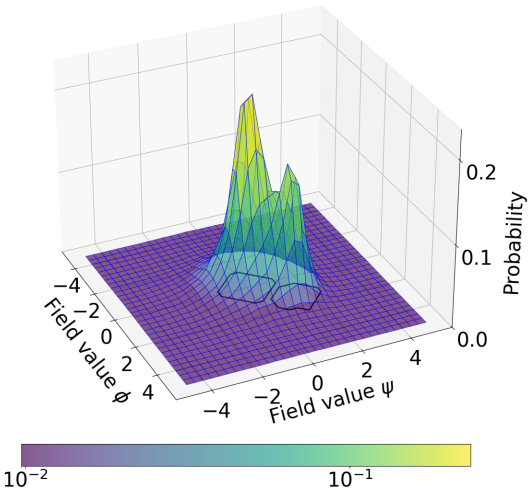

(a) $\vec{b} = (1.41, 1.41) \quad |\vec{b}| = 2$

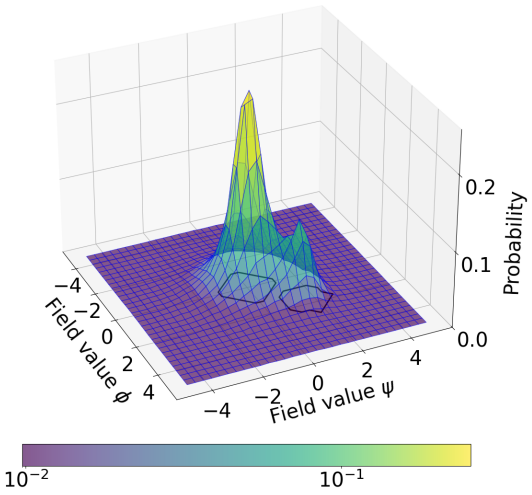

(b) $\vec{b} = (1.65, 1.65) \quad |\vec{b}| = 2.33$

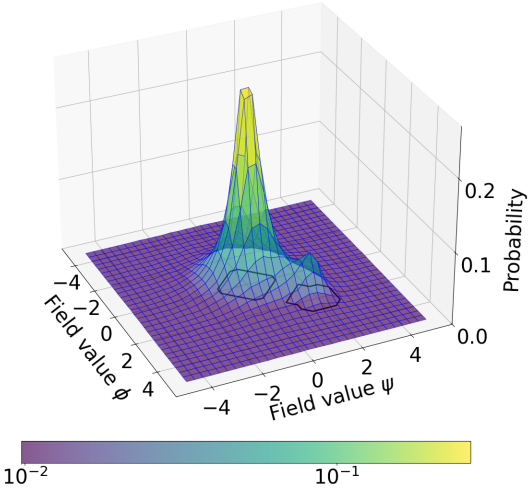

(c) $\vec{b} = (1.89, 1.89) \quad |\vec{b}| = 2.68$

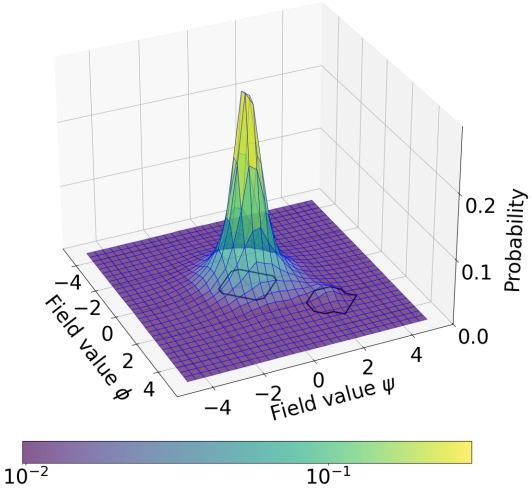

(d) $\vec{b} = (2.36, 2.36) \quad |\vec{b}| = 3.34$

Figure 6.4.: The final normalized probability densities over the space of possible field configurations for the encoded potentials of Fig. 6.3, measured on the QPU, at the end of an anneal. These can be interpreted as the probabilities to encounter the fictive particle at a given field configuration. The black outlines represent the masks which are used for the fitting procedure. The simulations are run with $32 \times 32 = 1024$ qubits, 6000 batches and 50 reads per batch.

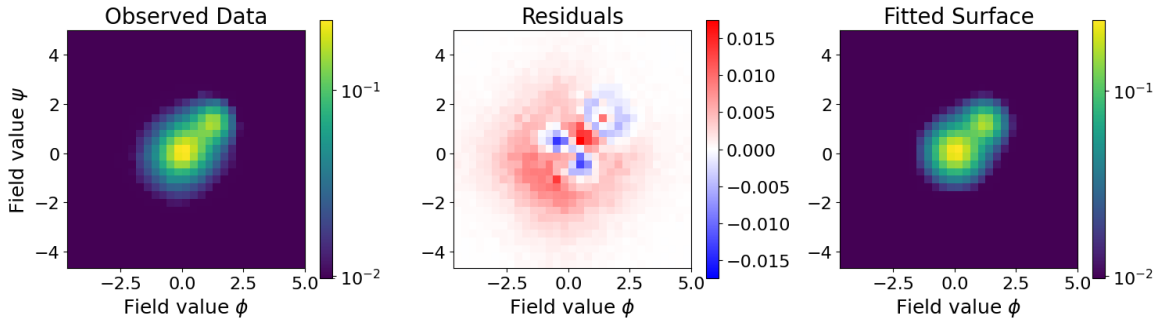

(a) $\vec{b} = (1.41, 1.41) \quad |\vec{b}| = 2$

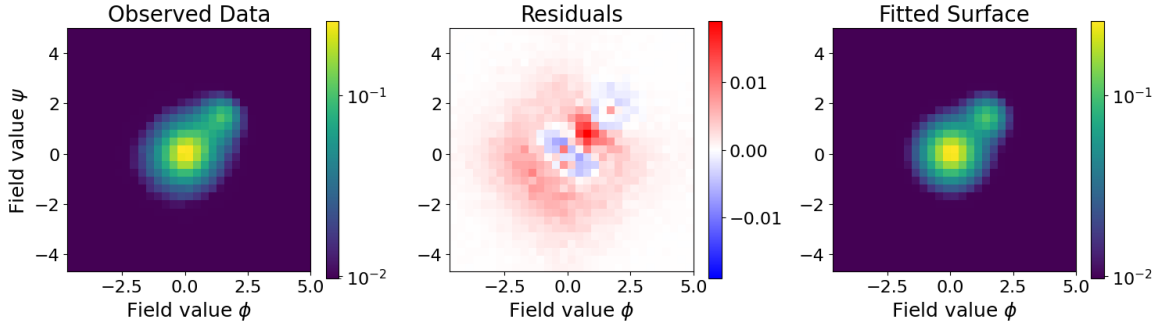

(b) $\vec{b} = (1.65, 1.65) \quad |\vec{b}| = 2.33$

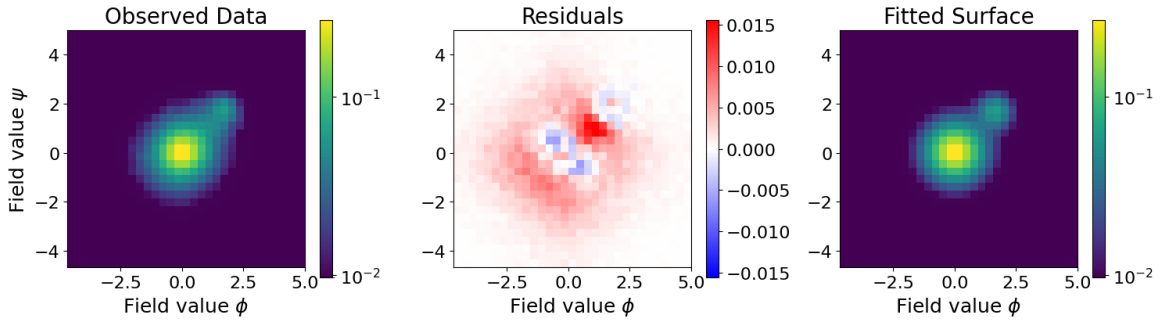

(c) $\vec{b} = (1.89, 1.89) \quad |\vec{b}| = 2.67$

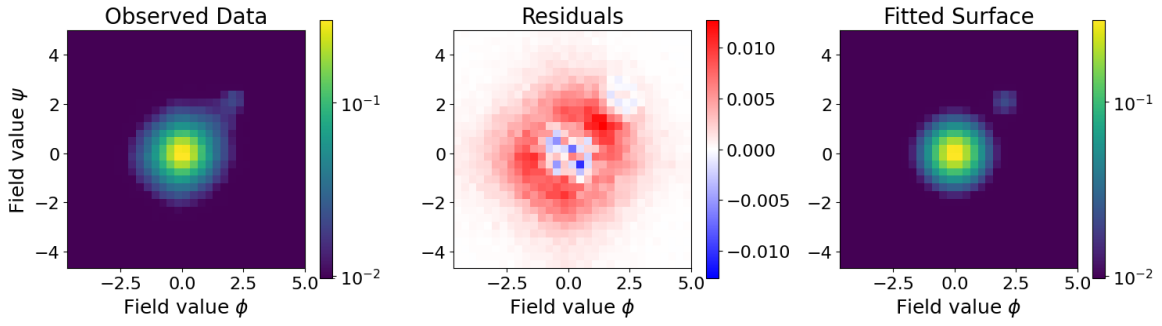

(d) $\vec{b} = (2.36, 2.36) \quad |\vec{b}| = 3.34$

Figure 6.5.: Normalized probability densities of Fig. 6.4 on the left, the respective fits according to the double-peak fitting function $\hat{y}$ on the right, and their residuals in the middle.

the g values are unusually large and the c_2 values unusually low. The probability distribution as well as the fit corresponding to the fifth row in table 6.1 can be found in Fig. (6.4d) and (6.5d), where, regardless of the aforementioned discrepancy, the fit matches the observed distribution quite well.

Because the peak width is not only controlled by l and g, but also by c_i, it is hardly possible to compare the l and g values with theoretical predictions, where c_i is constant. (Theoretically, the c_i values should all be one, but in order to obtain an adequate fit, it is beneficial to use the c_i values as fitting parameters.) When one tries to modify the fit for better comparability, one option is to bound the fitting parameters. One such example is to set $g \leq 4$, which has the effect that the c_2 value becomes larger, yet does not result in a significant difference from the unbound case. Nevertheless, because the tunneling fraction did not change noticeably and only the qualitative behavior of the decay is of interest, the parameters of the unbound case are used in this work. For future studies which may explore not only qualitative, but also quantitative behavior, the bound case is indeed preferable.

Another observation is that the fitted positions of the minima $\vec{\mu_2}$ do not coincide precisely with their theoretical positions. Though they are close, they deviate slightly and systematically toward the position of the local minimum. This deviation is likely an artifact of the fitting procedure as, as previously stated, only ground state functions were used for fitting, whereas the actual data originates from a mixed state distribution. As a result, the tail of the local minimum peak appears more elevated than predicted by the ground state function, which is evident in the residuals plot Fig. 6.5. The plot additionally shows an excess intensity between the peaks compared to the outer tails. To compensate for this discrepancy and minimize the residuals, during the fitting, the global minimum peak is shifted slightly toward the more inert local minimum peak due to its larger aggregated probability mass. Note, that for the encoding of a potential on the QPU, one needs to discretize the potential, thereby potentially shifting the original position of the minima. As a result, the peaks might show a slight offset along the line connecting the theoretical minima positions, which might explain the small offsets for μ_1.

Computing the tunneling fractions based on these fits according to Eq. (6.2) and plotting them against the distance between the fitted peaks according to $|\vec{\mu}_1 - \vec{\mu}_2|$, yields Fig. 6.6a. The predicted exponential decay behavior of the square of the absolute value of Eq. (2.16) is evident. Performing an exponential fit of the form

$$y_{\text{exp}}(C, \alpha, \beta) = Ce^{-\alpha|\vec{b}|} + \beta, \tag{6.3}$$

for the tunneling fractions, yields the red dashed line with the residuals given in the plot below.

While, theoretically, the parameter β should be zero, it was nevertheless incorporated into the fit, because during the annealing, the decay might not always reach zero due to a positive offset on the probabilities over all possible states. This effect becomes more apparent for lower s_{min} values, as s_{min} controls the kinetic term in the annealing Hamiltonian. The lower s_{min}, the greater the kinetic term and thus the space that the fictive particle can explore. If the kinetic energy of the particle passes the threshold at which the kinetic energy becomes greater than the maximum value of the potential, it becomes a free particle unbounded by

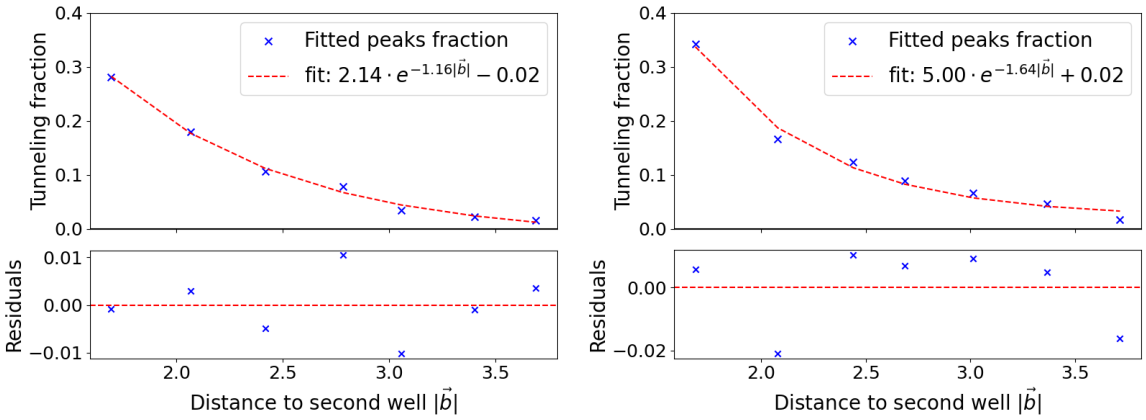

(a) Diagonal shifting of global minimum.

(b) Spiral shifting of global minimum.

Figure 6.6.: Tunneling fractions according to Eq. (6.2) for the fitted peaks are marked by blue crosses. The exponential fit of the fractions is given by the red dashed line with the according residuals plot in the graph below. The distances between the peaks has been computed based on the fitted peak positions $|\vec{\mu}_1 - \vec{\mu}_2|$.

the potential, having non-zero probabilities over the whole possible space. As a consequence, the decay may not converge to zero asymptotically.

It is important to note that the tunneling probability for some given time T, in this case $\approx 60\mu s$, is measured, instead of the decay probability per unit time. But due to their proportionality (Eq. (2.27)) and, in particular, their sharing the same decay exponent, one can also draw conclusions for the decay probability per unit time.

Comparing the fitted function with the numerical solutions of the decay exponent from section 5.2 is only possible for the α value of the fit, as the parameter C not only incorporates the constant offset of the decay exponent B, from the fit in Fig. 5.2, but, in theory, also the whole squared absolute of the prefactor from Eq. (2.16). Due to the complexity of the prefactor and the rather secondary influence on the qualitative behavior of the decay, this was not investigated further in this work, making it impossible to reliably estimate the constant in the exponent in that manner. As the current objective is to draw qualitative conclusions about the functional behavior, this is entirely sufficient.

Comparing the slope of the fit in Fig. 5.2 with the α parameter from Eq. (6.3) which was used as the fit in Fig. 6.6a, it becomes evident that they do not coincide exactly. Instead, they differ by a factor of approximately 1.7. Several reasons may contribute to this discrepancy:

Most importantly, the numerical results are based on the same theory from which Eq. (2.16) is derived. This theory assumes a one-way tunneling process without any tunneling-back. This is contingent upon the value of the evolution time T, which is itself depending on the potential using the Euler-Lagrange equations (2.31), being equal to half of an oscillation period (see remark 2). These equations depend on the value $\hbar^2/2m$, which is crucial to estimate the actual evolution time of the system on the QPU. However, obtaining this value is difficult. It can be estimated, for instance, by fitting the one-dimensional ground state

function of the harmonic oscillator [AS21], from which $\hbar^2/2m$ can be obtained. By obtaining $\hbar^2/2m$ from the fitting, it may not remain constant across different annealing parameters or system configurations, such as the $s_{\min}$ value. It is also doubtful whether this method truly returns $\hbar^2/2m$, or whether it merely reflects a thermal distribution over the harmonic potential. No conclusions can be drawn from the shape of the distribution, because, just like the ground state distribution of the quantum harmonic oscillator, the thermal distribution of the harmonic potential resembles a Gaussian distribution. Most likely, the result is a mixture of both quantum and thermal effects, which poses considerable difficulties for the fitting procedure.

Another issue arises from the way in which the potential of Eq. (5.1) was directly encoded in the annealing Hamiltonian. Here, the necessary prefactor $\hbar/2$ was set to one, though ideally it should have been replaced by the fitted value discussed in the previous paragraph. The prefactor could have been absorbed into the constant c of Eq. (2.43) and carried into Eq. (5.1); however, this was not implemented, since the precise estimation of the prefactor remains inaccessible. Without it, accurate quantitative results are difficult to obtain.

This prefactor $\hbar/2$ is also relevant for determining the correct $s_{\min}$ value for the anneal. Since $s_{\min}$ defines the particle's energy, which, within the theoretical model, is assumed to be equal to the local minimum energy (or the ground state energy if one avoids the classical regime approximation of section 2.1.1). Setting $s_{\min}$ correctly is thus essential for the annealing runs.

The fitting is critical because it determines the tunneling fraction per anneal run, and ultimately the decay behavior for a shifting global minimum. The present challenge is that the fitting is based on the assumption of a superposition of two ground state peaks. This may be a good approximation for well-separated wells, but its results become less reliable if wells are close together; in that case, the barrier height decreases, the potential wells deform, and the corresponding ground states change. Moreover, the fitting neglects higher excited states that could appear due to thermal excitations, which further weakens its accuracy. Since the decay fit relies heavily on the preceding peak fit, even small errors in estimating the tunneling fraction can significantly affect the slope of the exponential decay.

Lastly, a limitation arises from the theoretical assumptions about the potential. Even if the decay probability per unit time were derived using bounce solutions (section 2.1.2), this method would be based on an open potential, which is not the case here. The discretization used during potential encoding introduces infinite boundary conditions, always bounding the potential, regardless of its form. As a result, oscillations in the survival probability of the metastable state naturally emerge (see remark 1). An open potential can only be assumed, to some extent, if thermalization effects of the QPU are included, as discussed in remark 2.

To probe the system's rotational symmetry on the QPU, the above annealing runs were repeated while shifting the global minimum in a spiral manner away from the local minimum. The positions of the global minimum $\vec{b}$ can be found in the first column of table 6.2. The rest of the configurations and parameters were kept the same. As the results are quite similar to Fig. 6.4, as was to be expected, only two of the seven resulting potentials and their final distributions after the annealing process are presented in Fig. 6.7. Performing the peak-fitting procedure for all seven anneals results in the fitted parameters of table 6.2. Here, just as

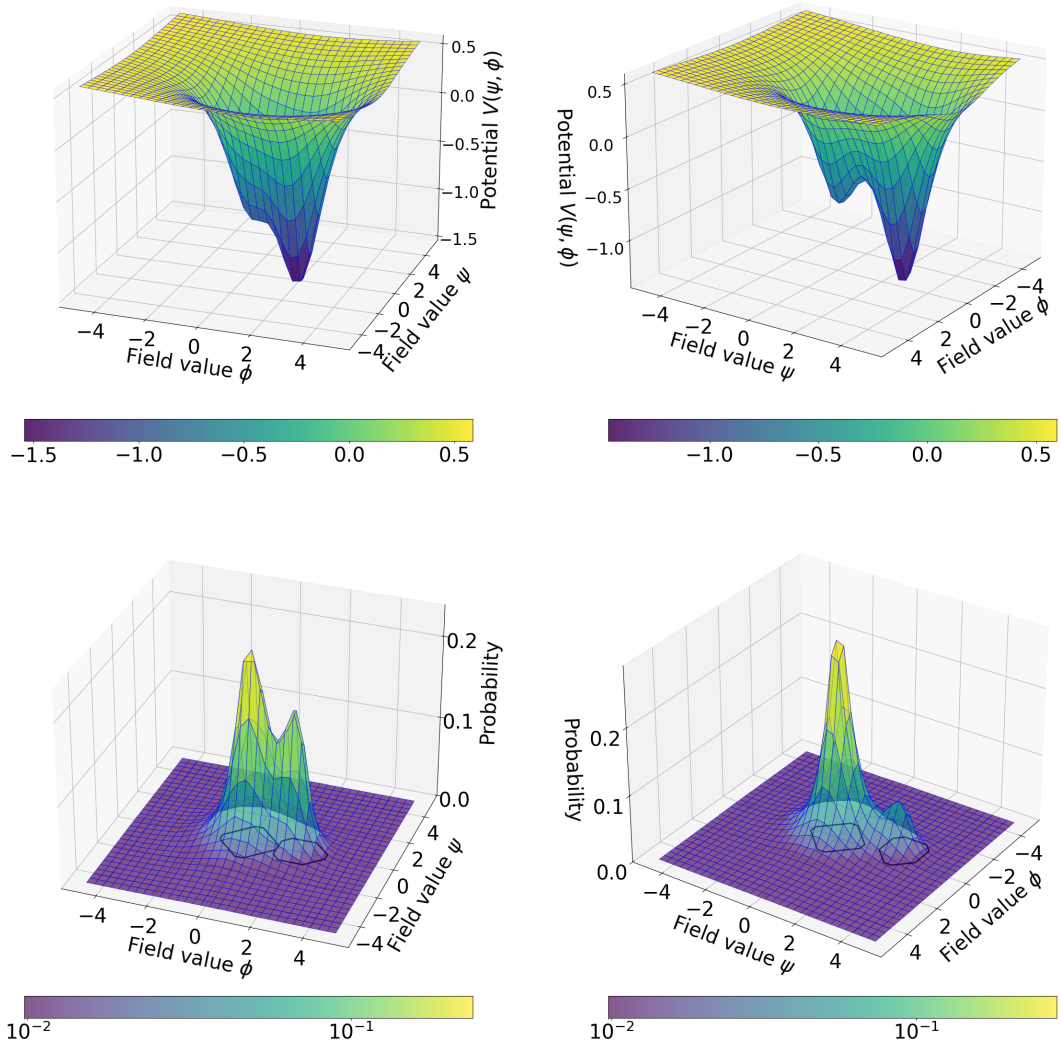

(a) $\vec{b} = (2, 0) \quad |\vec{b}| = 2$

(b) $\vec{b} = (-0.6, 2.6) \quad |\vec{b}| = 2.67$

Figure 6.7.: The upper row depicts the encoded potential Eq. (5.1) on the QPU, for $l = 1/2$, $g = 3/4$ and position $\vec{b}$ of the global minimum. The row below shows the normalized probability densities over the discretized space of possible field configurations measured on the QPU at the end of an anneal. These can be interpreted as the probabilities of encountering the fictive particle for a given field configuration. The black circles represent the masks which are used for the fitting procedure. $32 \times 32 = 1024$ qubits, with 6000 batches and 50 reads per batch are used for these simulations.

$\vec{b}$	A	l	c_1	$\vec{\mu}_1$	B	g	c_2	$\vec{\mu}_2$
(0.00, 2.00)	0.24	1.22	1.21	(0.08, -0.03)	0.18	0.64	2.21	(-0.02, 1.77)
(1.45, 1.82)	0.30	0.39	2.60	(0.01, 0.01)	0.10	0.63	2.32	(1.29, 1.65)
(-0.59, 2.60)	0.33	0.27	3.49	(-0.04, 0.02)	0.08	0.70	2.15	(-0.53, 2.41)
(-2.70, 1.30)	0.32	0.40	2.61	(-0.07, -0.02)	0.05	2.13	1.07	(-2.49, 1.15)
(-3.00, -1.45)	0.32	0.40	2.62	(-0.06, -0.04)	0.04	1615.86	0.04	(-2.80, -1.30)
(-0.82, -3.57)	0.33	0.38	2.67	(-0.04, -0.06)	0.03	2533.90	0.03	(-0.74, -3.35)
(2.49, -3.13)	0.34	0.35	2.84	(-0.02, -0.05)	0.01	1.43	1.48	(2.31, -2.95)

Table 6.2.: Table of double-peak fitting parameters, according to Eq. (6.1), for the tunneling fraction simulation runs in which the global minimum was shifted outward in a spiral manner around the local minimum .

in the preceding runs for the diagonal shifting of the global minimum, one can observe that l and g deviate from the theoretical values of 1/2 and 3/4. For some annealing runs, they show only slight discrepancies, but because they are not consistently close for all runs, their validity is questionable. As previously indicated, this might be explained by the correlation with the c_i values, as is evident from the fifth and sixth row of table 6.2, where the g values are unusually high and the c_2 values unusually low.

The systemic offset in the fitted peak positions $\vec{\mu}_1$ and $\vec{\mu}_2$ can be observed once again and can be attributed to the discretization of the potential for the QPU. The fitted double peaks of the distributions in Fig. 6.7 can be found in Fig. 6.8. Computing the tunneling fractions from these fits and plotting them again against the distance of the fitted peak positions yields Fig. 6.6b with the exponential fit represented by the red dashed line. The exponentially decaying behavior is also evident. While the slope is closer to the numerical solutions of section 5.2, it does not quite match it. This is likely for the same reasons that were discussed in connection with the decay with a shifting of the global minimum in a diagonal manner. Even though the decay curves resulting from the diagonal shifting are run on the same QPU with the exact same parameters set for the annealing runs, they differ from the ones with the spiral shifting. When comparing the absolute values of the tunneling fractions at each distance for the diagonal and spiral shifting procedures respectively, one can notice that they do not differ significantly and are rather close to one another for all distances. Notably, in Fig. 6.6b, the first value is slightly larger and the second value slightly lower than in the corresponding Fig. 6.6a. The rest of the values in Fig. 6.7 seems to be slightly higher. The derivative of an exponential function is, in turn, an exponential function, thus accounting for the changing rate of the initial function at the input; therefore, the exponential function is highly sensitive to its input and small differences from the QPU data in the tunneling fractions result in a larger negative slope for the exponential decay in Fig. 6.6b, causing it to converge faster.

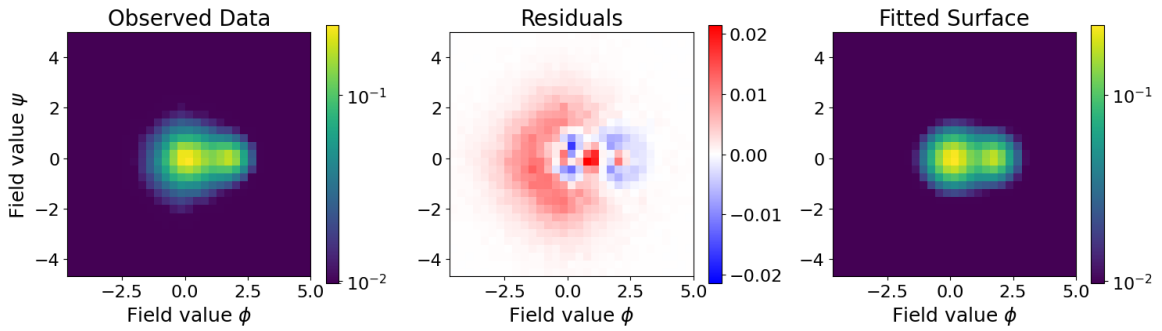

(a) $\vec{b} = (2, 0) \quad |\vec{b}| = 2$

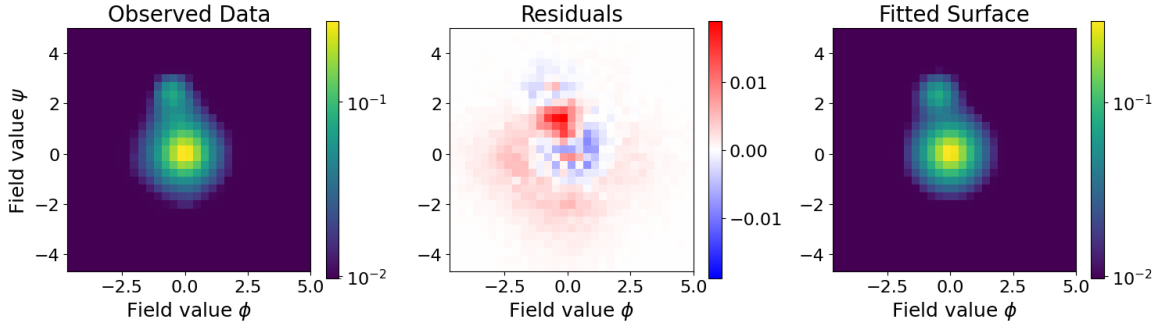

(b) $\vec{b} = (-0.6, 2.6) \quad |\vec{b}| = 2.67$

Figure 6.8.: Normalized probability densities of Fig. 6.7 on the left, the respective fits according to the double-peak fitting function $\hat{y}$ on the right, and their residuals in the middle.

6.3. Quantum or Thermal?

This raises the question, whether the observed behavior is of quantum or thermal nature. In [AS21], in which thermal and quantum predictions were compared with the observed behavior, it was already attempted to answer this question for the one-dimensional case. The expected behavior from a quantum perspective in the semi-classical regime, in combination with the Pöschl-Teller potential, is an exponential decay depending on the distance between the two minima (section 5.2). If using the thermodynamic approach instead, assuming mainly thermal effects in an equilibrium and expecting the thermal energy to be high enough to excite states over the barrier, one would anticipate a Boltzmann distribution, $p_i = e^{-E_i/(k_b T)}$ over all possible eigenstates as the final distribution, in which the eigenstate with the lowest eigenenergy would have the highest occupancy. In this scenario, the distance between the minima would not matter, as it does not influence the eigenenergies of the eigenstates of the separate wells, and therefore one would expect to see a constant tunneling fraction, independent of the distance.

When viewed in light of this, the results of section 6.2 indicate that the major contribution likely stems from quantum mechanical principles, because out of the two, it is the only model which also shows an exponential decay. Here, the emphasis is on *likely* as there are

several limitations: Firstly, one expects a constant tunneling fraction only in the case of a thermodynamic equilibrium, but when examining the final distributions of Fig. 6.4 and its corresponding potentials in Fig. 6.3, this expectation might not hold, as, apparently, the ground state of the global minimum, which has the lowest energy of all possible eigenstates in this potential, does not have the highest occupancy, but rather the ground state of the local minimum does. Accordingly, one needs to model this system using non-equilibrium thermodynamics to gain a better understanding of what it would behave like in this limit, which hasn't been done yet. When considering that for the results of section 6.2 an overall annealing time of $100\mu s$, which incorporated $60\mu s$ of tunneling time, was used, this notion appears to be reasonable. Although, according to [Ami15], annealing times of this order of magnitude lie well within the quasistatic regime, that conclusion was drawn for a specific problem instance; thus the regime boundaries may shift with larger qubit counts, and the present case may thereby fall into the non-equilibrium regime. All in all, the only conclusion that one can draw with certainty at the moment is, that the current system is not in a thermal equilibrium and therefore not in the quasistatic regime.

7. Discussion and outlook

In this work, the qualitative behavior of a false vacuum decay in two dimensions was investigated. For this purpose, the theoretical background was outlined and ways were presented on how to simulate such a decay on a quantum annealer to test the theoretical predictions. Different methods were analyzed on how to encode the problem on a quantum annealer and from all the methods presented, the coupled domain wall emerged as the most promising approach, as it uses the least amount of qubits while still preserving distance and rotational symmetry, both of which are crucial for the simulation of the physical model on the QPU. The simulations naturally raised the question of fidelty, that is to say, whether the system 'does what it should do'. Even though the coupled domain wall encoding without any encoded potential was used and a uniform distribution was to be expected, one obtained a distribution which clearly showed a bias toward anti-ferromagnetic states. To counter this problem, stemming from biases on the couplers between qubits, several approaches were investigated, such as shimming and a gauge transformation of the qubits. It was found that gauge transformations produced the most promising results, which not only averaged out the bias but also decreased its variance. Due to its simplicity and because there is no need for extra iterations to retrieve a correction term, it provides a lightweight but effective technique for error mitigation.

With this, one could study a false vacuum decay, in which two wells were given by the modified Pöschl-Teller potential with one local and one global minimum. As predicted in the semi-classical quantum field theoretic approach, a qualitative exponential decaying behavior depending on the distance between the minima was observed. Whether this behavior is truly of a quantum mechanical nature needs to be determined in future research by studying limit cases, with, for instance, infinitely narrow wells. Other theories such as non-equilibrium thermodynamics need to be explored on whether they produce results similar to the observed behavior or if they can be excluded as an explanation. In this work it could be shown that the system was not in a thermodynamic equilibrium. Nevertheless, a quantization of the decay was not pursued, as the higher excited states for the two-dimensional modified Pöschl-Teller potential and key parameters such as $\hbar^2/2m$ remain undetermined, and a detailed treatment would have exceeded the framework of this thesis. The parameter $\hbar^2/2m$ is also needed to compute the $s_{\min}$ value controlling the energy of the fictive particle as introduced in section 2.3. Additionally, one is limited by real-world constraints; approximations were needed to simulate the theory on the QPU such as the discretization of the problem, which introduced infinite boundary conditions, as opposed to the open potential of the theory [Col77], in which there is a single well with an energy level higher than that of the potential in the asymptotical limit.

It would be of great interest for future research to investigate if other theories and models might explain the exponentially decaying behavior equally well or better, to gain an improved

understanding of the processes occurring on the QPU. For that purpose, it might be of interest to perform Monte Carlo simulations to probe the non-equilibrium thermodynamic approach or possibly model it using diffusion equations. These insights would enable quantitative analysis of the problem that was investigated in this work. With the ability to change the temperature on the DWave QPU, it would be of further interest to examine the convergence behavior of the decay, which depends on the temperature. Lowering the temperature toward zero would allow for the potential isolation of thermal effects. Furthermore, with the advent of fast reverse annealing on the DWave QPU, it would be of interest to rerun the simulations performed herein in the coherent regime [Ami15] to further minimize thermal influences on the solutions.

One might also explore other types of QPUs which might be even more suitable to the problem at hand. Though one would certainly have to redesign the way of encoding the problem onto the alternatively chosen machine, but the underlying theoretical model should not change. As the given method in this work can be easily adjusted to encode higher-dimensional potentials, it might also be of interest to extend the presently investigated two-dimensional models to three- or higher-dimensional models. A notable application for the framework used to simulate the false vacuum decay, might be to investigate the two-dimensional potential of graphene and, from simulations, to determine the hopping terms of the electrons between the atoms quantitatively. Other possible applications include measuring tunneling probabilities of arbitrary potentials, as well as the computation of probabilities of electrons transitioning between different energy levels within an atom, which represent local minima. All in all, the considerations laid out in this thesis have shown how the simulation of false vacuum decay on quantum computers opens a path into a fascinating field that continues to challenge our understanding while offering remarkable opportunities for scientific discoveries.

A. Appendix

A.1. Mathematical techniques

For the thorough derivation of the false vacuum decay in the semi-classical regime of the path integral formalism, it is necessary to use advanced mathematical techniques which are going to be presented in the following subsections.

A.1.1. Wick-Rotation

A *Wick-Rotation* is a rotation of 90° in the complex plane. This is usually done in physics by changing from real to complex time, which is done by setting $t \to i\tau$. This leads to a change from the *Minkowski Space* to the *Euclidean space*, which can be seen by analyzing the according metrics with respect to the $(\partial_\mu \phi)^2$ operator in Eq. (2.2). The metrics are given by

$$g_{\mu\nu}^{\text{Minkowski}} = \text{diag}(-1, 1, 1, 1), \qquad g_{\mu\nu}^{\text{Euclidean}} = \text{diag}(1, 1, 1, 1). \tag{A.1}$$

The operator in Minkowski space therefore yields

$$(\partial_\mu \phi)^2 = g_{\mu\nu}^{\text{Minkowski}} \partial_\mu \phi \partial_\nu \phi = -\left(\frac{\partial \phi}{\partial t}\right)^2 + \left(\frac{\partial \phi}{\partial x}\right)^2 + \left(\frac{\partial \phi}{\partial y}\right)^2 + \left(\frac{\partial \phi}{\partial z}\right)^2 \tag{A.2}$$

whereas in the Euclidean space this would have yielded

$$(\partial_\mu \phi)^2 = g_{\mu\nu}^{\text{Euclidean}} \partial_\mu \phi \partial_\nu \phi = \left(\frac{\partial \phi}{\partial t}\right)^2 + \left(\frac{\partial \phi}{\partial x}\right)^2 + \left(\frac{\partial \phi}{\partial y}\right)^2 + \left(\frac{\partial \phi}{\partial z}\right)^2. \tag{A.3}$$

It is evident at once that if one uses complex time, the metrics transform into one another, due to $-(\partial\phi/\partial t)^2 \overset{t=it}{\to} -(\partial\phi/i\partial t)^2 = (\partial\phi/\partial t)^2$.

A.1.2. Saddle-Point approximation

Consider the integral

$$F(x) = \int_\gamma g(z) e^{\lambda f(z)} dz, \tag{A.4}$$

where γ is a contour in the complex plane and $g(z)$ a smooth function. Such integrals are not trivial to solve and often require advanced techniques. The *saddlepoint approximation* represents such a technique.

Assuming $\gamma \to \infty$, similar to the condition of the *Laplace Method*, in which for a function $h(x) = \exp(-Mf(x))$ with $f(x_0)$ being the minimum and $M \to \infty$, one can observe that the ratio

$$\frac{h(x)}{h(x_0)} = e^{-M(f(x)-f(x_0))} \tag{A.5}$$

is an exponential decay, which approaches zero for values far away from the minimum $f(x_0)$, thus showing that, in this case, the minimum is the only dominating value if one were to integrate the function.

Here, a similar case presents itself, as the dominating values of the integral are the stationary points of the function $f(z)$ in Eq. (A.4); or, to be more precise, the largest saddle point, as saddle points are the only stationary points in the complex plane. This can be deduced from the *Cauchy-Riemann equations*, which are, given a function $\zeta(z) = \zeta(x+iy) = u(x,y) + iv(x,y)$, with $z = x + iy$ being a complex input and u, v being real characterizing the real and imaginary part of the function,

$$\frac{\partial u}{\partial x} = \frac{\partial v}{\partial y}; \qquad \frac{\partial u}{\partial y} = -\frac{\partial v}{\partial x}. \tag{A.6}$$

Using these equations, one obtains the *Laplace equation* for u

$$\frac{\partial^2 u}{\partial x^2} = -\frac{\partial^2 u}{\partial y^2} \tag{A.7}$$

and, by proceeding analogously, also for v. These are the conditions for saddle points; for at a saddle point a function attains a minimum in one direction and a maximum in another (i.e. complementary in x- and y-direction). These conditions hold for any given complex differentiable (*holomorphic*) function $\zeta(z)$. The derivative in x and y for such a function is given by the *Wirtinger derivative*

$$\frac{\partial}{\partial z} = \frac{1}{2}\left(\frac{\partial}{\partial x} - i\frac{\partial}{\partial y}\right). \tag{A.8}$$

Therefore, every stationary point in $\partial\zeta(z)/\partial z = 0$ is also a stationary point in $u(x,y)$ and $v(x,y)$, and, given Eq. (A.7), a saddle point.

The approach is to deform the contour γ in Eq. (A.4), which is valid due to *Cauchy's integral theorem*, in such a manner that one passes the saddle point so that the imaginary part $\Im[f(z)] = \text{const}$ and the real part $\Re[f(z)]$ are traversed in the steepest possible descent, to achieve an effect similar to the Laplace method. The path of steepest descent for $u(x,y)$ is equivalent to following the path of constant $v(x,y)$. This can be seen by analyzing the steepest descent of u, which is given by

$$\vec{n} = \vec{\nabla} u(x,y) = \begin{pmatrix} \frac{\partial u}{\partial x} & \frac{\partial u}{\partial y} \end{pmatrix}. \tag{A.9}$$

Inserting this into the path of v with $\epsilon \to 0$ yields

$$v(x + n_x\epsilon, y + n_y\epsilon) = v(x,y) + \left[\frac{\partial v}{\partial x}n_x + \frac{\partial v}{\partial y}n_y\right]\epsilon, \tag{A.10}$$

with n_x and n_y being the vector components of Eq. (A.9). Evaluating the bracket and with the help of the Cauchy-Riemann equations, one obtains

$$\frac{\partial v}{\partial x}n_x + \frac{\partial v}{\partial y}n_y = \frac{\partial v}{\partial x}\frac{\partial u}{\partial x} + \frac{\partial v}{\partial y}\frac{\partial u}{\partial y} \tag{A.11}$$

$$= \frac{\partial v}{\partial x}\frac{\partial v}{\partial y} - \frac{\partial v}{\partial y}\frac{\partial v}{\partial x} \tag{A.12}$$

$$= 0, \tag{A.13}$$

showing that $v(x, y)$ stays constant.

Hence, the first step is to determine the saddle points of $f(z)$. These are given by

$$\left.\frac{\partial f}{\partial z}\right|_{z=z_0} = 0. \tag{A.14}$$

If there are several saddle points, one needs to choose the one with the largest real value. The contour is deformed to $\gamma \to \gamma'$ so that it passes this saddle point. The next step is to approximate the exponent at this saddle point; to this end a *second-order Taylor expansion* is used

$$f(z) \approx f(z_0) + \frac{1}{2}f''(z)(z - z_0)^2 + O(z^3), \tag{A.15}$$

which in turn is inserted into Eq. A.4

$$F(x) \approx g(z_0)e^{\lambda f(z_0)} \int_{\gamma'} e^{\frac{\lambda}{2}f''(z)(z-z_0)^2} dz. \tag{A.16}$$

The exponent in the integral can be rewritten in terms of

$$z - z_0 = re^{i\phi} \qquad f''(z_0) = |f''(z_0)|e^{i\psi}, \tag{A.17}$$

with ϕ being the angle the contour passes through the saddle point, r the radius and ψ some angle, thus yielding the following equation

$$F(x) \approx g(z_0)e^{\lambda f(z_0)}e^{i\psi} \int_{\gamma'} e^{\frac{\lambda}{2}|f''(z_0)|e^{i(2\phi+\psi)}r^2} dr. \tag{A.18}$$

It is evident that the steepest descent is the one, where $e^{i(2\phi+\psi)} = -1$, which indicates that $2\phi + \psi = \pi$, thus providing the angle for the steepest descent through the saddle point $\phi = \frac{\pi-\psi}{2}$. The integral then results in

$$F(x) \approx g(z_0)e^{\lambda f(z_0)}e^{i\psi}\sqrt{\frac{2\pi}{\lambda|f''(z_0)|}}, \tag{A.19}$$

where a Gaussian integral was performed.

A.1.3. Functional Taylor-Expansion

When working with *functionals* (i.e. functions which map functions to functions) it is crucial to proceed cautiously, as one cannot simply apply the regular approximation methods from regular analysis; instead, one needs to modify the techniques. This is also the case for the *Taylor-Expansion*. The difference results mostly from the way derivatives are performed for functionals [GR96] ([GF65])

$$\mathrm{D}_{[\delta x(t)]}F[x(t)] = \int \frac{\partial F[x(t)]}{\partial x(t)}\delta x(t)dt, \tag{A.20}$$

which influences the whole expansion. The classical multivariate Taylor Expansion (TE)

$$F(\boldsymbol{x}) = F(\boldsymbol{a}) + \sum_{d=1}\frac{1}{d!}\sum_{n_1,\cdots,n_d=1}\frac{\partial^d F(\boldsymbol{x})}{\partial x_{n_1}\cdots\partial x_{n_d}}\bigg|_{\boldsymbol{x}=\boldsymbol{a}}(x_{n_1}-a_{n_1})\cdots(x_{n_d}-a_{n_d}), \tag{A.21}$$

where $\boldsymbol{x} = (x_{s_1},\cdots,x_{s_N})$ and similarly $\boldsymbol{a}$, can be used to derive the FTE in the form of a *Volterra series* around a path $x_a(t)$. To do this, a Frechet-differentiable functional $F[x(t)]$ is taken and in the first steps approximated by a multivariate function $F(x_{s_1},\cdots,x_{s_d}):\mathbb{R}^N\to\mathbb{R}$, where N equidistant samples of the function are taken over the path $x(t)$, denoted by $x_{s_d} = x(s_d)$, instead of directly using the path function and considering the limit $N\to\infty$. This can then in turn be represented by Eq. (A.21). One can map the classical derivatives to functional derivatives by making a suitable choice for the directional function resulting in

$$\frac{\partial F(\boldsymbol{x})}{\partial x_{s_d}}\bigg|_{\boldsymbol{x}=\boldsymbol{a}} = \mathrm{D}_{\mathbb{1}_{[s_d,s_{d+1})}}F[x(t)]\bigg|_{x(t)=x_a(t)} = \int_{s_d}^{s_{d+1}}\frac{\partial F[x(t)]}{\partial x(t)}\bigg|_{x(t)=x_a(t)}dt, \tag{A.22}$$

where $\mathbb{1}_{[s_d,s_{d+1})}$ is an indicator function restricting the integral on the interval of constant x_{s_d}. One can verify this intuitively by comparing the total differential of the multivariate function

$$dF = \sum_i \frac{\partial F}{\partial x_{s_i}}dx_{s_i} \tag{A.23}$$

and Eq. (A.20) in the continuous limit

$$\mathrm{D}_{[\delta x(t)]}F[x(t)] = \lim_{\Delta t\to 0}\sum_{i=0}\frac{\partial F[x(t)]}{\partial x(t)}\bigg|_{x(t)=x_{s_i}}dx_{s_i}\Delta t, \tag{A.24}$$

which need to be equivalent for $N\to\infty$. Therefore one can match

$$\frac{\partial F[x(t)]}{\partial x(t)}\bigg|_{x(t)=x_{s_i}} = \lim_{\Delta t\to 0}\frac{\partial F}{\Delta t\partial x_{s_i}}, \tag{A.25}$$

which can then be used in Eq. (A.22), with the help of the *Riemann-sum*, to establish the equivalency in the continuous limit of N. With this one can insert Eq.(A.22) into Eq. (A.21) which, in turn, in the continuous limit $N\to\infty$, gives the functional Taylor expansion

$$F[x] = F[x_a(t)] + \sum_{d=1}\frac{1}{d!}\int\cdots\int\frac{\partial F[x]}{\partial x(t_0)\cdots\partial x(t_d)}\bigg|_{x=x_a(t)}\delta x(t_0)\cdots\delta x(t_d)dt_0\cdots dt_d, \tag{A.26}$$

at the path $x_a(t)$ with $\delta x_i(t) = x_i(t) - x_a(t)$. For more details, see the derivation in [DTD23], while [Ern94] gives a practical application of it.

A.1.3.1. Second-order functional Taylor expansion around a minimum

The second-order FTE around a minimum is characterized by the fact, that the first-order is zero at the minimum, effectively letting only the second-order contribute to the approximation. Taking a closer look at the action Eq. (2.2) from section 2.1.1, one can see that for a first-order FTE, the integral is evaluated along the path which minimizes, in this specific case, the action. For reasons of simplicity this procedure will be done only for the **time dimension**, but can be easily modified to higher dimensions (see sec. A.1.3.2). For first-order FTEs, the minimum of the action is given by the path

$$\frac{\partial S[\phi]}{\partial \phi(\tau)} = \int_{\tau_a}^{\tau_b} d\tau' \left(\frac{d\phi}{d\tau'} \frac{d}{d\tau'} \delta(\tau - \tau') + V'(\phi)\delta(\tau - \tau') \right) \tag{A.27}$$

$$= \left[\dot{\phi}(\tau')\delta(\tau - \tau') \right]_{\tau_a}^{\tau_b} - \ddot{\phi}(\tau) + V'(\phi(\tau)) \tag{A.28}$$

$$\stackrel{!}{=} 0, \tag{A.29}$$

where from the first to the second line, a partial integration on the first term was performed and the relation

$$\frac{\partial \phi(t)}{\partial \phi(t')} = \delta(t - t') \tag{A.30}$$

for functionals was used. This result can also be deduced from the *Euler-Lagrange equations* of classical mechanics, which provides the classical paths, $\phi_{cl}(\tau)$, minimizing the action. In common physical cases it is necessary that $\delta\phi$ vanishes at the borders, as usually, paths are only considered at fixed points a to b, resulting in the cancellation of the first term in Eq. (A.28) when inserting in into Eq. (A.20). The second-order is given by

$$\frac{\partial^2 S[\phi]}{\partial \phi(\tau) \partial \phi(\tau')} = \left[-\frac{\partial^2}{\partial t^2} + V''(\phi) \right] \delta(\tau - \tau') = S''[\phi]\delta(\tau - \tau'). \tag{A.31}$$

Inserting all of this into the second-order FTE one obtains

$$S[\phi] \approx S[\phi_{cl}] + \frac{1}{2} \int \int S''[\phi_{cl}]\delta(\tau - \tau')\delta\phi(\tau)\delta\phi(\tau')d\tau d\tau' \tag{A.32}$$

$$= S[\phi_{cl}] + \frac{1}{2} \int S''[\phi_{cl}]\delta\phi(\tau)\delta\phi(\tau)d\tau, \tag{A.33}$$

where $\delta\phi(\tau) = \phi(\tau) - \phi_{cl}(\tau)$ and the first-order is cancelled out as the expansion is done around the classical path.

A.1.3.2. Functional Taylor expansion for multivariate input-functions

When working with higher-dimensional input functions like the four-dimensional QFT, one needs to adjust the way of applying directional derivatives. Fortunately, this is only a matter of notation. Given the function $F[\rho(\boldsymbol{r})]$

$$F[\rho(\boldsymbol{r})] = \int f(\rho(\boldsymbol{r}, \rho(\boldsymbol{r}), \nabla\rho(\boldsymbol{r}))d\boldsymbol{r}, \tag{A.34}$$

where the bold symbols represent the vector notation $\boldsymbol{r} = (r_0, \cdots, r_N)$ with N being the number of independent variables, the derivative in the direction of $\delta\rho(\boldsymbol{r})$ is given by

$$\mathrm{D}_{[\delta\rho(\boldsymbol{r})]}F[\rho(\boldsymbol{r})] = \int \frac{\partial F[\rho(\boldsymbol{r}))]}{\partial\rho(\boldsymbol{r})}\delta\rho(\boldsymbol{r})d\boldsymbol{r} \tag{A.35}$$

$$= \int \left(\frac{\partial f[\rho(\boldsymbol{r})]}{\partial\rho(\boldsymbol{r})} - \nabla\frac{\partial f[\rho(\boldsymbol{r})]}{\partial\nabla\rho(\boldsymbol{r})}\right)\delta\rho(\boldsymbol{r})d\boldsymbol{r} + C, \tag{A.36}$$

where $\partial/\partial\nabla\rho(\boldsymbol{r})$ is the derivative with respect to a vector and C is a constant depending on the boundary conditions (for more details, see chapter 7 in [GF65]). Also, as stated in the aforementioned case, it is usually required in a physical context that $\delta\rho(\boldsymbol{r})$ cancels at the boundaries, thus, in turn, leading to the cancellation of the constant C. This yields the multidimensional Euler-Lagrange equations. By inserting these into the Taylor expansion one obtains

$$F[\rho(\boldsymbol{r})] = F[\rho_a(\boldsymbol{r})] + \sum_{d=1}\frac{1}{d!}\int\cdots\int \left.\frac{\partial F[\rho(\boldsymbol{r})]}{\partial\rho(\boldsymbol{r}_0)\cdots\partial\rho(\boldsymbol{r}_d)}\right|_{\rho(\boldsymbol{r})=\rho_a(\boldsymbol{r})} \delta\rho(\boldsymbol{r}_0)\cdots\delta\rho(\boldsymbol{r}_d)d\boldsymbol{r}_0\cdots d\boldsymbol{r}_d. \tag{A.37}$$

A.2. Derivations

This subsection develops the derivations which the main work builds upon.

A.2.1. Action for a one-dimensional multi-field bounce

Given the Euclidean action for a multi-field system

$$S = \int_{-C/2}^{C/2} dx \left[\frac{1}{2}\left(\frac{\partial\boldsymbol{\phi}}{\partial x}\right)^2 + V(\boldsymbol{\phi})\right] = \int_{-C/2}^{C/2} dx \left[\frac{1}{2}\left(\frac{\partial\boldsymbol{\phi}}{\partial x}\right)^2 + V(\boldsymbol{\phi}) - E_c\right] + E_c C, \tag{A.38}$$

which follows the energy conservation of Eq. (2.5) and with the integration constant which equals the solution $S[\phi_{cl,0}]$ of the constant path from Eq. (2.16), one can rewrite the equation by applying *Young's inequality* which states

$$ab = \min_{\lambda>0}\left[\frac{\lambda^p a^p}{p} + \frac{\lambda^{-q}b^q}{q}\right], \tag{A.39}$$

for $a, b > 0$. With this inequality, one can write the integrand as

$$\sqrt{V\cdot K} = \min_{\lambda>0}\left[\frac{\lambda^2}{2}K + \frac{V}{2\lambda^2}\right] = \min_{\eta>0}\left[\frac{\eta}{2}K + \frac{V}{2\eta}\right], \tag{A.40}$$

in which K is the kinetic and V the potential term of the integrand, which should always be ≥ 0 as long as energy is conserved, with the reparameterization $\lambda^2 = \eta$ being used. Determining the minimum by computing the derivation and setting it to zero yields

$$\eta = \sqrt{\frac{V}{K}} = 1 \quad \Rightarrow \quad 2\sqrt{V\cdot K} = K + V, \tag{A.41}$$

where, on the left side, the energy conservation was applied. Substituting all this back into Eq. (A.38), one arrives at

$$S = \int dx 2\sqrt{\frac{1}{2}\left(\frac{\partial \boldsymbol{\phi}}{\partial x}\right)^2 \cdot [V(\boldsymbol{\phi}) - E_c]} = \int dx \sqrt{\left(\frac{\partial \boldsymbol{\phi}}{\partial x}\right)^2} \sqrt{2[V(\boldsymbol{\phi}) - E_c]}, \tag{A.42}$$

where the integration constant was neglected as it is not crucial for proceeding with the current derivation. Defining the arc length, which returns the length of the path that has already been traversed from x_0 to x as follows with its respective differential

$$s(x) = \int_{x_0}^{x} \sqrt{\left(\frac{\partial \boldsymbol{\phi}}{\partial x}\right)^2} dx \qquad ds = \sqrt{\left(\frac{\partial \boldsymbol{\phi}}{\partial x}\right)^2} dx, \tag{A.43}$$

allows for the reparameterization of the action, given that an inversion $x(s)$ exists, which should be the case for $|\partial \boldsymbol{\phi}/\partial x| \neq 0$, in the following manner

$$S = \int_0^{s_f} ds \sqrt{2[V(\boldsymbol{\phi}(s)) - E]}. \tag{A.44}$$

This yields the action in the line integral formulation, where one can see that $|\partial \boldsymbol{\phi}/\partial s| = 1$ as the arc length definition was used to parametrize the path having the property

$$\frac{\partial \boldsymbol{\phi}}{\partial s} = \boldsymbol{\phi}' \frac{dx}{ds} = \boldsymbol{\phi}' \left(\frac{ds}{dx}\right)^{-1} = \frac{\boldsymbol{\phi}'}{|\boldsymbol{\phi}'|} \quad \Rightarrow \quad \left|\frac{\partial \boldsymbol{\phi}}{\partial s}\right| = 1. \tag{A.45}$$

Remark 9 *The derivation above only holds as long as $a, b > 0$, which is not always the case for the potential or kinetic energy, as they can become zero, which makes the derivation only valid within the limit.*

A.2.2. Pöschl-Teller in 2D

Below are the first and second derivation of the family of ground states from Eq. (2.41) given with the norm constant excluded for simplicity

$$\nabla \varphi_l(|\vec{x}|) = -l \tanh(c \cdot |\vec{x}|) \operatorname{sech}^l(c \cdot |\vec{x}|) \frac{c \cdot \vec{x}}{|\vec{x}|} \tag{A.46}$$

$$\Delta \varphi_l(|\vec{x}|) = -c^2 l \operatorname{sech}^2(c \cdot |\vec{x}|) \operatorname{sech}^l(c \cdot |\vec{x}|) \frac{\vec{x}}{|\vec{x}|} \frac{\vec{x}}{|\vec{x}|} \tag{A.47}$$

$$- c^2 l \tanh(c \cdot |\vec{x}|) \left(-l \tanh(c \cdot |\vec{x}|) \operatorname{sech}^l(c \cdot |\vec{x}|) \frac{\vec{x}}{|\vec{x}|}\right) \frac{\vec{x}}{|\vec{x}|} \tag{A.48}$$

$$- c^2 l \tanh(c \cdot |\vec{x}|) \operatorname{sech}^l(c \cdot |\vec{x}|) \left(\frac{2}{|\vec{x}|} - \frac{\vec{x}^2}{|\vec{x}|^3}\right) \tag{A.49}$$

$$= c^2 \left[l^2 \tanh^2(c \cdot |\vec{x}|) - l \operatorname{sech}^2(c \cdot |\vec{x}|) - l \frac{\tanh(c \cdot |\vec{x}|)}{|\vec{x}|}\right] \operatorname{sech}^l(c \cdot |\vec{x}|) \tag{A.50}$$

$$= c^2 \left[-l + l(l+1) \tanh^2(c \cdot |\vec{x}|) - l \frac{\tanh(c \cdot |\vec{x}|)}{|\vec{x}|}\right] \operatorname{sech}^l(c \cdot |\vec{x}|), \tag{A.51}$$

where in the last step $\mathrm{sech}^2(x) = 1 - \tanh^2(x)$ was used. Inserting them into Eq. (2.40) yields Eq. (2.42).

A.2.3. Domain wall encoding into the J parameter

Starting with

$$V(\phi(\tau)) = \frac{1}{2}\sum_{i=1}^{N-1} V(\phi_0 + i\xi)(\sigma_{i+1}^z - \sigma_i^z), \tag{A.52}$$

it is noticeable that $(\sigma_{i+1}^z - \sigma_i^z)/2$ is an element of the set $\{0, 1\}$ which is why the equality $(\sigma_{i+1}^z - \sigma_i^z)/2 = [(\sigma_{i+1}^z - \sigma_i^z)/2]^2$ holds. Inserting this into the above formula one obtains

$$V(\phi(\tau)) = \frac{1}{4}\sum_{i=1}^{N-1} V(\phi_0 + i\xi)(\sigma_{i+1}^z - \sigma_i^z)^2 \tag{A.53}$$

$$= \frac{1}{4}\sum_{i=1}^{N-1} V(\phi_0 + i\xi)(\sigma_{i+1}^z\sigma_{i+1}^z - \sigma_i^z\sigma_{i+1}^z - \sigma_{i+1}^z\sigma_i^z + \sigma_i^z\sigma_i^z) \tag{A.54}$$

$$= \frac{1}{2}\sum_{i=1}^{N-1} V(\phi_0 + i\xi)(\sigma_{i+1}^z\sigma_{i+1}^z - \sigma_i^z\sigma_{i+1}^z), \tag{A.55}$$

where the relations $\sigma_{i+1}^z\sigma_{i+1}^z = \sigma_i^z\sigma_i^z = 1$ and $\sigma_{i+1}^z\sigma_i^z = \sigma_i^z\sigma_{i+1}^z$ were used. Extracting the J parameters and by comparison with the quantum annealing Hamiltonian, one obtains

$$J_{i,j} = \frac{1}{2}V(\phi_0 + i\xi)(\delta_{i,j} - \delta_{i,j-1}). \tag{A.56}$$

A.2.4. One-Hot encoding Hamiltonian transformation

To obtain the J-couplings and h-biases for the One-Hot encoding, it is necessary to rearrange its Hamiltonian given in Eq. (3.24). This is done in the following up to the point, where the

J and h parameters become apparent:

$$H_{\mathrm{OH}} = \Lambda \left(\left[\sum_i^N \frac{1-\sigma_i^z}{2} \right]^2 - 2 \left[\sum_i^N \frac{1-\sigma_i^z}{2} \right] + 1 \right) \tag{A.57}$$

$$= \Lambda \left(1 - \left[\sum_i^N 1 - \sigma_i^z \right] + \frac{1}{4} \left[\sum_{i,j}^N 1 - \sigma_i^z - \sigma_j^z + \sigma_i^z \sigma_j^z \right] \right) \tag{A.58}$$

$$= \Lambda \left(\underbrace{1 - N + \frac{N^2}{4}}_{C} + \sum_i^N \sigma_i^z + \frac{1}{4} \left[\sum_{i,j}^N -\sigma_i^z - \sigma_j^z + \sigma_i^z \sigma_j^z \right] \right) \tag{A.59}$$

$$\propto \Lambda \left(\left[1 - \frac{N}{2} \right] \sum_i^N \sigma_i^z + \frac{1}{4} \sum_{i,j}^N \sigma_i^z \sigma_j^z \right) \tag{A.60}$$

$$= \underbrace{\Lambda \left[1 - \frac{N}{2} \right]}_{\Lambda'} \left(\sum_i^N \sigma_i^z + \frac{1}{4 \left[1 - \frac{N}{2} \right]} \sum_{i,j}^N \sigma_i^z \sigma_j^z \right) \tag{A.61}$$

List of Figures

Bibliography

[ABS22] Abel, Steve ; Blance, Andrew ; Spannowsky, Michael: Quantum optimization of complex systems with a quantum annealer. In: *Phys. Rev. A* 106 (2022), Oct, 042607. http://dx.doi.org/10.1103/PhysRevA.106.042607. – DOI 10.1103/PhysRevA.106.042607

[ACS21] Abel, Steven ; Chancellor, Nicholas ; Spannowsky, Michael: Quantum computing for quantum tunneling. In: *Phys. Rev. D* 103 (2021), Jan, 016008. http://dx.doi.org/10.1103/PhysRevD.103.016008. – DOI 10.1103/PhysRevD.103.016008

[AG08] Al-Gwaiz, M. A.: The Sturm–Liouville Theory. In: *Sturm-Liouville Theory and its Applications*. London : Springer London, 2008. – ISBN 978–1–84628–972–9, 41–91

[AGT19] Ai, Wen-Yuan ; Garbrecht, Björn ; Tamarit, Carlos: Functional methods for false-vacuum decay in real time. In: *Journal of High Energy Physics* 2019 (2019), Dec, Nr. 12, 95. http://dx.doi.org/10.1007/JHEP12(2019)095. – DOI 10.1007/JHEP12(2019)095. – ISSN 1029–8479

[Ami15] Amin, Mohammad H.: Searching for quantum speedup in quasistatic quantum annealers. In: *Phys. Rev. A* 92 (2015), Nov, 052323. http://dx.doi.org/10.1103/PhysRevA.92.052323. – DOI 10.1103/PhysRevA.92.052323

[AS21] Abel, Steven ; Spannowsky, Michael: Quantum-Field-Theoretic Simulation Platform for Observing the Fate of the False Vacuum. In: *PRX Quantum* 2 (2021), Mar, 010349. http://dx.doi.org/10.1103/PRXQuantum.2.010349. – DOI 10.1103/PRXQuantum.2.010349

[Bad13] Bader, Michael: *Space-filling Curves. An Introduction With Applications in Scientific Computing*. Bd. 9. Springer Berlin Heidelberg, 2013. http://dx.doi.org/10.1007/978-3-642-31046-1. http://dx.doi.org/10.1007/978-3-642-31046-1. – ISBN 978–3–642–31045–4

[BHS+16] Blum, Kfir ; Honda, Masazumi ; Sato, Ryosuke ; Takimoto, Masahiro ; Tobioka, Kohsaku: O(N) Invariance of the Multi-Field Bounce. In: *Journal of High Energy Physics* 2017 (2016), 11. http://dx.doi.org/10.1007/JHEP05(2017)109. – DOI 10.1007/JHEP05(2017)109

[BP18] Brown, Erin ; Peña, Lisandro Hernández de l.: A Simplified Pöschl–Teller Potential: An Instructive Exercise for Introductory Quantum Mechanics. In:

Journal of Chemical Education 95 (2018), Nr. 11, 1989-1995. http://dx.doi.org/10.1021/acs.jchemed.8b00029. – DOI 10.1021/acs.jchemed.8b00029

[BRI+14] Boixo, Sergio ; Rønnow, Troels F. ; Isakov, Sergei V. ; Wang, Zhihui ; Wecker, David ; Lidar, Daniel A. ; Martinis, John M. ; Troyer, Matthias: Evidence for quantum annealing with more than one hundred qubits. In: *Nature Physics* 10 (2014), Mar, Nr. 3, 218-224. http://dx.doi.org/10.1038/nphys2900. – DOI 10.1038/nphys2900. – ISSN 1745–2481. – See the "Gauge Averaging" section in supplemental material

[CC77] Callan, Curtis G. ; Coleman, Sidney: Fate of the false vacuum. II. First quantum corrections. In: *Physical Review D* 16 (1977), September, Nr. 6, 1762–1768. http://dx.doi.org/10.1103/PhysRevD.16.1762. – DOI 10.1103/PhysRevD.16.1762. – ISSN 0556–2821

[CCD+22] Chancellor, Nicholas ; Crowley, Philip J. D. ; Durić, Tanja ; Vinci, Walter ; Amin, Mohammad H. ; Green, Andrew G. ; Warburton, Paul A. ; Aeppli, Gabriel: Error measurements for a quantum annealer using the one-dimensional Ising model with twisted boundaries. In: *npj Quantum Information* 8 (2022), Jun, Nr. 1, 73. http://dx.doi.org/10.1038/s41534-022-00580-w. – DOI 10.1038/s41534–022–00580–w. – ISSN 2056–6387

[CGKN16] Cevik, D. ; Gadella, M. ; Kuru, S. ; Negro, J.: Resonances and antibound states for the Pöschl–Teller potential: Ladder operators and SUSY partners. In: *Physics Letters A* 380 (2016), April, Nr. 18-19, 1600–1609. http://dx.doi.org/10.1016/j.physleta.2016.03.003. – DOI 10.1016/j.physleta.2016.03.003. – ISSN 03759601

[Cha19] Chancellor, Nicholas: Domain wall encoding of discrete variables for quantum annealing and QAOA. In: *Quantum Science and Technology* 4 (2019), aug, Nr. 4, 045004. http://dx.doi.org/10.1088/2058-9565/ab33c2. – DOI 10.1088/2058–9565/ab33c2

[Col77] Coleman, Sidney: Fate of the false vacuum: Semiclassical theory. In: *Phys. Rev. D* 15 (1977), May, 2929–2936. http://dx.doi.org/10.1103/PhysRevD.15.2929. – DOI 10.1103/PhysRevD.15.2929

[D-W21] D-Wave Systems Inc.: *D-Wave Technical Note: Errors and Error Correction*, 2021. https://docs.dwavequantum.com/en/latest/quantum_research/annealing.html#freezeout-points. – Accessed: 2025-06-13

[DDDLR22] Devoto, Federica ; Devoto, Simone ; Di Luzio, Luca ; Ridolfi, Giovanni: False vacuum decay: an introductory review. In: *Journal of Physics G: Nuclear and Particle Physics* 49 (2022), aug, Nr. 10, 103001. http://dx.doi.org/10.1088/1361-6471/ac7f24. – DOI 10.1088/1361–6471/ac7f24

[DTD23] Dupire, Bruno ; Tissot-Daguette, Valentin: *Functional Expansions*. https://arxiv.org/abs/2212.13628. Version: 2023

[DWa25] *Advantage System 6.4 anneal schedule*. https://docs.dwavequantum.com/en/latest/quantum_research/solver_properties_specific.html#advantage-system6-4, 2025. – Accessed: 2025-05-07

[Ern94] Ernzerhof, Matthias: Taylor-series expansion of density functionals. In: *Phys. Rev. A* 50 (1994), Dec, 4593–4607. http://dx.doi.org/10.1103/PhysRevA.50.4593. – DOI 10.1103/PhysRevA.50.4593

[GF65] Gelfand, I. M. ; Fomin, S. V.: *Calculus of variations*. Revised English edition. Translated and edited by Richard A. Silverman. 3rd. printing. Englewood Cliffs, N.J.: Prentice-Hall, Inc. VII, 232 p. (1965)., 1965

[GR96] Greiner, Walter ; Reinhardt, Joachim: Classical Field Theory. In: *Field Quantization*. Berlin, Heidelberg : Springer Berlin Heidelberg, 1996. – ISBN 978–3–642–61485–9, 31–54

[HJL+10] Harris, R. ; Johnson, M. W. ; Lanting, T. ; Berkley, A. J. ; Johansson, J. ; Bunyk, P. ; Tolkacheva, E. ; Ladizinsky, E. ; Ladizinsky, N. ; Oh, T. ; Cioata, F. ; Perminov, I. ; Spear, P. ; Enderud, C. ; Rich, C. ; Uchaikin, S. ; Thom, M. C. ; Chapple, E. M. ; Wang, J. ; Wilson, B. ; Amin, M. H. S. ; Dickson, N. ; Karimi, K. ; Macready, B. ; Truncik, C. J. S. ; Rose, G.: Experimental investigation of an eight-qubit unit cell in a superconducting optimization processor. In: *Phys. Rev. B* 82 (2010), Jul, 024511. http://dx.doi.org/10.1103/PhysRevB.82.024511. – DOI 10.1103/PhysRevB.82.024511

[JAG+11] Johnson, M. W. ; Amin, M. H. S. ; Gildert, S. ; Lanting, T. ; Hamze, F. ; Dickson, N. ; Harris, R. ; Berkley, A. J. ; Johansson, J. ; Bunyk, P. ; Chapple, E. M. ; Enderud, C. ; Hilton, J. P. ; Karimi, K. ; Ladizinsky, E. ; Ladizinsky, N. ; Oh, T. ; Perminov, I. ; Rich, C. ; Thom, M. C. ; Tolkacheva, E. ; Truncik, C. J. S. ; Uchaikin, S. ; Wang, J. ; Wilson, B. ; Rose, G.: Quantum annealing with manufactured spins. In: *Nature* 473 (2011), May, Nr. 7346, 194-198. http://dx.doi.org/10.1038/nature10012. – DOI 10.1038/nature10012. – ISSN 1476–4687

[KL25] Kavaki, Ali H. Z. ; Lewis, Randy: False vacuum decay in triamond lattice gauge theory. In: *Phys. Rev. D* 112 (2025), Jul, 014502. http://dx.doi.org/10.1103/1km8-3tc3. – DOI 10.1103/1km8–3tc3

[KMV22] Kumar, Gaurav ; Mishra, Radha R. ; Verma, Akarsh: Introduction to Molecular Dynamics Simulations. In: Verma, Akarsh (Hrsg.) ; Mavinkere Rangappa, Sanjay (Hrsg.) ; Ogata, Shigenobu (Hrsg.) ; Siengchin, Suchart (Hrsg.): *Forcefields for Atomistic-Scale Simulations: Materials and Applications*. Singapore : Springer Nature Singapore, 2022. – ISBN 978–981–19–3092–8, 1–19

[Kru64] Kruskal, J. B.: Nonmetric Multidimensional Scaling: A Numerical Method. In: *Psychometrika* 29 (1964), Nr. 2, S. 115–129. http://dx.doi.org/10.1007/BF02289694. – DOI 10.1007/BF02289694

[MVHR19] Marshall, Jeffrey ; Venturelli, Davide ; Hen, Itay ; Rieffel, Eleanor G.: Power of Pausing: Advancing Understanding of Thermalization in Experimental Quantum Annealers. In: *Phys. Rev. Appl.* 11 (2019), Apr, 044083. http://dx.doi.org/10.1103/PhysRevApplied.11.044083. – DOI 10.1103/PhysRevApplied.11.044083

[PS95] Peskin, Michael E. ; Schroeder, Daniel V.: *An Introduction to Quantum Field Theory*. Westview Press, 1995. – Reading, USA: Addison-Wesley (1995) 842 p

[SABW82] Swope, William C. ; Andersen, Hans C. ; Berens, Peter H. ; Wilson, Kent R.: A computer simulation method for the calculation of equilibrium constants for the formation of physical clusters of molecules: Application to small water clusters. In: *The Journal of Chemical Physics* 76 (1982), 01, Nr. 1, 637-649. http://dx.doi.org/10.1063/1.442716. – DOI 10.1063/1.442716. – ISSN 0021–9606

[VDH+25] Vodeb, Jaka ; Desaules, Jean-Yves ; Hallam, Andrew ; Rava, Andrea ; Humar, Gregor ; Willsch, Dennis ; Jin, Fengping ; Willsch, Madita ; Michielsen, Kristel ; Papić, Zlatko: Stirring the false vacuum via interacting quantized bubbles on a 5,564-qubit quantum annealer. In: *Nature Physics* 21 (2025), Mar, Nr. 3, 386-392. http://dx.doi.org/10.1038/s41567-024-02765-w. – DOI 10.1038/s41567–024–02765–w. – ISSN 1745–2481